ISSN 2518-7198 (Print)
ISSN 2663-5089 (Online)

BULLETIN

OF THE KARAGANDA UNIVERSITY

PHYSICS

Series

№ 4(104)/2021

ISSN 2663-5089 (Online)
ISSN-L 2518-7198 (Print)
Индексі 74616
Индекс 74616

ҚАРАҒАНДЫ УНИВЕРСИТЕТІНІҢ ХАБАРШЫСЫ

ВЕСТНИК КАРАГАНДИНСКОГО УНИВЕРСИТЕТА

BULLETIN OF THE KARAGANDA UNIVERSITY

ФИЗИКА сериясы

Серия ФИЗИКА

PHYSICS Series

№ 4(104)/2021

Қазан–қараша–желтоқсан
30 желтоқсан 2021 ж.
Октябрь–ноябрь–декабрь
30 декабря 2021 г.
October–November–December
December, 30th, 2021

1996 жылдан бастап шығады
Издается с 1996 года
Founded in 1996

Жылына 4 рет шығады
Выходит 4 раза в год
Published 4 times a year

Қарағанды, 2021
Караганда, 2021
Karaganda, 2021

Редакцияның мекенжайы: 100024, Қазақстан, Қарағанды қ., Университет к-сі, 28
Тел.: +7 701 531 4758; факс: (7212) 35-63-98.
E-mail: vestnikku@gmail.com; karabekova71@mail.ru
Сайты: physics-vestnik.ksu.kz

Қарағанды университетінің хабаршысы. «Физика» сериясы.

ISSN-L 2518-7198 (Print). ISSN 2663-5089 (Online).

Меншік иесі: «Академик Е.А. Бөкетов атындағы Қарағанды университеті» КЕАҚ.

Қазақстан Республикасы Ақпарат және қоғамдық даму министрлігімен тіркелген. 30.09.2020 ж. № KZ38VPY00027378 қайта есепке қою туралы куәлігі.

Басуға 29.12.2021 ж. қол қойылды. Пішімі 60×84 1/8. Қағазы офсеттік. Көлемі 12,25 б.т. Таралымы 200 дана. Бағасы келісім бойынша. Тапсырыс № 111.

«Акад. Е.А. Бөкетов ат. Қарағанды ун-ті» КЕАҚ баспасының баспаханасында басылып шықты.
100024, Қазақстан, Қарағанды қ., Университет к-сі, 28. Тел. (7212) 35-63-16. E-mail: izd_kargu@mail.ru

Адрес редакции: 100024, Казахстан, г. Караганда, ул. Университетская, 28
Тел.: +7 701 531 4758. Факс: (7212) 35-63-98.
E-mail: vestnikku@gmail.com; karabekova71@mail.ru
Сайт: physics-vestnik.ksu.kz

Редакторы
Ж.Т. Нурмуханова, С.С. Балкеева, З.Е. Рамазанова

Компьютерная верстка
Г.Қ. Жанбосова

Вестник Карагандинского университета. Серия «Физика».

ISSN-L 2518-7198 (Print). ISSN 2663-5089 (Online).

Собственник: НАО «Карагандинский университет имени академика Е.А. Букетова».

Зарегистрирован Министерством информации и общественного развития Республики Казахстан. Свидетельство о постановке на переучет № KZ38VPY00027378 от 30.09.2020 г.

Подписано в печать 29.12.2021 г. Формат 60×84 1/8. Бумага офсетная. Объем 12,25 п.л. Тираж 200 экз. Цена договорная. Заказ № 111.

Отпечатано в типографии издательства НАО «Карагандинский университет им. акад. Е.А. Букетова». 100024, Казахстан, г. Караганда, ул. Университетская, 28. Тел. (7212) 35-63-16. E-mail: izd_kargu@mail.ru

Postal address: 28, University Str., 100024, Karaganda, Kazakhstan
Tel.: +7 701 531 4758; Fax: (7212) 35-63-98.
E-mail: vestnikku@gmail.com; karabekova71@mail.ru
Web-site: physics-vestnik.ksu.kz

Editors
Zh.T. Nurmukhanova, S.S. Balkeyeva, Z.E. Ramazanova

Computer layout
G.K. Zhanbossova

Bulletin of the Karaganda University. "Physics" series.
ISSN-L 2518-7198 (Print). ISSN 2663-5089 (Online).
Proprietary: NLC "Karagandy University of the name of academician E.A. Buketov".
Registered by the Ministry of Information and Social Development of the Republic of Kazakhstan. Rediscount certificate No. KZ38VPY00027378 dated 30.09.2020.

Signed in print 29.12.2021. Format 60×84 1/8. Offset paper. Volume 12,25 p.sh. Circulation 200 copies. Price upon request. Order № 111.
Printed in the Publishing house of NLC "Karagandy University of the name of acad. E.A. Buketov".
28, University Str., Karaganda, 100024, Kazakhstan. Tel. (7212) 35-63-16. E-mail: izd_kargu@mail.ru

МАЗМҰНЫ — СОДЕРЖАНИЕ — CONTENT

ТЕХНИКАЛЫҚ ФИЗИКА
ТЕХНИЧЕСКАЯ ФИЗИКА
TECHNICAL PHYSICS

КОНДЕНСАЦИЯЛАНҒАН КҮЙДІҢ ФИЗИКАСЫ
ФИЗИКА КОНДЕНСИРОВАННОГО СОСТОЯНИЯ
PHYSICS OF THE CONDENSED MATTER

ЖЫЛУФИЗИКАСЫ ЖӘНЕ ТЕОРИЯЛЫҚ ЖЫЛУТЕХНИКАСЫ
ТЕПЛОФИЗИКА И ТЕОРЕТИЧЕСКАЯ ТЕПЛОТЕХНИКА
THERMOPHYSICS AND THEORETICAL THERMOENGINEERING

ТЕХНИКАЛЫҚ ФИЗИКА
ТЕХНИЧЕСКАЯ ФИЗИКА
TECHNICAL PHYSICS

DOI 10.31489/2021PH4/6-15

UDC 539.12

K.M. Mukashev[1,3*], A.V. Stepanov[2], A.Kh. Argynova[1], V.V. Zhukov[1,2], T.K. Idrisova[1]

[1]Satbayev University, Institute of Physics and Technology, Almaty, Kazakhstan;
[2]Tien Shan High-Mountain Scientific Station in the Republic of Kazakhstan,
Branch of the Physical Institute of the Russian Academy of Sciences, Almaty, Kazakhstan;
[3]Al-Farabi Kazakh National University, Almaty, Kazakhstan
([*]E- mail: mukashev.kms@gmail.com; argali7@mail.ru)

About one way of organization Unified system for registration of space rays

Today, at the high-mountain scientific station for the study of the physics of cosmic rays, various, independently operating unique experimental installations are used. The ways and methods of combining these installations into a single system are discussed in the article. A single system includes networks of scintillation detectors of the "carpet" type for registration of the electron-photon component, ground and underground monitors for registration of neutron components, calorimeters, Cherenkov detectors, a scintillation spectrometer and a number of other subsystems. The newly created unified system for registering cosmic rays based on the achievements of modern technology and scientific thought will have a high resolution, with a common databank with synchronization in time of operation of separate, independently operating experimental installations. The solution to this problem will help to perform a detailed analysis of the recorded events from a single position, to carry out complex calculations of the spatial distribution, mass composition, and also the energy structure of cosmic rays with a high degree of accuracy. Significant scientific results, obtained in recent years at the Horizon-T experimental installation, are provided. The presented preliminary significant data obtained during the implementation of the project testify to the high information content of the obtained results.

Keywords: cosmic rays, scintillation detector, neutron monitors, fiber optics, local area network, server, extensive air showers, unified database.

Introduction

First of all, it should be emphasized that the physics of cosmic rays belongs to fundamental science. One may ask the question — why does society need fundamental science, which does not bring immediate benefit to mankind, as is sometimes the case with applied research? It should be noted that applied science regularly faces problems that it simply cannot solve itself — neither with the help of accumulated practical experience, nor through the insight of inventors, nor by trial and error. However, they can be solved with the help of fundamental science. Fundamental science is the basis of new high technologies in the long term, technologies understood in the broadest sense [1]. If some small improvements in existing technologies can be made, limiting ourselves to purely applied research, then creating new technologies and with their help solving new problems that regularly face humanity – it is possible only relying on fundamental science [2].

Cosmic ray physics is the physics of elementary particles, one of its facets, which through the development of mathematical formalism is tightly connected with plenty of more "practical" areas of physics, and natural sciences in general. Cosmic rays (CR) are usually understood as fluxes of charged relativistic particles, ranging from protons and helium nuclei to the nuclei of heavier elements up to uranium, born and accelerated to high and extremely high (up to 10^{20} eV) energies outside the Earth [3, 4]. In this case, the contri-

bution of the Sun dominates in the flux of particles with energies up to 10^9 eV, and particles of higher energies are of galactic (and, possibly, at the highest energies, extragalactic) origin. Naturally, protons and nuclei do not exhaust the whole variety of radiation coming to the Earth from outer space. The composition of galactic cosmic rays (GCR) is mainly dominated by protons, the rest of the nuclei account for less than 10% of all inputs. Protons remain the dominant component, at least up to energies of ~ 1TeV, although the fraction of nuclei grows with increasing particle energy.

Certainly, not all physical processes explaining the origin of cosmic rays are understood, and not everything is clear with their effect on the space surrounding the Earth, on biological and technological systems. Every day brings new facts, gives rise to new hypotheses, makes us take a fresh look at seemingly already known physical phenomena [5]. Over the past decades, science has made great strides in understanding the space around us, and scientists are trying to explain and link the seemingly incompatible phenomena into a single chain. The theory of the origin of GCRs, which could be called entirely complete, is currently absent, especially if we bear in mind the origin of GCRs of ultrahigh energies (>10^{15} eV), although over the past 10-15 years in understanding the general nature of the processes in which cosmic rays are emerging and accelerating, a significant progress has been made. A completed theory of the origin of GCRs should explain their main characteristics: the power-law shape of the energy spectrum, the magnitude of the energy density, the mass (chemical) composition of primary CRs including data on the fluxes of antiprotons, electrons, positrons, gamma quanta, the practical constancy of the GCR intensity in time, and their weak anisotropy [6, 7].

The existence of cosmic rays — a stream of high-energy elementary particles coming to Earth from outer space — was established in 1912 by the Austrian physicist V.F. Hess [8, 9]. Later, through the works of subsequent researchers, many new phenomena and patterns were discovered, including the so-called extensive air showers (EAS), the limiting energy spectrum of cosmic rays, which extends up to energy of 10^{20} eV. Particular interest to researchers is the energy range 10^{15}-10^{18} eV, in which a break in the CR energy spectrum was first discovered, and then a number of interesting phenomena incorporating a rather sharp change in the chemical composition of primary cosmic radiation, the appearance of a long-range component, the appearance of delayed particles and showers. The essence of the delay lies in the fact that these particles or the products of their interaction with the atmosphere reach the earth's surface with some delay relative to the front of extensive air showers [10].

Experimental installations, available today in the world for CR registration, are mainly focused on solving individual particular problems. For example, the Yakutsk complex EAS installation, created in the valley of the Lena River, makes it possible to analyze cosmic radiation in terms of energies exceeding 10^{17} eV, to assess its impact on the Earth's atmosphere. The AGASA facility located in Japan was launched almost simultaneously with the facility in Yakutia. The two stations serve similar purposes. Main feature of the AGASA station is considered to be a huge scale – it covers an area of about 100 square kilometers and is a complex of 111 surface detectors and 27 muon detectors. The KASCADE-Grande installation in Karlsruhe is a large ground network of 252 detector stations designed to study extensive air showers. The world's largest Pierre Auger Observatory is located in Argentina, covers an area of 3,000 square kilometers and consists of 1,600 receivers. Its main purpose is to register EASs generated by ultrahigh-energy particles. Nevertheless, despite the complexity and the achieved level of CR registration efficiency, none of the above installations is fully integrated, capable of solving, if not all, then at least the most important sets of tasks and problems facing researchers in the field of physics and cosmic ray astrophysics.

In this regard, this work describes the results achieved to date by combining separate, independently operating basic experimental installations and subsystems of the Physico-Technical Institute (PTI) and the Tien Shan High-Mountain Scientific Station (TSHMSS) into a single integrated system. The structure of this unique complex includes: a flood section, ground and underground neutron monitors; underground muon detectors; neutron detectors; an ionization calorimeter with a gamma-block, where for the first time research is held in the field of cosmic ray astrophysics – gamma astronomy; thrust installation; scintillation spectrometers; EAS radio emission detectors; Cherenkov light detectors; means of registration and analysis of the pulse shape of the EAS leading edge; and a number of other subsystems and means [11]. In addition, the creation of a unified database of experimental results and data extracted by a complex installation helps to take into account all the nuances that arise when accessing various sources of information and their subsequent processing.

Unified integrated system of FTI and TSHVNS

Since the beginning of the sixties of the last century in the vicinity of Almaty city in the mountains of the Zailiiskii Alatau at an altitude of 3340 m above sea level at the experimental site "Cosmostation" by the Physico-Technical Institute of the Ministry of Education and Science of the Republic of Kazakhstan and the Physical Institute named after P.N. Lebedev RAS, joint experiments are being carried out to study the physics of cosmic rays. During this time, fundamental world-class results have been obtained in the study of the CR energy spectrum, measurements of the mass composition, and the search for the anisotropy of primary cosmic rays in various energy ranges. Significantly, more reliable data on CR can be obtained using complex methods of simultaneous registration of charged particles with scintillators, observations of Cherenkov light and radio emission. The advantages of these methods are due to the fact that during the generation of hadron, electron-photon, and muon components, as well as Cherenkov and radio emissions, the atmosphere plays the role of a giant calorimeter, while fluctuations characteristic of the charged component of an EAS are substantially smoothed out. The large scatter of experimental data in the energy range of 10^{16}–10^{19} eV, because its study requires installations with an area of at least a square kilometer at minimum distances between detectors. Due to the low cost of radio emission detectors in contrast to Cherenkov and scintillation detectors, a greater number of such detectors can be placed on the same area and at closer distances from each other, which provides a more detailed study of the spatial and energy structure of EASs. The solution to this problem facilitates to conduct practically round-the-clock measurements, regardless of weather conditions, with a high degree of accuracy, reliability and information content.

Experimental installations of the type "Hadron-55", "Storm installation", "Horizon-T", "Radio emission EAS", "Thunderstorm", "MAS2" (installation for recording earthquakes) and others, which contain a carpet of scintillation detectors, ground and underground neutron monitors, a calorimeter with a gamma block and neutron detectors, Cherenkov light detectors, remote scintillation detectors, a scintillation spectrometer, and a number of other subsystems, are combined into the following items, for which a general network infrastructure scheme has been developed with the ability to connect them to a single dedicated local network (Fig. 1):

- Point "Dormitory", the center of the local network is located here: network and server equipment. Point coordinates: 43.043335N, 76.943078E.
- Point "Boathouse", the center of the storm water installation. Point coordinates: 43.042556N, 76.944330E.
- Point "Physico-Technical Institute", center of the "Hadron-55" installation with a calorimeter, gamma-block and neutron detectors. Point coordinates: 43.044078N, 76.943458E.
- Point "Horizon", registration center of the "Horizon-T" installation. Point coordinates: 43.047177N, 76.945417E.
- Point "Bunker", here are the remote detectors of the "Horizon-T" installation with an autonomous registration system. Point coordinates: 43.049165N, 76.957369E.
- Item "Stone Flower". Remote detectors of the Gorizont-T installation with an autonomous registration system. Point coordinates: 43.050650N, 76.946487E.
- Neutron Super Monitor. Point coordinates: 43.042864N, 76.944314E.
- "Dungeon". Point coordinates: 43.042665N, 76.945063E.

The communication between the subsystems is performed by combining fiber-optic lines into a network, which increased the reliability of communication and the speed of data transmission over the network. The use of a fiber-optic line has increased the resistance of the local network to adverse environmental influences such as precipitation, lightning discharges and static electricity.

Fiber optic lines are built on the basis of Sterlite Aerial Fig-8 Fiber Optic Cable, a self-supporting eight-fiber single-mode cable. The ends of the cable are wound and terminated in optical distribution frames, then they are connected to media converters by means of optical patch cords. The FH-MC100 Series Fiber Optic Media Converter converts 10/100Base-TX connections to 100Base-FX connections and vice versa. The 10/100Base-TX port has 10/100 Mbps auto-negotiation features. The device supports single-mode and multi-mode SC connections. This converter allows for fiber-optic connections at a distance of up to 20 km over two fibers. Media converters are connected to the local network with 10/100Base-TX patch cords.

Figure 1. Fiber optic lines – the basis of the local area network

To improve performance, the local area network was divided into two segments. The first segment with the address range 192.168.11.1–192.168.11.254 (class C network 192.168.11.0/24) includes computers of registration systems, two database servers, a file and Internet server, and a NAS data backup system. The second segment with addresses 192.168.12.1–192.168.12.254 (class C network 192.168.12.0/24) is intended for access from the local network to servers, computers of registration systems and the Internet for all interested users. The network segments are interconnected via the Ubiquiti EdgeRouter ER-X router. Based on Cisco 1760 and Cisco 2620 routers, gateways are used to access the Internet.

In addition, it was decided to include in the local computer network part of the remote subsystems that previously worked autonomously, which would be connected to the local computer network via radio channels. Radio channels for connecting distant points are built on the basis of Ubiquiti AirMAX equipment operating at frequencies of 5.470-5.825 GHz. This band, unlike the 2.4 GHz WiFi band, is less congested and less susceptible to interference. At the central point of the radio network, it is planned to place an Ubiquiti Rocket M5 access point with an Ubiquiti AirMAX Omni 5G10 omnidirectional antenna connected to it. Ubiquiti NanoBeam M5-16 radio bridges will be deployed at remote locations.

Installation of the database server and backup system

When modeling a database server combined with an Internet server, the rack server HUAWEI RH2285V2 is used as a layout. The server includes two Intel Xeon E5-2400 4-core CPUs, 16GB RAM DDR3, two 1TB hard disks combined into a mirrored disk array RAID 1. The network equipment is represented by two 10/100/1000 Mbps Ethernet interfaces. The server runs under Scientific Linux operating system version 7.8. To work with databases, a free object-relational database management system PostgreSQL version 11.9 is deployed on the server. NTP daemon version 4 is running on the server, providing synchronization with world time with an accuracy of no worse than 10 ms (1/100 s) when working via the Internet, and up to 0.2 ms (1/5000 s) inside local networks.

Application package

A package of application programs for working from a local network is programs that use the developed libraries, form queries to databases, transfer the requested records to the program content and process them in accordance with the specified criteria. The processed data will be presented in text or graphic form. Using the Linux operating system, programming languages C, C ++, Python, Java, Java script, programming interfaces and modules have been developed and debugged, allowing to transfer database records into program content.

2. Significant research results at the Horizon-T installation

Horizon-T installation [12] registers the fluxes of charged particles of EAS with energies above 1016 eV and with nanosecond precision. It is designed to study the space-time structure of shower disks. Installation observation level is at 3340 m above sea level (see Figure 2).

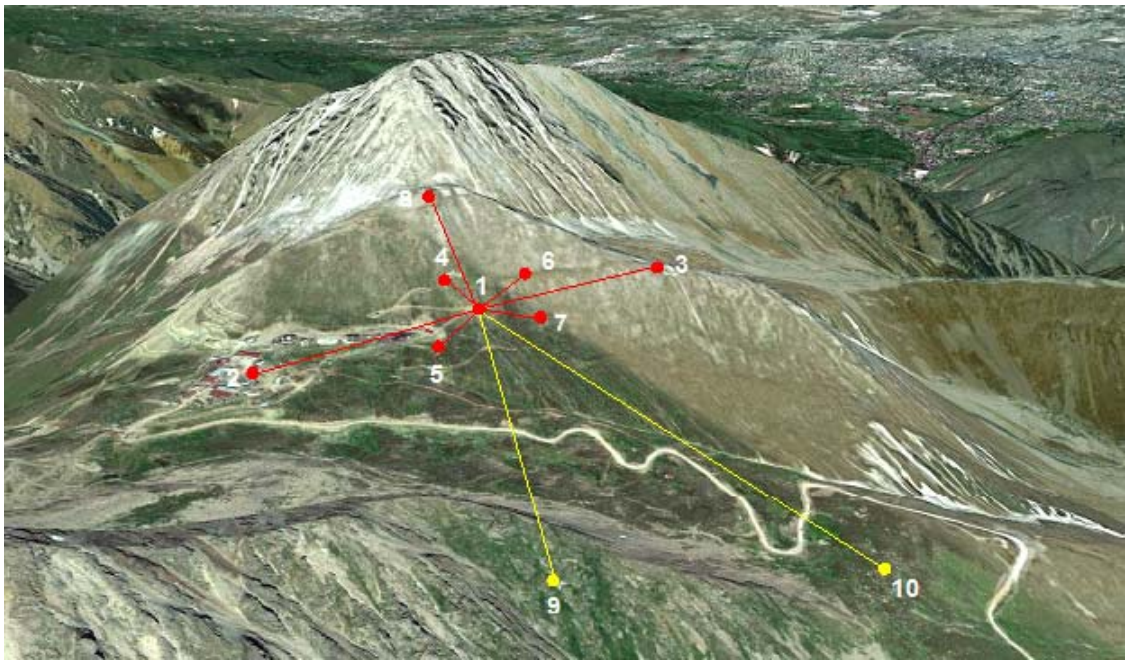

Figure 2. Geometry of the location of registration points of the Horizon-T installation

The space-time characteristics of the fluxes of charged particles of EAS, which were obtained at the Horizon-T installation, are compared with the space-time characteristics of the fluxes of charged particles of electron-nuclear showers from protons, which were obtained using the CORSIKA model package [13].

The composition of particles that reached the Earth's surface in electron-nuclear showers from primary protons with an energy of $2x10^{17}$ eV, which were obtained by drawing for the CORSIKA model package, was considered. Gamma quanta, neutrinos, electrons, positrons and muons dominate in these particles.

In the present experiment, charged particles were considered when the difference between an electron and a positron is not significant. “Electrons” and “positrons” were considered as “electrons”. In an electron-nuclear shower with energy $2\cdot10^{17}$eV, from the vertical direction to the observation level, on average, about 10^{8}charged particles, in a shower with an energy of $2\cdot10^{18}$eVon average pass about 10^{9}particles.

Among charged particles that come to the observation level from directions close to the vertical (up to zenith angles of 30°), the fraction of electrons is close to 99%, the fraction of muons is about 1%. By increasing zenith angles, the electron flux density decreases, and the muon flux density increases, and in the EAS from the zenith directions more than 70° the muon flux density exceeds the electron flux.

Conducted drawings of electron-nuclear showers using the CORSIKA model package illustrated the following:

1. With an increase in the distance to the shower axis, the flux density of charged shower particles at the observation level decreases rapidly.

2. Only one storm disk arrives at an altitude of 3340 m above sea level, unaccompanied by delayed particles. Therefore, when streams of charged particles of a shower pass through the detector, a pulse with only one maximum is formed.

3. The duration of the pulse in the SC detector from the passage of charged particles of the shower increases rapidly with increasing distance to the axis of the shower.

Below is an analysis of the experimental material obtained at the Horizon-T installation from March 21 to May 12 2018, when over 1137 hours, 15725 events were recorded with an intensity of 13.8 events / hour and a detection threshold of $2 \cdot 10^{16}$eV.

More than 500 showers were found in this experimental material, in which delayed particles are observed. In showers with energies less than10^{17}eV, recorded with the Horizon-T installation, any pulses had only one maximum. All showers with delayed particles have energies above 10^{17}eV. The recorded intensity of showers with delayed particles does not contradict the luminosity of the installation.

The term delayed particles implicitly implies that one group of particles crosses the observation level as a part of the shower disk, while the other group of particles is delayed from the main shower disk. Experimental data obtained at the Horizon-T installation indicate that delayed EAS particles cross the observation level, forming two, three, or more pulses in the detectors along with the first pulse. An example of three pulses recorded in a shower with energies above $5 \cdot 10^{17}$eV, which came at a zenith angle of 30° from the southwest direction, is illustrated in Figure 3.

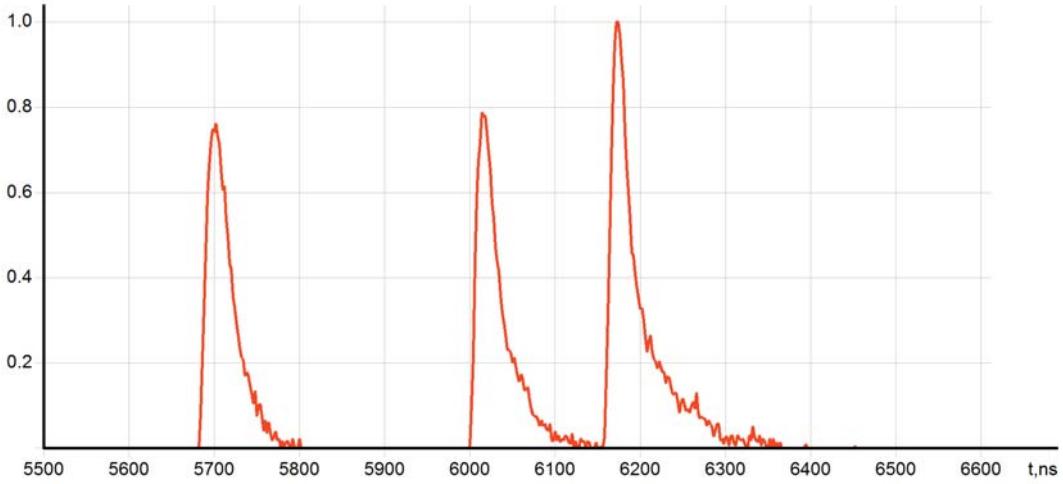

Note. The delay time of the second pulse from the first pulse is t_{12} = 318 ns, the third pulse from the second pulse is t_{13}= 465 ns.

Figure 3. Three pulses recorded in a shower with an energy higher than $5 \cdot 10^{17}$eV

The first pulse has a duration of τ_1=35 ns and is generated by the passage of 316 particles, the second pulse has a duration of τ_2= 32 ns and is generated by the passage of 327 particles, the third pulse has a duration of τ_2= 28 ns and is generated by the passage of 363 particles. Obviously, in this shower, the detector was crossed by particles of three shower disks. A disk that formed the first impulse came earlier than the others, but it does not follow from this that the disk is the main one. The term “delayed particles” simply means that the origin of the time scale is associated with the first disk. These three pulses, generated in the detector by particles of one shower, were considered as a single geometrical object, with three maxima (modes) and were called a trimodal pulse. The pulses with several peaks recorded in the detector were called multimodal pulses, respectively, showers in which multimodal pulses were recorded – multimodal showers.

Experimental data on multimodal showers obtained at the Horizon-T installation indicate that particles in such showers cross the observation level as part of several shower disks, each of which generates its own pulse in the detector of the facility.

In electron-nuclear showers with energies up to 10^{18}eV played out using the CORSIKA package of models, charged particles at any distance from the shower axis formed only one pulse. The modern physical concepts of electron-nuclear showers, which are implemented in the CORSIKA package of models, do not give delayed particles in EASs.

Figure 4 demonstrates the field of points with coordinates (R, ρ) for bimodal pulses recorded in the SC detector at point 9 in 217 showers. The curves are the functions of the spatial distribution ρ(R) in electron-nuclear showers, obtained in a raffle applying the CORSIKA package of models.

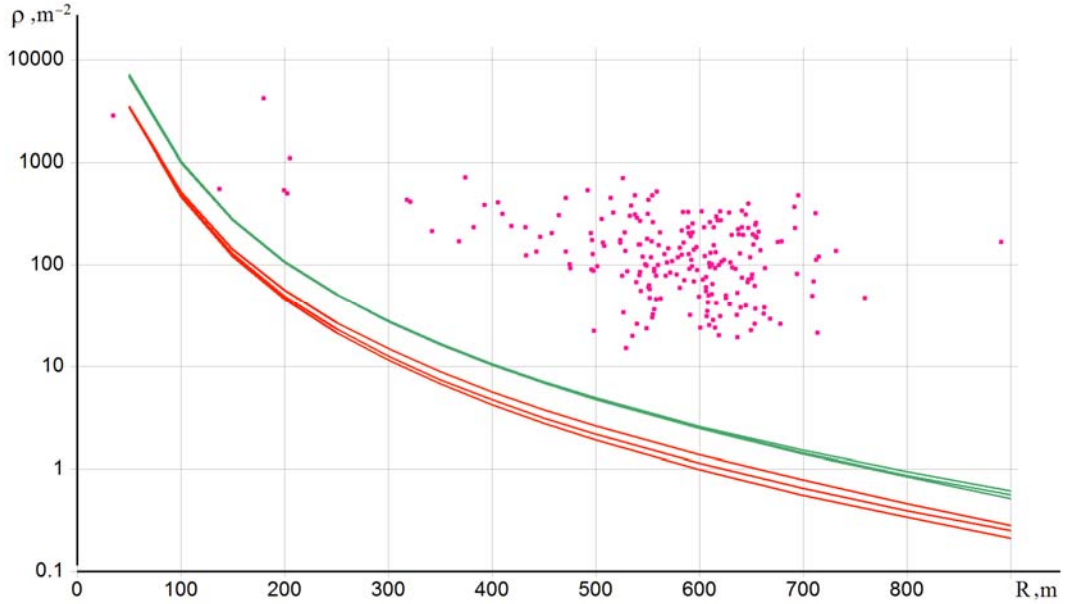

Note. The curves are the functions ρ(R) of the spatial distribution of charged particles of six electron-nuclear showers, which were obtained by drawing according to the CORSIKA model. Red curves – three showers with an energy of $5 \cdot 10^{17}$eV, green curves – three showers with an energy of 10^{18} eV.

Figure 4. Field of distribution of points with coordinates (R, ρ) in 217 showers recorded at the Horizon-T installation

The bimodal pulses recorded in point 9 are caused in the SC detector by charged particles, the flux densities of which are much higher than the flux densities of electron-nuclear showers with energies of 10^{18}eV at distances of 600 m from the shower axis, obtained using the CORSIKA model package. The distribution of points (R, ρ) in Fig. 4 shows that at R > 400 m, the experimental SDF does not change with increasing R. While the SDF of charged particles in electron-nuclear showers decreases several times.

Figure 4 designates that in electron-nuclear showers with energies of 10^{18} eVthe flux density of charged particles at a distance of 400 m from the shower axis is ρ_{400}=10.0 m^{-2}. Taking the flux density of charged particles in an electron-nuclear shower proportional to the shower energy, it can be estimated that a 10 times higher flux density ρ_{400} = 100 m^{-2} will appear in electron-nuclear showers at energies of 10^{19} eV. Accordingly, the flux density ρ_{400} = 300 m^{-2} can be recorded in electron-nuclear showers at energies of $3 \cdot 10^{19}$ eV.

The performed estimates of the luminosity of the Horizon-T installation showed that in 1137 hours it is capable of registering, on average, 1 electron-nuclear shower with an energy of 10^{19}eV and above. Registration of 108 electron-nuclear showers with energies of 10^{19}eV and above will require on average more than one hundred thousand hours. Registration of 27 electron-nuclear showers with energies of $3 \cdot 10^{19}$eV and above will require substantially more than one hundred thousand hours. Hence, it follows that bimodal impulses recorded at distances R=(400÷750) m cannot be generated by particles of electron-nuclear showers.

Results and Discussion

1. In EAS with energies above 10^{17}eV, the Horizon-T installation has recorded delayed particles that form a system of pulses in the detectors. The system of several pulses recorded in the detector is called a multimodal pulse – a pulse with several modes. EASs, in which multimodal impulses were recorded, are called multimodal EASs.

2. Analysis of electron-nuclear showers with energies from 10^{17}eV to 10^{18}eV, obtained applying the CORSIKA package of models, showed that delayed particles do not appear in electron-nuclear showers and, accordingly, only one pulse with one maximum (mode) can be recorded in the detectors. Therefore, it follows that multimodal EASs are not electron-nuclear showers.

3. The quantitative characteristics of bimodal impulses were studied. The behavior of these characteristics showed that in showers, which are called “EAS with delayed particles”, a system of several shower disks comes to the observation level. When the axis of one of these shower disks passes near the detector, a pulse is formed in the detector, the duration of which is an order of magnitude shorter, and the flux density is an order of magnitude greater than expected in electron-nuclear showers. This confirms that multimodal EASs are not electron-nuclear showers.

Conclusions

Combining all experimental installations into a single registration system with a common data bank makes it possible to perform a detailed analysis of events, complex calculations of the spatial and energy structure of EASs with a high degree of accuracy and reliability of the obtained results. A network infrastructure and a central server have been created to organize a single base of the entire system with the connection of individual experimental installations to a single dedicated local network. The organization of time synchronization of the operation of individual experimental installations with each other is ensured. The software support has been developed and debugged, which ensures the normal functioning of the entire infrastructure and uninterrupted client access to the database of the combined system.

Acknowledgments

This work was carried out with the support of grant funding from the Science of the Ministry of Education and Science of the Republic of Kazakhstan, No. AP08855641.

References

1 Zatsepin G.T. Penetrating particles in extensive air showers / G.T. Zatsepin, S.A. Kuchai, I.L. Rosenthal // DAN. — 1948. — Vol. 61. — P. 47–49.

2 Zatsepin G.T. Nuclear cascade process and its role in the development of extensive air showers // DAN. — 1949. — Vol. 67. – P. 993–997.

3 Zatsepin G.T. On the question of the absorption curve of «primary» particles of cosmic radiation / G.T. Zatsepin // ZhETF, — 1949. — Vol. 19. — P. 1104–1107.

4 Zatsepin G.T. Nuclear interaction of high-energy particles and extensive air showers / G.T. Zatsepin, I.L. Rosenthal, L.I. Sarycheva // Izvestiya Academy of Sciences of the USSR, ser. Physical. — 1953. — Vol.17. — P. 39–50.

5 Egorov T.A. On the construction of large scintillation counters with one PMT / T.A. Egorov, N.N. Efimov, D.D. Krasilnikov // Izvestiya AN SSSR, ser. Physical. — 1965. — V.24. — No. 9. — P. 1788–1790.

6 Gunningham G. The energy spectrum and arrival direction distributions of cosmic rays with energies above 10^{19} eV / G. Gunningham // Aph. J. — 1980. — Vol. 71. — P. 236–239.

7 Suga K. Scintillation detector of 4 m^2 area and transistorized amplifier with logarithmic response / K. Suga // Rev. Sc. Instruments. — 1961. — Vol. 32. — P. 1187–1189.

8 Shinozaki K. For AGASA Colaboration. AGASA Results / K. Shinozaki, M. Teshima // Nucl. Phys. B (Proc. Suppl.). — 2004. — Vol. 136. — P. 18–27.

9 Tomson G. New Results from the HiRes Experiment / G. Tomson // Nucl. Phys. B (Proc. Suppl.), — 2004. — Vol. 136. — P. 28–39.

10 Beisembaev R.U., Beisembaeva E.A., Dalkarov O.D., Mosunov V.D. Spatial and Temporal Characteristics of EAS with Delayed Particles / 36th International Cosmic Ray Conference -ICRC2019 — (July 24th — August 1st.– 2019) — Madison, WI, U.S.A. Retrieved from: https://www.icrc 2019.org/uploads/1/1/9/0/119067782/crigspatialandtemporalcharacteristicsofeaswithdelayedparticles.pdf.

11 Argynova A.Kh. The perspective fundamental cosmic rays physics and astrophysics investigations in the Tien-Shan high-mountain scientific station / A.Kh. Argynova, B. Iskakov, V.V. Jukov, K.M. Mukashev, A.D. Muradov, V.V. Piskal, N.O. Saduyev, T.X. Sadykov, N.M. Salihov, A.S. Serikkanov, E.M. Tautaev, F.F. Umarov // News of the National academy of sciences of the Republic of Kazakhstan. Series of geology and technical sciences. — 2019. — Vol. 6 (438). — P.121–138. https://doi.org/10.32014/2019.2518–170X.163.

12 Beisembaev R.U. The «Horizon-T» Experiment: Extensive Air Showers Detection. / R.U. Beisembaev, O.D. Dalkarov, V.A. Ryabov, A.V. Stepanov, M.I. Vildanova, V.V. Zhukov, K.A. Baigarin, D. Beznosko, T.X. Sadykov, N.S. Suleymenov // arxiv: physics.ins-det/1605.05179. — 2016. Retrieved from: https://arxiv.org/ftp/arxiv/papers/1605/1605.05179.pdf

13 Heck D. «CORSIKA»: A Monte Carlo Code to Simulate Extensive Air Showers / D. Heck, J. Knapp, J.N. Capdevielle, G. Schatz, T. Thouw // Forschungszentrum Karlsruhe Report FZKA 6019. — 1998. Retrieved from: https://is.muni.cz/el/sci/jaro2013/F9145/um/40140265/CORSIKA_PHYSICS.pdf

Қ.М. Мұқашев, А.В. Степанов, А.Х. Арғынова, В.В. Жуков, Т.К. Идрисова

Ғарыш сәулесін тіркеуге арналған бірегей жүйені құрудың бір тәсілі туралы

Бүгінгі күні ғарыш сәулесінің физикасын зерттеуге арналған биіктаулы ғылыми станцияда әрқайсысы дербес жұмыс істейтін, баламасы жоқ көптеген дара қондырғылар пайдаланылуда. Мақалада құрамында ғарыш сәулесінің электрон-фотон құраушысын тіркеуге арналған сцинтилляциялық детекторлармен құрылған «кілем», сәуленің нейтрондық құраушыларын тіркеуге арналған жерасты және жерүсті мониторлары, калориметрлер, черенков сәулесінің тіркеуіштері, сцинтилляциялық спектрометрлер, жер сілкінісін қадағалауға арналған қондырғы мен көптеген қосалқы құрылымдарды біріккен бірегей жүйеге айналдырудың әдістері мен техникалық шешімі қарастырылған. Қазіргі заман технологиясының алдыңғы қатарлы жетістіктері мен озық ғылыми пікірлерге сүйену нәтижесінде құрылған ғарыш сәулесін тіркеуге арналған бірегей жүйе шешуші қабілеті жоғары, арнайы дайындалған бағытты бағдарламалар арқылы басқарылатын ортақ мағлұматтар қоры бар, тәуелсіз жұмыс істейтін дербес эксперименталдық маңызды қондырғыларды синхронды түрде басқаруға арналған жүйелік құрылымдармен жабдықталған қондырғыны жинақтап құру принциптері баяндалады. Маңызы ерекше және айрықша күрделі бұл проблеманың іс жүзінде орындалуы нәтижесінде тіркелген ғарыш сәулесі туралы мағлұматтарды мейлінше мұқият талдауға, олардың кеңістікте таралуы, массалық құрамы және энергетикалық құрылымы туралы есептеулерді жоғары дәлдікпен орындау арқылы ақпараттарды бір позициядан суреттеуге мүмкіндік туады. «Горизонт-Т» экспериментальдық қондырғысынан соңғы жылдары алынған алғашқы ғылыми нәтижелер берілген. Жобаны орындау барысында алынған алғашқы деректер қол жеткен нәтижелердің мағлұматтық құндылығының жоғары екендігін дәлелдейді.

Кілт сөздер: ғарыш сәулелері, сцинтилляция детекторы, нейтрон мониторы, талшықты оптика, жергілікті желі, сервер, ауқымды атмосфералық нөсер, бірегей мағлұматтар қоры.

К.М. Мукашев, А.В. Степанов, А.Х. Аргынова, В.В. Жуков, Т.К. Идрисова

Об одном способе организации единой системы регистрации космических лучей

В настоящее время на высокогорной научной станции для исследования физики космических лучей используются различные, независимо действующие уникальные экспериментальные установки. В статье рассмотрены пути и методы объединения этих установок в единую систему, включающую в себя сети сцинтилляционных детекторов типа «ковер» для регистрации электронно-фотонной компоненты, мониторы наземного и подземного базирования для регистрации нейтронных составляющих, калориметры, черенковские детекторы, сцинтилляционный спектрометр и еще ряд подсистем. Вновь созданная единая система регистрации космических лучей на основе достижений современной технологии и научной мысли будет обладать высокой разрешающей способностью, с общим банком данных с обеспечением синхронизации по времени работы отдельных, независимо действующих экспериментальных установок. Решение этой проблемы позволит выполнение детального анализа регистрируемых событий с единой позиции, проведение сложных расчетов пространственного распределения, массового состава, а также энергетической структуры космических лучей с высокой степенью точности. Приведены значимые научные результаты, полученные в последние годы на экспериментальной установке «Горизонт-Т». Представленные предварительные значимые данные в проекте свидетельствуют о высокой информативности полученных результатов.

Ключевые слова: космические лучи, сцинтилляционный детектор, нейтронные мониторы, волоконная оптика, локальная сеть, сервер, широкие атмосферные ливни, единая база данных.

References

1 Zatsepin, G.T., Kuchai, S.A. & Rosenthal, I.L. (1948). Penetrating particles in extensive air showers. *DAN,* 61, 47–49.

2 Zatsepin, G.T. (1949). Nuclear cascade process and its role in the development of extensive air showers. *DAN*. 67, 993–997.

3 Zatsepin, G.T. (1949). On the question of the absorption curve of «primary» particles of cosmic radiation. *ZhETF*. 19, 1104–1107.

4 Zatsepin, G.T., Rosenthal, I.L. & Sarycheva, L.I. (1953). Nuclear interaction of high-energy particles and extensive air showers. *Bulletin of Academy Sciences of the USSR, Physical series,*17, 39–50.

5 Egorov, T.A., Efimov, N.N. & Krasilnikov, D.D. (1965). On the construction of large scintillation counters with one PMT. *Izvestiia AN SSSR, Seria Fizika — Bulletin of AN USSR, Physical series,* 24 (9), 1788–1790.

6 Gunningham, G. (1980). The energy spectrum and arrival direction distributions of cosmic rays with energies above 10^{19} eV. *Aph. J.* 71, 236–239.

7 Suga, K. (1961). Scintillation detector of 4 m^2 area and transistorized amplifier with logarithmic response. *Rev. Sc. Instruments.* 32, 1187–1189.

8 Shinozaki, K. & Teshima, M. (2004). For AGASA Colaboration. AGASA Results. *Nucl. Phys. B (Proc. Suppl.),* 136, 18–27.

9 Tomson, G. (2004). New Results from the HiRes Experiment. *Nucl. Phys. B. (Proc. Suppl.),* 136, 28–39.

10 Beisembaev, R.U., Beisembaeva, E.A., Dalkarov, O.D., & Mosunov, V.D. (2019). The perspective fundamental cosmic rays physics and astrophysics investigations in the Tien-Shan high-mountain scientific station. *36th International Cosmic Ray Conference* -ICRC2019 (July 24th August 1st. 2019). Madison, WI, U.S.A. *icrc org.* Retrieved from https://www.icrc org/uploads/1/1/9/0/119067782/ crigspatial and temporal characteristics of eas with delayed particles.pdf.

11 Argynova, A.Kh., Iskakov, B., Jukov, V.V., Mukashev, K.M. Muradov, A.D, Piskal, V.V., & et al. (2019). The perspective fundamental cosmic rays physics and astrophysics investigations in the Tien-Shan high-mountain scientific station. *News of the National academy of sciences of the Republic of Kazakhstan. Series of geology and technical sciences,* 6 (438), 121–138. Retrieved from https://doi.org/10.32014/2019.2518–170X.163.

12 Beisembaev, R.U., Dalkarov, O.D., Ryabov, V.A., Stepanov, A.V., Vildanova, M.I., Zhukov, V.V., & et al. (2016). The «Horizon-T» Experiment: Extensive Air Showers Detection. arXiv: physics.ins-det/1605.05179. Retrieved from https://arxiv.org/ftp/arxiv/papers/1605/1605.05179.pdf

13 Heck, D., Knapp, J., Capdevielle, J.N., Schatz, G., & Thouw, T. (1998). «CORSIKA»: A Monte Carlo Code to Simulate Extensive Air Showers. *Forschungszentrum Karlsruhe Report FZKA.* 6019. Retrieved from https://is.muni.cz/el/sci/jaro2013/F9145/um /40140265/CORSIKA_PHYSICS.pdf

DOI 10.31489/2021PH4/16-24

UDC 621.785.5, 621.785.3, 669

B.K. Rakhadilov[1,2], R.S. Kozhanova[2,3*], P. Kowalewski[4], D. Baizhan[1,5], Zh.B. Sagdoldina[1], L.G. Zhurerova[1], G.U. Yerbolatova[6]

[1]*Sarsen Amanzholov East Kazakhstan University, Ust-Kamenogorsk, Kazakhstan;*
[2]*«PlasmaScience» LLP, Ust-Kamenogorsk, Kazakhstan;*
[3]*Shakarim University, Semey, Kazakhstan;*
[4]*Wroclaw University of Science and Technology, Wroclow, Poland;*
[5]*Institute of Composite Materials, Ust-Kamenogorsk, Kazakhstan;*
[6]*D. Serikbayev East Kazakhstan Technical University, Ust-Kamenogorsk, Kazakhstan*
*(*E-mail: kozhanovars@yandex.kz)*

Impact of Volume and Surface Heat Treatment on the Structure and Properties of Steel 30HGSA

The work presents the results of a comparative study of volumetric and surface heat treatment impact on the structural-phase states, hardness, and wear resistance of steel 30HGSA. Surface hardening was conducted by the electrolyte-plasma method. Bulk quenching of the samples was carried out by heating to a temperature of 900 °C, followed by cooling in water and oil, and some of the samples after quenching were annealed at a temperature of 510 °C. The structural-phase states of 30HGSA steel samples were studied by metallographic and X-ray structural analysis. There were carried out the microhardness measurements, tribological tests according to the ball-disk scheme, as well as was determined the resistance of the samples to abrasive wear. It was determined that after electrolytic-plasma hardening, fine-acicular martensite with a small content of cementite is formed on the basis of metallographic and X-ray structural analyzes, and coarse-acicular martensite is formed after volume quenching in water and oil. It was determined that the microhardness increased to 400-460 HV after volume quenching, and subsequent annealing leads to a decrease in hardness to 330-360 HV. It was revealed that the electrolyte-plasma surface hardening leads to an increase in microhardness up to 2 times due to the formation of fine-acicular martensite.

Keywords: hardening, annealing, electrolytic plasma treatment, volume quenching, structure, wear resistance, martensite.

Introduction

One of the most effective ways to improve the service characteristics of structural steels is the development of optimal heat-treatment modes. This facilitates to obtain products with certain specified characteristics that meet operational requirements, and, on the other hand, to predict changes in the properties of parts and structures during manufacture and operation [1-3]. The high level of physical and mechanical properties of structural steels, widely used in industry, is due to the martensitic structure [1]. They are subjected to bulk or surface hardening to obtain a martensitic structure in steels. An important place in increasing the durability of a wide class of machine parts is given to the quality of the metal — not of the entire section of the product, but to the structural state and physical and mechanical properties of the surface layer. It is the surface layer that determines the operational properties of parts — wear resistance, strength, material resistance to fatigue, contact endurance, corrosion resistance, etc. Surface treatment technologies with concentrated energy flows are widely used to increase the durability of parts, which have a number of common features that distinguish them favorably from other heat treatment methods. These technologies include the following methods of surface hardening: hardening by electric current induced in the surface layers of the part (HFC or induction hardening); flame hardening of an oxygen-acetylene or gas burner; plasma hardening; hardening by a laser beam; electric arc hardening; quenching in molten metals, electrolytes or salts [4-6]. Among them, plasma hardening has a number of advantages over the existing methods of surface thermal hardening in terms of its technical and economic indicators and the results of comparative analysis. The main advantage of plasma thermal hardening in comparison with laser is that the area of contact of the plasma arc with the material being processed is much larger than that of the laser beam; therefore, less time is spent on processing the surface of the die tooling with this method [3, 6]. One of the promising methods of plasma surface hardening is electrolytic-plasma hardening [7-10], which is one of the varieties of plasma hardening. Heating and cooling of the part is carried out in a water-based electrolyte during electrolytic-plasma hardening. The plasma layer is formed in the gap between the liquid (electrolyte) electrode and the

surface of the product when voltage is applied [10]. The result of a short stay of steel at quenching temperatures, as well as the occurrence of phase transformations in the temperature range above equilibrium, is an increase in the mechanical properties of the material in comparison with bulk quenching. However, the tribological properties of steels treated by electrolytic-plasma hardening have not been sufficiently studied, and there is little information on comparative studies of the wear resistance of steels treated with volumetric heat treatment and surface electrolytic-plasma hardening.

In connection with the above, the purpose of this work is to comparatively research the impact of volumetric and surface heat treatment on the structural-phase states and physical-mechanical properties of steel 30HGSA.

Experimental

Structural alloy steel 30HGSA was chosen as the object of research. Table 1 illustrates the chemical composition of the researched steel.

Table 1

Chemical composition of 30HGSA steel, %

Steel	C	Si	Mn	Ni	S	P	Cr	Cu
30HGSA	0.28-0.34	0.9-1.2	0.8-1.1	till 0.3	till 0.025	till 0.025	0.8-1.1	till 0.3

Samples of 30HGSA steel with the size of 15x15 mm were subjected to volumetric and surface heat treatment. The heat treatment modes are represented in Table 2. Heat treatment was carried out in an evacuated quartz tube in a laboratory tube furnace. Heat treatment of 30HGSA steel samples was carried out in the following modes: quenching from 900 °C, holding time at 900 °C was 0.5 h, cooling was conducted in water and oil, and some of the samples were subjected to annealing at 510 °C with cooling in water and oil. Surface hardening of 30HGSA steel samples was carried out by the electrolytic-plasma method on a setup consisting of a 30 kW direct current source, an electrolytic cell, a bath, a pump, a heat exchanger, and a stainless steel anode [11].

Table 2

Modes of processing 30HGSA steel samples

Sample designation	Volume quenching			Annealing			Surface hardening		
	Heating temperature, T, °C	Holding time t, sec	Cooling environment	Heating temperature, T, °C	Holding time t, sec	Cooling environment	Heating temperature, T, °C	Holding time t, sec	Cooling environment
Q0	-	-	-	-	-	-			
EPH	-	-	-	-	-	-	2 sec	-	water solution
Q1	900	30	water						
Q2	900	30	oil						
Q1A1	900	30	water	510	30	water			
Q2A1	900	30	oil	510	30	water			
Q1A2	900	30	water	510	30	oil			
Q2A2-	900	30	oil	510	30	oil			

The EPH process was carried out in the following mode: the applied voltage between the anode and the sample was 320 V, the current density was 25 A/cm^2, and the plasma exposure time was 2 sec. In this mode, the samples were heated to ~ 850-900 °C. Cooling was carried out in a flowing electrolyte after turning the voltage off. An aqueous solution containing 15% sodium carbonate was used as the electrolyte. Distilled water was used to prepare the electrolyte. The schematic view of the installation for plasma electrolytic processing is shown in Figure 1.

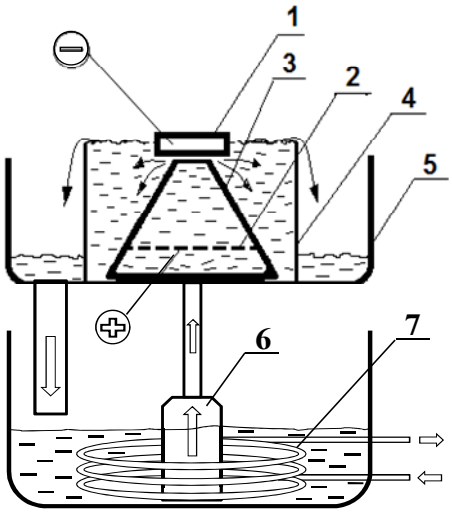

1 - processed sample (cathode), 2 - stainless steel anode with holes, 3 - cone-shaped baffle, 4 - working chamber - electrolyte bath, 5 - pan, 6 - pump, 7 - heat exchanger

Figure 1. Schematic view of the installation of plasma electrolytic treatment

The research of the phase composition of 30HGSA steel samples before and after volumetric and surface hardening was carried out on an X'PertPRO X-ray diffractometer in CuKα-radiation in a continuous recording mode in the range of angles from 20 to 85°. Metallographic analysis was performed in a bright field on an Altami MET 5C microscope at various magnifications. The microhardness of the samples was measured by the method of indentation of a diamond indenter on a PMT-3M device in accordance with GOST 9450-76, at a load of 100 g and holding under a load of 10 s. Tribological tests were carried out on a TRB^3 tribometer with dry friction according to the "ball-disk" scheme (ASTM G133-95 and ASTM G99) under the following conditions: wear radius – 3 mm, friction path – 60 m, sample rotation speed – 2 cm/s , a load of 6 N. Si_3N_4 ball with a diameter of 6 mm was used as a counterbody. Figures 2a-b represent a schematic of the experiment and a general view of the TRB^3 tribometer.

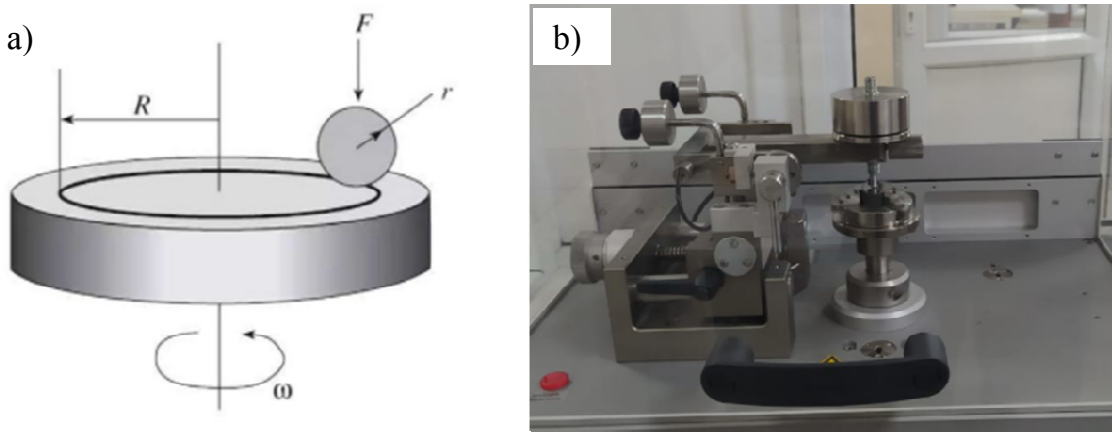

Figure 2. Experiment a schematic (a) and general view of TRB^3 tribometer (b)

Abrasive wear tests of the samples were carried out on an experimental setup for testing abrasive wear when rubbing against loose abrasive particles according to the "rotating roller – flat surface" scheme in accordance with GOST 23.208-79, which coincides with the American standard ASTM C 6568. The surfaces of the samples were ground and polished for testing abrasion on a rubber disc, they were also cleaned with acetone, and dried. A cylindrical rubber roller, pressed by a radial surface against a flat surface of a test specimen with a force of 44 N, rotated at a frequency of 1 s^{-1}. The general and schematic view of the device is shown in Figure 3a-b. The rate of entry of abrasive particles between the rubber wheel and the sample, that is, into the test zone, was 41-42 g/min. Electrocorundum with a grain size of 200-250 μm was used

as abrasive particles. The wear resistance of the treated test piece was evaluated by comparing its wear with that of a reference piece (non-treated piece). The wear was measured by the gravimetric method on an ADV-200 analytical balance with an accuracy of 0.0001 g. The samples were tested for 10 minutes, the total wear length was 96 m, and then, were blown with compressed air to remove the remaining sand particles on the samples before weighing. The wear resistance of the test material was assessed by the loss of the mass of the samples during the test in accordance with GOST 23.20879.

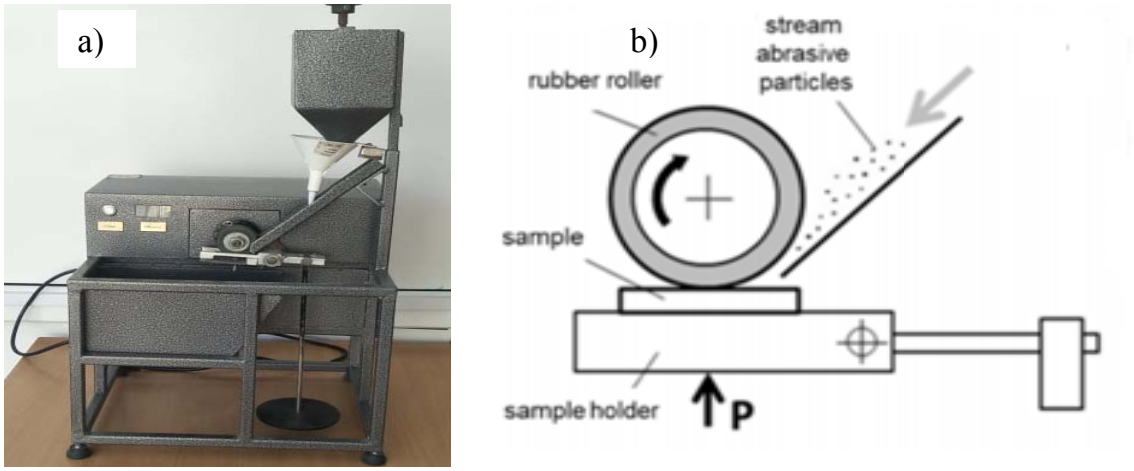

Figure 3. Experiment a schematic (a) and general view (b) of the device for testing materials for abrasive wear

Results and Discussions

Figures 4a-h indicate the microstructure of 30HGSA steel before and after volumetric and surface heat treatment. Metallographic analysis showed that 30HGSA steel in the initial state consists of a ferrite-pearlite structure. A fine-needle martensitic structure is formed after electrolyte-plasma hardening. Coarse-acicular martensite is formed after volumetric quenching with cooling in water and oil. No significant changes are observed in the structure of quenched samples after annealing.

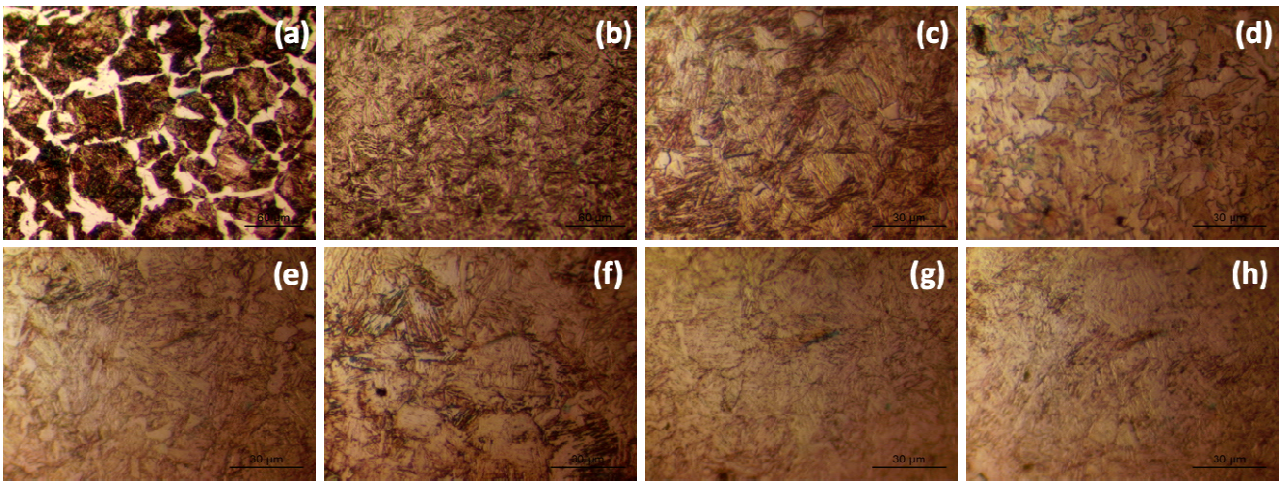

Figure 4. Microstructure of 30HGSA steel samples: Q0-30HGSA (a), EPH-30HGSA (b), Q1-30HGSA (c), Q2-30HGSA (d), Q1A1-30HGSA (e), Q2A1-30HGSA (f), Q1A2-30HGSA (g), Q2A2-30HGSA (h)

The phase composition of the samples was investigated before and after volumetric and surface heat treatment. Figures 5a-h indicate X-ray diffraction patterns of 30HGSA steel samples. X-ray structural analysis demonstrated that in the initial state 30HGSA steel consists of the α-phase. After electrolyte-plasma hardening and volumetric quenching with cooling in oil, the diffractograms of the samples, along with the α-phase, exhibit a reflection (121) of cementite. Only the lines of the α-phase are present on the diffraction patterns of the samples that have passed quenching with cooling in water and quenching with subse-

quent annealing. In this case, in all quenched samples, the diffraction patterns show broadening of the interference lines of the-phase. Broadening of the α-phase interference lines is associated with an increase in the dislocation density, the formation of martensite and is mainly determined by the tetragonality of martensite [12-14]. The largest broadening of the α-phase peaks is observed for the Q1-30HGSA sample, which indicates significant internal stresses due to the high cooling rate. In the samples annealed after quenching, such a large broadening is not observed.

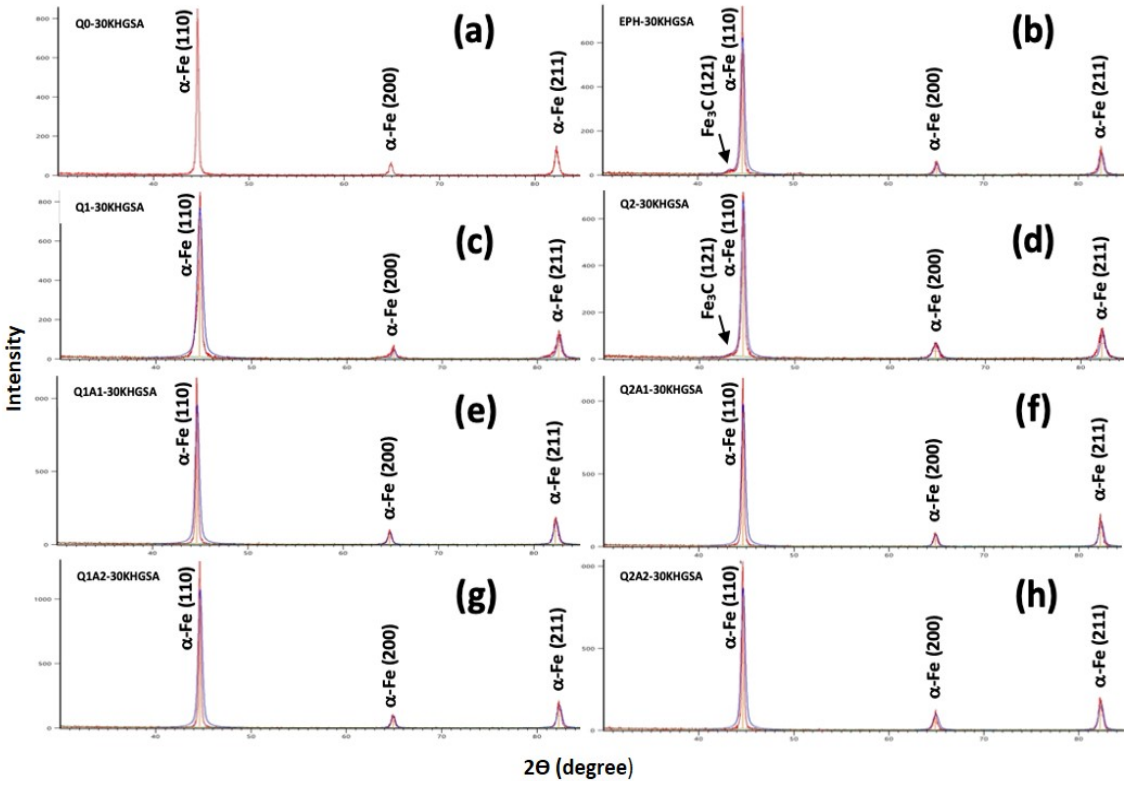

Figure 5. X-ray diffraction patterns of steel 30HGSA: Q0-30HGSA (a), EPH-30HGSA (b), Q1-30HGSA (c), Q2-30HGSA (d), Q1A1-30HGSA (e), Q2A1-30HGSA (f), Q1A2-30HGSA (g), Q2A2-30HGSA (h)

One of the most important properties of the surface layer, which strongly depends on the cooling rate during quenching, is hardness. Therefore, we have studied the changes in the microhardness of 30HGSA steel depending on the mode of heat treatment. Figure 6 represents a histogram of the microhardness of 30HGSA steel before and after volumetric and surface heat treatment. It was identified that the microhardness of steel samples increases after volumetric and surface heat treatment. At the same time, the microhardness increased to 400-460 HV, and subsequent annealing led to a decrease in hardness to 330-360 HV after volume quenching. The decrease in the hardness of quenched samples after annealing is associated with the removal of the internal stress formed during cooling at a high rate.

The maximum increase in hardness is observed in samples treated by plasma electrolyte hardening. An increase in hardness up to 2 times during electrolyte-plasma hardening is associated with the formation of fine-needle martensite. There is no need for annealing due to the small thickness of the hardened layer for steels that have undergone electrolytic-plasma hardening. Only the surface layer with a thickness of 1-2 microns is hardened during electrolytic-plasma hardening, and the base remains viscous. In this case, the hardened layer smoothly passes to the base of the material. Due to the formation of a transition zone – a heat-affected zone, the formed internal stress on the modified layer does not lead to the destruction of the steel material and the appearance of cracks in it.

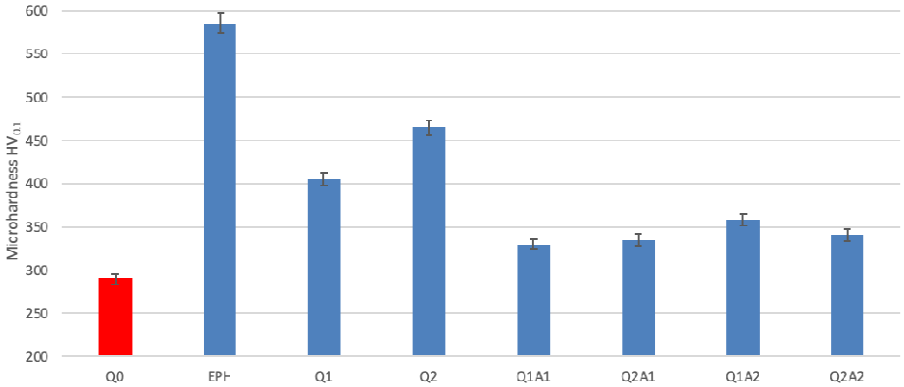

Figure 6. Microhardness of 30HGSA steel before and after surface and volume hardening

Figure 7 designates the results of tribological tests of 30HGSA steel samples according to the "ball-disk" scheme [15]. The wear resistance of the samples was characterized by the coefficient of friction and the volume of wear of the samples. Figure 7a shows the curves of the friction coefficient of the samples before and after treatment. It can be seen from the figure that the samples that have undergone electrolytic-plasma surface hardening and volumetric quenching with cooling in oil have a low coefficient of friction in comparison with the samples that have undergone quenching with cooling in water. In this case, annealing with cooling in oil of the quenched sample leads to a decrease in the coefficient of friction. Specimens quenched with cooling in water and annealing with cooling in water have high values of the coefficient of friction in comparison with the original specimen. Apparently, since steel quenching with cooling in water is accompanied by the formation of structural stresses in the steel this leads to the formation of microcracks under the action of dynamic loads.

Figure 7b represents the results of changes in the volume of wear of the samples before and after treatment. The data on the volume of wear of the samples correlates well with the data on the coefficient of friction of the samples. Samples EPH, Q2 and Q2A2 illustrated low wear volume compared to other samples. The rest of the treated samples showed a high amount of wear compared to the original sample. The low wear volume and coefficient of friction of samples EPH, Q2 and Q2A2 demostrated high wear resistance in dry friction.

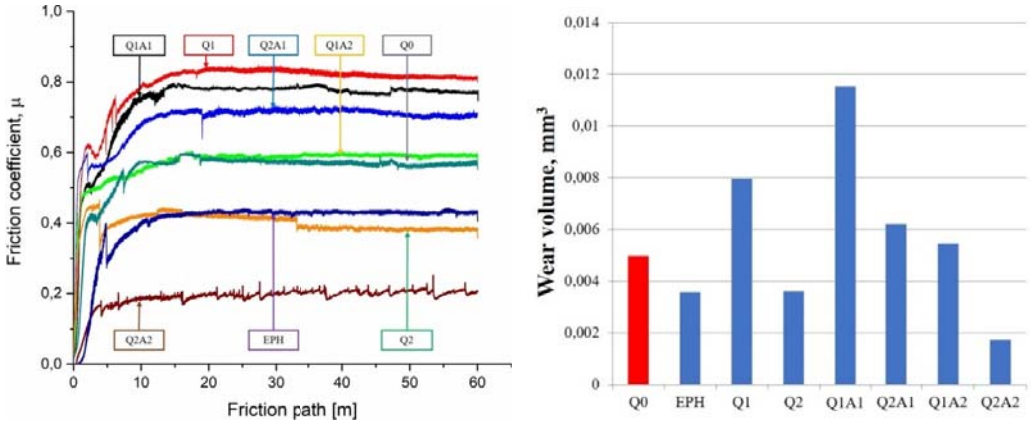

Figure 7. Friction coefficient (a) and wear volume (b) of 30HGSA steel samples before and after surface and volume quenching

Figure 8 demonstrates the results of an abrasive wear test. All samples, except for samples Q1 and Q1A2, showed a low value of weight loss compared to the original sample. At the same time, samples EPH, Q2 and Q2A2 showed high resistance to abrasive wear. The high durability of samples that have undergone electrolyte-plasma surface hardening is associated with the formation of fine-acicular martensite. An increase in the complex of operational properties of steel 30HGSA during electrolytic-plasma hardening is carried out due to saturation of the solid solution with carbon and alloying elements, grain refinement, and an increase in the density of crystal structure defects.

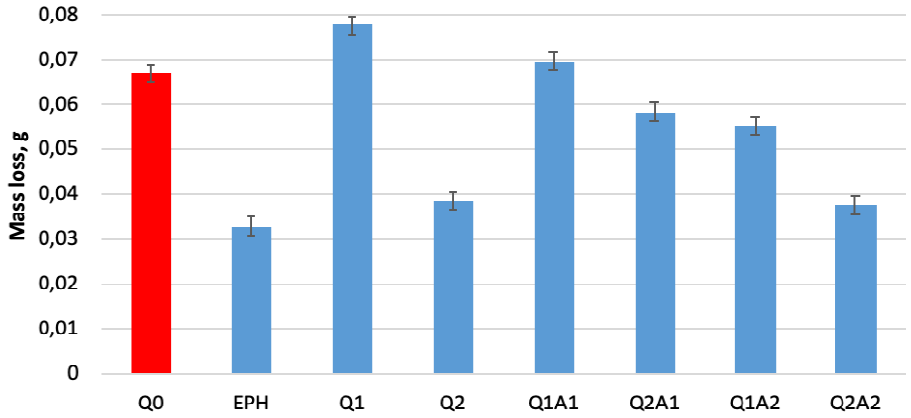

Figure 8. Results of abrasive wear resistance tests of 30HGSA steel samples

Conclusions

It was determined that after electrolytic-plasma hardening, fine-acicular martensite with a small content of cementite is formed on the basis of metallographic and X-ray structural analyses, and coarse-acicular martensite is formed after volume quenching in water and oil. In this case, cementite is observed in the diffractogram after quenching with cooling in water. The cementite dissolves after annealing. No significant changes are observed after annealing in the structure of the samples quenched with cooling in water.

It was analyzed that the microhardness increased to 400-460 HV, and subsequent annealing leads to a decrease in hardness to 330-360 HV after volume quenching. Moreover, due to the formation of fine-acicular martensite the electrolyte-plasma surface hardening leads to an increase in microhardness up to 2 times.

The results of tribological tests of 30HGSA steel specimens before and after heat treatment showed that specimens subjected to electrolytic-plasma surface hardening and volumetric quenching with cooling in oil have a low coefficient of friction in comparison with specimens quenched with cooling in water. It was also determined that samples EPH, Q2 and Q2A2 demonstrated a low wear volume compared to the original sample. Specimens quenched with cooling in water and annealing with cooling in water showed a high volume of wear compared to the original specimen. Apparently, this is due to the fact that quenching and/or annealing of steel with cooling in water is accompanied by the formation of structural stresses in the steel, leading to the formation of microcracks under the action of dynamic loads.

The results of testing samples of steel 30HGSA for resistance to abrasive wear indicated that the samples, except for Q1 and Q1A2, showed a low value of weight loss in comparison with the original sample. At the same time, samples EPH, Q2 and Q2A2 showed high resistance to abrasive wear.

Thus, the tribological properties of parts made of steel 30HGSA can be increased due to the use of heat treatment, including quenching from 900 ºC with cooling in oil, followed by annealing with cooling in oil. Also, surface plasma hardening can be used, which includes heating for 2 seconds followed by cooling in a flowing electrolyte. Electrolytic-plasma surface hardening is a more economical and productive process compared to bulk heat treatment. Concurrently, after electrolytic-plasma surface hardening, the hardness of steel 30HGSA increases by 2 times and tribological properties increase. This is primarily due to the formation of a highly dispersed metastable structure with a higher dislocation density in the surface layer.

Acknowledgments

This research was conducted within the grant financing of scientific research for 2020-2022 years of the Committee of Science of the Ministry of Education and Science of the Republic of Kazakhstan. Grant No. AP08857733.

References

1 Курдюмов В.Г. Превращения в железе и стали / В.Г. Курдюмов, Л.М. Утевский, Р.И. Энтин. — М.: Наука, 1977. — 236 с.

2 Счастливцев В.М. Структура термически обработанной стали / В.М. Счастливцев, Д.А. Мирзаев, И.Л. Яковлева. — М.: Металлургия, 1994. — 288 с.

3 Васильева А.Г. Деформационное упрочнение закаленных конструкционных сталей / А.Г. Васильева. — М.: Машиностроение, 1981. — 231 с.

4 Полетика И.М. Электронно-лучевая закалка поверхностного слоя стали вне вакуума // И.М. Полетика, М.Г. Голковский, М.В. Перовская // Физическая мезомеханика. — 2006. — № 9. — С. 181–184.

5 Смирнова Н.А. Особенности образования структуры при лазерной обработке // Н.А. Смирнова, А.И. Мисюров // Инженер. журн. «Наука и инновации». — 2012. — № 6 (6). — 11 с.

6 Сафонов Е.Н. Плазменная закалка деталей машин: моногр. / Е.Н. Сафонов. — М.; Берлин: Директ-Медиа, 2014. — 165 с.

7 Belkin P.N. Plasma Electrolytic Hardening of Steels: Review // P.N. Belkin, S.A. Kusmanov // Surface Engineering and Applied Electrochemistry. — 2016. — Vol. 52. — No. 6. — P. 531–546. DOI: 10.3103/S106837551606003X.

8 Rakhadilov B.K. Method of Electrolyte-Plasma Surface Hardening of 65G and 20GL Low-Alloy Steels Samples // B.K. Rakhadilov, L.G. Zhurerova, A. Pavlov // IOP Conf. Series: Materials Science and Engineering. — 2016. — V. 142. — P. 1–7.

9 Rakhadilov B.K. The cathodic electrolytic plasma hardening of the 20Cr2Ni4A chromium-nickel steel // B.K. Rakhadilov, V.V. Buranich, Z.A. Satbayeva, Zh.B. Sagdoldina, R.S. Kozhanova, A.D. Pogrebnjak // Journal of Materials Research and Technology. — 2020. — Vol. 9, Issue 4. — P. 6969–6976.

10 Рахимова У.А. Увеличение объема при динамическом нагружении закаленных образцов сплава 110Г13Л / У.А. Рахимова // Вестн. Караганд. ун-та. Сер. Физика. — 2011. — № 1(61). — С. 32–40.

11 Rakhadilov B. Impact of electronic radiation on the morphology of the fine structure of the surface layer of R6M5 steel // B. Rakhadilov, A. Kengesbekov, L. Zhurerova, R. Kozhanova, Z. Sagdoldina // Machines. — 2021. — 9 (2). — P. 1–9.

12 Хомутов О.И. Исследование электролитно-плазменного процесса // О.И. Хомутов, Г.В. Плеханов, С.Д. Терентьев, С.О. Хомутов // Ползуновский альманах. — 2001. — 1, 2. — С. 10–19.

13 Терентьев С.Д. Исследование вольт-амперной характеристики электролитно-плазменного разряда // С.Д. Терентьев, Г.В. Плеханов // Вузовская наука в современном мире: Тез. докл. Междунар. науч.-техн. конф. — 1999. — С. 118, 119.

14 Райзер Ю.П. Распространение разрядов и поддержание плотной плазмы электромагнитными полями // Успехи физ. наук. — 1972. — Т. 108. — Вып. 3. — С. 429–461.

15 Юров В.М. Некоторые вопросы физики сухого трения / В.М. Юров, С.А. Гученко // Вестн. Караганд. ун-та. Сер. Физика. — 2011. — № 1(61). — С. 50–57.

Б.К. Рахадилов, Р.С. Кожанова, П. Ковалевский,
Д. Байжан, Ж.Б. Сагдолдина, Л.Г. Журерова, Г.У. Ерболатова

30ХГСА болатының құрылымы мен қасиеттеріне көлемді термиялық өңдеу мен электролитті-плазмалық беткі шынығудың әсері

Мақалада 30ХГСА болатының құрылымдық-фазалық күйлеріне, қаттылығы мен тозуға төзімділігіне, көлемді және беттік термиялық өңдеудің әсерінің салыстырмалы зерттеу нәтижелері келтірілген. Беткі қатаю электролитті-плазмалық әдіспен жүзеге асырылды. Үлгілердің көлемді қатаюын 900°С температураға дейін қыздыру арқылы жүргізілген, содан кейін суда және майда, сондай-ақ, қатаюдан кейінгі үлгілердің бір бөлігі 510°С температурада салқындатылады. Металлографиялық және рентгендік талдау әдістерімен 30ХГСА болат үлгілерінің құрылымдық-фазалық күйлері зерттелді. Микроқаттылықты өлшеу, шар-диск схемасы бойынша трибологиялық сынақтар жүргізілді, сондай-ақ, үлгілердің абразивтік тозуға төзімділігі анықталды. Металлографиялық және рентгенқұрылымдық талдаулар негізінде электролитті-плазмалық шынығудан кейін құрамында аз цементит бар ұсақ инелі мартенсит, ал көлемді шынығудан кейін суда және майда түзілетіні белгілі болды. Көлемді қатаюдан кейін микроқаттылықтың 400-460 HV дейін жоғарылағаны анықталды, содан кейін күйдіру қаттылықтың 330-360 HV дейін төмендеуіне әкеледі. Электролитті-плазмалық беткі қатаю ұсақ инелі мартенситтің пайда болуы есебінен микроқаттылықты 2 есеге дейін арттыруға әкелетіні дәлелденген.

Кілт сөздер: беріктендіру, қыздырып босаңдату, көлемдік шынықтыру, электролитті-плазмалық өңдеу, құрылым, желінугетөзімділік, мартенсит.

Б.К. Рахадилов, Р.С. Кожанова, П. Ковалевский, Д. Байжан,
Ж.Б. Сагдолдина, Л.Г. Журерова, Г.У. Ерболатова

Влияние объемной термической обработки и электролитно-плазменной поверхностной закалки на структуру и свойства стали 30ХГСА

В статье представлены результаты сравнительного изучения влияния объемной и поверхностной термической обработки на структурно-фазовые состояния, твердость и износостойкость стали 30ХГСА. Поверхностная закалка осуществлялась электролитно-плазменным методом. Объемная закалка образцов проведена нагревом до температуры 900°С с последующим охлаждением в воде и в масле, а также

часть образцов после закалки подвергнута отжигу при температуре 510°С. Были изучены структурно-фазовые состояния образцов стали 30ХГСА методами металлографического и рентгеноструктурного анализа. Проведены измерение микротвердости, трибологические испытания по схеме «шар–диск», а также была определена стойкость образцов к абразивному изнашиванию. На основе металлографического и рентгеноструктурного анализа определено, что после электролитно-плазменной закалки формируется мелкоигольчатый мартенсит с небольшим содержанием цементита, а после объемной закалки в воде и в масле формируется крупноигольчатый мартенсит. После объемной закалки микротвердость увеличивалась до 400–460 HV, а последующий отжиг приводил к уменьшению твердости до 330–360HV. Выявлено, что электролитно-плазменная поверхностная закалка приводит к увеличению микротвердости до 2 раз за счет формирования мелкоигольчатого мартенсита.

Ключевые слова: упрочнение, отжиг, объемная закалка, электролитно-плазменная обработка, структура, износостойкость, мартенсит.

References

1 Kurdiumov, V.G., Utevskii, L.M. & Entin, R.I. (1977). *Prevrashcheniia v zheleze i stali [Transformations in iron and steel]*. Moscow: Nauka [in Russian].

2 Schastlivtsev, V.M., Mirzaev, D.A. & Yakovleva, I.L. (1994). *Struktura termicheski obrabotannoi stali [Structure of heat-treated steel]*. Moscow: Metallurgiia [in Russian].

3 Vasileva, A.G. (1981). *Deformatsionnoe uprochnenie zakalennykh konstruktsionnykh stalei [Deformation hardening of hardened structural steels]*. Moscow: Mashinostroenie [in Russian].

4 Poletika, I.M., Golkovskii, M.G. & Perovskaia, M.V. (2006). Elektronno-luchevaia zakalka poverkhnostnogo sloia stali vne vakuuma [Electron-beam hardening of the surface layer of steel outside the vacuum]. *Fizicheskaia mezomekhanika — Physical mesomechanics*, 9, 181–184 [in Russian].

5 Smirnova, N.A. & Misiurov, A.I. (2012). Osobennosti obrazovaniia struktury pri lazernoi obrabotke [Features of structure formation during laser processing]. *Inzhenernyi zhurnal «Nauka i innovatsii» — Engineering Journal: Science and Innovation*, 6 (6), 11 [in Russian].

6 Safonov, E.N. (2014). *Plazmennaia zakalka detalei mashin [Plasma hardening of machine parts]*. Moscow; Berlin: Direkt-Media [in Russian].

7 Belkin, P.N. & Kusmanov, S.A. (2016). Plasma Electrolytic Hardening of Steels: Review. *Surface Engineering and Applied Electrochemistry*, Vol. 52., No. 6., 531–546. Retrieved from DOI: 10.3103/S106837551606003X.

8 Rakhadilov, B.K., Zhurerova, L.G. & Pavlov A. (2016). Method of Electrolyte-Plasma Surface Hardening of 65G and 20GL Low-Alloy Steels Samples. *IOP Conf. Series: Materials Science and Engineering,* V. 142, 1–7.

9 Rakhadilov, B.K., Buranich, V.V., Satbayeva, Z.A., Sagdoldina, Zh.B., Kozhanova, R.S., & Pogrebnjak, A.D. (2020). The cathodic electrolytic plasma hardening of the 20Cr2Ni4A chromium-nickel steel. *Journal of Materials Research and Technology*, Vol. 9, Issue 4, 6969–6976.

10 Rakhimova, U.A. (2011). Uvelichenie obema pri dinamicheskom nagruzhenii zakalennykh obraztsov splava 110G13L [Increase in volume under dynamic loading of quenched specimens of alloy 110G13L]. *Vestnik Karagandinskogo universiteta. Seriia Fizika — Bulletin of the Karagandy University. Physics Series*, 1 (61), 32–40 [in Russian].

11 Rakhadilov, B., Kengesbekov, A., Zhurerova, L., Kozhanova, R., & Sagdoldina. Z. (2021). Impact of electronic radiation on the morphology of the fine structure of the surface layer of R6M5 steel. *Machines*. 9 (2), 1–9.

12 Khomutov, O.I., Plekhanov, G.V., Terentev, S.D., & Khomutov, S.O. (2001). Issledovanie elektrolitno-plazmennogo protsessa [Investigation of the electrolyte-plasma process]. *Polzunovskii almanakh — Polzunovsky Almanac*, 1–2, 10–19 [in Russian].

13 Terentev, S.D. & Plekhanov, G.V. (1999). Issledovanie volt-ampernoi kharakteristiki elektrolitno-plazmennogo razriada [Investigation of the volt-ampere characteristics of an electrolyte-plasma discharge]. *Vuzovskaia nauka v sovremennom mire: Tezisy dokladov Mezhdunarodnoi nauchno-tekhnicheskoi konferentsii — University science in the modern world: Abstracts of reports of the international scientific and technical conference*, 118, 119 [in Russian].

14 Raizer, Yu.P. (1972). Rasprostranenie razriadov i podderzhanie plotnoi plazmy elektromagnitnymi poliami [Propagation of discharges and maintenance of dense plasma by electromagnetic fields]. *Uspekhi fizicheskikh nauk — Achievements of physical sciences, 108, 3,* 429–461 [in Russian].

15 Yurov, V.M. & Guchenko, S.A. (2011). Nekotorye voprosy fiziki sukhogo treniia [Some questions of the physics of dry friction]. *Vestnik Karagandinskogo universiteta. Seriia Fizika — Bulletin of the Karagandy University. Physics Series*, 1 (61), 50–57 [in Russian].

DOI 10.31489/2021PH4/25-34

UDC 539.013

V.M. Yurov[1*], V.I. Goncharenko[2,3], V.S. Oleshko[2], K.M. Makhanov[1]

[1]*Karaganda University of the name of academician E.A. Buketov, Kazakhstan;*
[2]*Moscow Aviation Institute (National Research University), Moscow, Russia;*
[3]*Institute for Management Problems. V.A. Trapeznikov RAS, Moscow, Russia*
*(*e-mail: exciton@list.ru)*

Anisotropy of the surface energy of silicides of some metals

An empirical model of a solid surface is proposed in the article. The thickness of the surface layer is described in terms of one parameter – the atomic volume of an element or its compounds. Surface energy is also expressed through one parameter – the melting point of a chemical element or crystal. The model proposes equations that allow calculating the thickness of the surface layer and surface energy for each face of the crystal. As an example, calculations of these values are made for silicides of some metals with crystal structures of cubic, hexagonal and rhombic systems. For cubic silicides, the thickness of the surface layer is 3-9 nm, and the number of monolayers is 7-16. Studies of metal deposition on silicon faces have shown that silicon silicide is formed on the (111) face, which has the highest surface energy. The reaction on the (100) face occurs only on the oxidized surface. In hexagonal silicides, anisotropy is seen, both in the values of the thickness of the surface layer and in the values of the surface energy. For example, during the formation of chromium disilicide on the (111) face in the *c* direction, it was found that the sizes of the islands become larger than on the (001) face. The authors designate that the thickness of the surface layer and the specific surface energy for cubic, hexagonal, and rhombic crystals significantly differ from them. What is the difference? First, the difference between the atoms of chemical elements from the periodic table and their compounds depends, first of all, on their electronic structure, which forms this or that interaction potential. Secondly, the difference between cubic, hexagonal and rhombic crystals lies in their relationship with Poisson's ratio and Young's modulus, that is, on two material parameters. Third, the thickness of the surface layer between cubic, hexagonal, and rhombic crystals also differs in only one parameter – the atomic (molar) volume of the crystal. However, the analysis of all the patterns still needs to be carefully analyzed.

Keywords: metal silicide, surface energy, thickness of the surface layer, solid, chemical element, crystal, surface layer, Poisson's ratio, Young's modulus.

Introduction

Silicides are compounds that are similar to metals. They have a good electrical conductivity, thermal conductivity and even superconductivity at low temperatures. Silicides in the silicon-metal system do not have a simple chemical bond in the structure of interstitial phases and do not fulfill the Hagg relation [1]. Due to the significant radius of silicon atoms, its high solubility by transition metals in structures and solid solutions is observed by the type of substitution. In metals with significant atomic radii, complex silicide structures are formed with a prevailing covalent bond of silicon atoms. With the transition of metals to groups VII and VIII, the structures of silicides become simpler. Disilicides of metals such as tantalum, zirconium, vanadium, chromium, niobium silicon form layered structures as curved nets. In the formation of silicides from transition metals, the decisive role is played by covalent bonds, which resonate between the electronic states of the s and d orbitals. The fact that the d-orbitals are empty leads to a large number of observed silicide structures.

When silicon forms solid solutions, its atom is transformed into +4 ion due to ionization. Such a solid solution has orthogonal symmetry and creates body-centered (bcs) structures with many metals from the periodic table.

Transition metal silicides are relevant today in microelectronics and nanoelectronics because of their low electrical resistivity and high melting temperature. Contacts for integrated circuits, thin thermal stable film connections, Schottky diodes and more. All this dictates the relevance of studies of diffusion processes in metal-silicon systems and the conditions for the formation of metal silicides [2]. Transition metal silicides have thermal and mechanical strength, which decreases when going from titanium to tungsten.

During the deposition of a metal coating on silicon at its initial stage, silicides of different chemical composition, different structural composition and intermediate phases can be formed at the interface. It all depends on the type of metal applied, its characteristics, temperature, and other thermodynamic parameters, crystallization kinetics, and much more.

Metal-silicon structures, which are widely used in microelectronics for soft X-ray radiation, contain a layer thickness in the nanoscale range. Therefore, it is believed that the nanometer thickness of metal silicides will provide the key to understanding many processes.

In this work, based on an empirical model, we present the values of the thickness of the surface layer of silicides, which can be experimentally determined by the methods of "grazing" X-rays [2], as well as the anisotropy of the surface energy for various faces, which was determined by us for the first time.

The difference in the radii of the metal and silicon atoms leads to a significant difference in their diffusion, which is determined by the activation energy, which, in turn, depends on the specific energy for each silicon face. This means that in order to understand the processes occurring during the formation of silicides either due to metal diffusion or due to its crystallization, it is necessary to know the specific surface energy and its anisotropy for silicides of some metals.

With regard to surface energy, we present several recent works that have been performed theoretically. In work [3], the surface characteristics of some metals were obtained using the traditional method of electron density, but using new test functions at the vacuum-metal interface. This method gave good agreement with the anisotropic behavior of some metals.

In work [4], the anisotropy of the metal in the s-surface layer was estimated by the electronic statistical method. In this case, considering the dispersion forces on the edges of the metal, the theory of E.M. Lifshitz calculates the attraction of molecules in the condensed phase and allows to determine the interaction energy through the constants of a solid.

In [5], a method was proposed for determining a layer thickness on the surface of a crystal that melts at the melting temperature. In this case, the thickness means the first coordination sphere of atoms, which is perpendicular to the surface. It facilitates to estimate the anisotropy of the surface energy of metals. In the same work, a model of the coordination melting of a solid was proposed, which made it possible to relate the surface energy to the physical properties of the crystal.

Experimental

Five silicides V_3Si, *FeSi, CoSi, MnSi,* Mg_2Si, which have a cubic crystal lattice, were selected as objects of study.

Trivanadium silicide V_3Si is produced by condensation of silicon and vanadium vapors in vacuum. In this case, gray crystals of a cubic system are formed with a superconductivity temperature of about 17.2 K. It can be used in magnetic devices in electrical engineering.

Iron silicide *ε-FeSi* forms yellow cubic crystals. It is part of ferrosilicon, which is used in the deoxidation of all steels. It is used for alloying structural and transformer steel grades. In [6], the formation of iron silicide on the silicon (100) and (111) faces was studied, similarly to how it was shown in [2]. It turned out that if iron is deposited on the (111) face, then it immediately interacts with this face, forming an *ε-FeSi* silicide of the cubic system. However, on the (100) face, iron first forms a solid solution, which passes into the *Fe3Si* phase.

Cobalt silicide *CoSi* is obtained from the solid phase with copper silicide at a temperature of 1500 °C. These are gray crystals of a cubic system. In [7], the formation of silicides upon the deposition of cobalt was studied on the silicon faces (100), (110) and (111). When a cobalt film less than 0.7 nm is applied, a cobalt silicide layer of about 0.17 nm is formed. Upon annealing a nanometer-thick substrate above 300 ºC, four silicide phases arise – nonmagnetic *CoSi*, Co_2Si, $CoSi_2$, and ferromagnetic Co_3Si.

Manganese silicide *MnSi* has a gray cubic crystal, the lattice of which does not contain inversion symmetry. In other words, its unit cell is not combined with itself by mirror reflection, and at low temperatures skyrmions are formed, first discovered by German physicists in 2009 [8]. Skyrmions have a nonzero topological charge (N = 1) and are highly localized (magnetic skyrmions are 50-100 nm in size). In [9], the initial stage of growth of manganese films on the (100) and (111) silicon faces at room temperature was studied. When 0.6 nm of manganese is deposited, a 0.1 nm thick monosilicide layer is formed. Upon annealing a silicon crystal, on the face of which 2.5 nm manganese was deposited, manganese monosilicide and a *Mn-Si* solid solution were formed. The formation of these silicide films took place at temperatures of 200-400 ºC. When manganese silicide is heated above 600 ºC, it turns into semiconducting silicide $MnSi_{17}$.

Magnesium silicide Mg_2Si is a blue crystal of a cubic system and a semiconductor material with a band gap of 0.76 eV. It is used as heat-to-electricity converters in silicon technology. In [10], the deposition of coatings on the (111) face was investigated at a magnesium deposition rate of about 0.06 nm / min. In this case, three stages of the formation of coatings appeared at the interface. The first stage is the formation of

clusters of magnesium atoms. In the second stage, magnesium silicide increases. The third stage illustrates the growth of metallic magnesium.

Five silicides Ti_5Si_3, $NbSi_2$, $TaSi_2$, $CrSi_2$, $MoSi_2$, which have a crystal lattice of hexagonal syngony. Titanium silicide Ti_5Si_3 is a hexagonal structure and has a high melting point, which makes it a heat-resistant material [11].

Niobium silicide (disilicide) $NbSi_2$ forms crystals of a hexagonal system. The metal sublattice has a hexagonal closest packing, and six octahedral voids are occupied by silicon atoms and their arrangement is ordered. The structure is constructed, so that the niobium atom contains six silicon atoms, which are surrounded by three niobium atoms $(NbSi_2)$. The $NbSi_2$ structure is located between silicides with silicon chains and layers of silicon atoms. In [12], the formation of $NbSi_2$ disilicide is established during the diffusion of silicon through the interface during electron beam evaporation to the silicon (111) face in vacuum. The thickness of the layer depends on the temperature during bombardment of the target with argon ions, which turned out to be maximum at T = 773 K. The absence of the influence of the energy of argon ions on the diffusion of niobium into flint suggests that radiation does not affect the formation of niobium silicides.

Tantalum silicide (disilicide) $TaSi_2$ forms crystals of a hexagonal system. It has metallic conductivity, while silicon has no free electrons in the $TaSi_2$ silicide. This leads to the appearance of a polarization dipole moment. Tantalum silicide has a high melting point (2200 ºC), low electrical resistance, high modulus of elasticity. It is used in Schottky barriers, ohmic contacts of integrated circuits. The interaction of conducting tantalum disilicide $TaSi_2$ with semiconducting silicon Si leads to the formation of Janus-like nanoparticles $TaSi_2/Si$ [13].

Chromium silicide (disilicide) $CrSi_2$ has a hexagonal structure with three chromium atoms in a unit cell and 6 silicon atoms. Chromium disilicide $CrSi_2$ is an indirect-gap semiconductor with a band width of 0.35 eV at points *L* and *M*. At point *L*, there is a gap with a band width of 0.52 eV. In [14], chromium films 30 nm thick were deposited on the silicon (111) face by magnetron sputtering in a vacuum setup. The formation of a $CrSi_2$ layer at a temperature of about 400 ºC, which has a resistivity of about 1.2 mΩ x cm and a Schottky barrier height of about 0.6 V.

Molybdenum silicide (disilicide) $MoSi_2$ contains a tetragonal structure. Each unit cell contains 2 molybdenum atoms and 4 silicon atoms. Along the z axis, a change of double dense layers of silicon atoms with layers of molybdenum atoms is observed. In other words, silicon atoms form a structure in the voids of which molybdenum atoms are located. Molybdenum disilicide $MoSi_2$ has two polymorphic modifications – α-*MoSi2* has a tetragonal structure and β-$MoSi_2$ has a hexagonal structure. The hexagonal structure is a metastable phase, while the tetragonal structure, on the contrary, is a stable phase [15], as evidenced by the fact that the bond between molybdenum and silicon atoms is much stronger than between *Si* - *Si* atoms.

Five silicides $ZrSi_2$, $HfSi_2$, $FeSi_2$, Co_2Si, Ni_2Si, which have a rhombic crystal lattice, were selected as the third objects of study.

Zirconium silicide (disilicide) $ZrSi_2$ forms rhombic crystals. In [16], the zirconium coating on the (100) face of silicon was investigated when the latter was irradiated with an electron beam with a density of 8-10 J/cm^2. Zirconium disilicide $ZrSi_2$ with a size of 40-50 nm is formed at the interface.

Hafnium silicide (disilicide) *HfSi2* is a substance of the rhombic system. It is obtained by spraying pure hafnium with a magnetron or laser onto silicon. The quality of silicon silicide *HfSi2* is investigated experimentally.

Iron silicide (disilicide) $FeSi_2$ is a β-$FeSi_2$ crystal of rhombic system. The quality of semiconductor iron disilicide depends on the material purity and the level of defects present. Electron beam evaporation of β-$FeSi_2$ shows better results than magnetron coating. The band diagram of β-$FeSi_2$ illustrates a direct transition at 0.74 eV at the Λ point, which is in the middle between the Γ-*Z* points [17].

Dicobalt silicide Co_2Si forms gray rhombic crystals. It was established in [18] that the hydrogen evolution reaction on the dicobalt Co_2Si electrode proceeds according to the Langmuir type.

Dinickel silicide Ni_2Si is a white rhombic crystal.

In [19], we showed that the thickness $R(I)_M$ of the surface layer of an atomically smooth crystal can be estimated by the formula:

$$R(I)_i = 0.24 \cdot 10^{-9} \cdot \upsilon(\text{nm}), \quad (1)$$

where the molar (atomic) volume of the crystal $\upsilon = M/\rho$, M is the molar (atomic) mass (g/mol), ρ is the density (g/cm^3) of the crystal. These values are given in the periodic table and in many reference books.

For example, for silicon Si, the molar mass is M = 28.086 (g/mol), the density is ρ = 2.33 (g/cm^3), then $R(I)_M$ = 2.9 nm. The experimental value of the silicon layer thickness measured by the method of grazing X-rays is 3.1 nm, which does not differ from our value with the experimental error. With formula (1), $R(I)_M$ of all elements of the periodic system can be calculated. It turned out that this value does not exceed 5-7 nm, that is, all the elements of the periodic system are nanostructure. As for silicon, its crystal lattice constant is a = 0.54307 nm. This means that on the thickness of silicon $R(I)_M$ there are monolayers in the amount of $n = R(I)_M/a \approx 6$. In other words, silicon is reconstructed on these 6 monolayers, which was discovered experimentally.

According to the empirical model [19] for the surface energy σ of the crystal face, we obtained:

$$\sigma(\mathrm{hkl}) = 10^{-3} \cdot T_\mathrm{m} \cdot \mathrm{l(hkl)}, \tag{2}$$

where *Tm* is the melting point of the crystal, and l *(hkl)* for crystals with body-centered (bcc) and face-centered (fcc) cubic structures is given by relations (3):

$$\begin{aligned} &\mathrm{Im3m},\ Z = 2;\ \mathrm{l}_{100} = \mathrm{a};\ \mathrm{l}_{110} = \mathrm{a}\sqrt{2};\ \mathrm{l}_{111} = \mathrm{a}/\sqrt{3}, \\ &\mathrm{Fd3m},\ Z = 4;\ \mathrm{l}_{100} = \mathrm{a};\ \mathrm{l}_{110} - \mathrm{a}/\sqrt{2};\ \mathrm{l}_{111} = 2\mathrm{a}/\sqrt{3}. \end{aligned} \tag{3}$$

It is necessary to write equations (1) and (2), taking into account the anisotropy of crystals, the directions of the crystal faces. Let us write them out finally:

$$\begin{aligned} \mathrm{R(I)}_{\mathrm{x=a}} &= 0.54 \cdot 10^{-11} \cdot \mathrm{x(a)}^3, \\ \mathrm{R(I)}_{\mathrm{y=b}} &= 0.54 \cdot 10^{-11} \cdot \mathrm{y(b)}^3, \\ \mathrm{R(I)}_{\mathrm{z=c}} &= 0.54 \cdot 10^{-11} \cdot \mathrm{z(c)}^3. \end{aligned} \tag{4}$$

$$\begin{aligned} \sigma_\mathrm{a} &= 10^{-3} \cdot \mathrm{T_m} \cdot \mathrm{R_a(I)/R(I)} \\ \sigma_\mathrm{b} &= 10^{-3} \cdot \mathrm{T_m} \cdot \mathrm{R_b(I)/R(I)} \\ \sigma_\mathrm{c} &= 10^{-3} \cdot \mathrm{T_m} \cdot \mathrm{R_c(I)/R(I)}. \end{aligned} \tag{5}$$

Results and Discussion

We will consider the thickness of the surface layer and the surface energy of silicides of the cubic, hexagonal, rhombic systems and compare them. Table 1 demonstrates 5 silicides having a cubic structure. The thickness of the surface layer for cubic filicides is 3-9 nm, and the number of monolayers is 7-16. For monosilicides it is equal to 7. These *FeSi, CoSi, MnSi* crystals have a structure of reduced dimensionality of the skyrmion type [8], in which the crystal lattice does not contain inversion symmetry (Fig. 1).

Table 2

Thickness of the surface layer and anisotropy of the surface energy of silicides cubic system

Compound	(hkl)	Syngonia	T_m, K	$R(I)_M$, nm	σ_{hkl}, μJ/m^2
V_3Si	100	Cubic	2003	7.6 (16)	2.003
	110				1.431
	111				2.289
FeSi	100	Cubic	1678	3.2 (7)	1.678
	110				1.199
	111				1.918
CoSi	100	Cubic	1600	3.3 (7)	1.600
	110				1.143
	111				1.829
MnSi	100	Cubic	1548	3.4 (7)	1.548
	110				1.106
	111				1.769
Mg_2Si	100	Cubic	1358	9.5 (15)	1.358
	110				0.970
	111				1.552

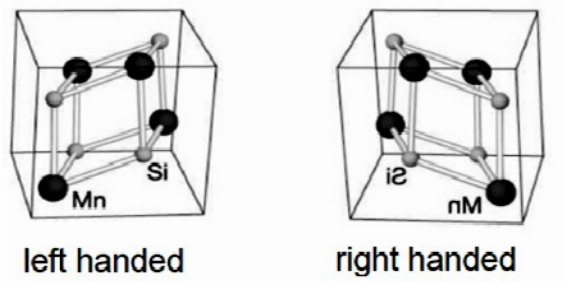

Figure 1. Unit cell of manganese silicide *MnSi*

Studies of metal deposition (especially *FeSi* and *CoSi*) on the silicon face have shown [6-10] that the formation of silicon silicide occurs on the (111) face with the highest surface energy (Table 1). The reaction on the (100) face occurs only on the oxidized surface.

Table 2 represents the thickness of the surface layer and the surface energy of the silicides of the hexagonal system.

In Table 2, the thickness $R(I)_M$ is calculated by the formula (2), and the thickness $R(I)_a$ and $R(I)_c$, as well as σa and σc are calculated by the formula (4) and (5). A noticeable anisotropy is seen both in the values of the thickness of the surface layer and in the values of the surface energy. For example, during the formation of chromium disilicide $CrSi_2$ on the (111) face in the c direction, it was found that the sizes of the islands become larger than on the (001) face (Fig. 2) [20].

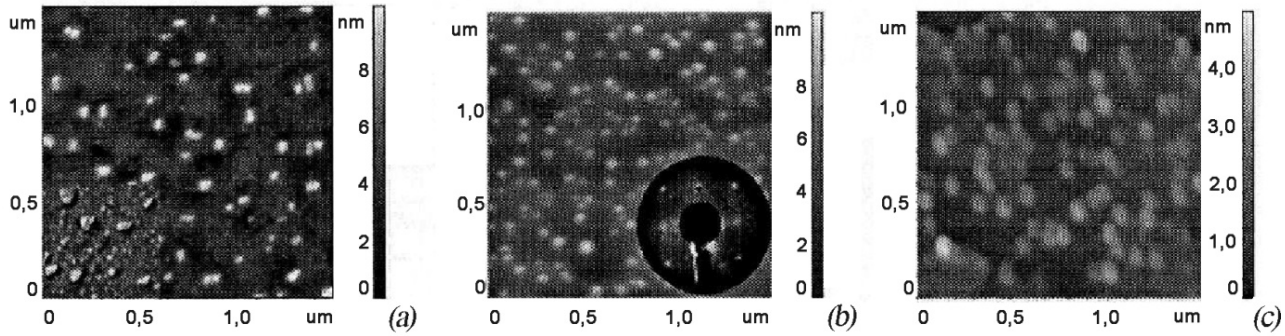

Figure 2. AFM surface of $CrSi_2$ obtained on the *Si* (001) face by reactive epitaxy (a) and solid-phase epitaxy (b) and on the *Si* (111) face obtained by reactive epitaxy (c) [20]

T a b l e 2

Thickness of the surface layer and anisotropy of the surface energy of silicides hexagonal system

Compound	Syngonia	T_m, K	ρ, g/sm^3	M, g/mol	$R(I)_M$, nm	$R(I)_a$, nm	$R(I)_c$, nm	σ_a, J/m^2	σ_c, J/m^2
Ti_5Si_3	hexagonal	2407	4.32	322.6	17.9	7.3 (14)	22.2 (30)	0.982	2.985
$NbSi_2$	hexagonal	2223	5.66	149.08	6.30	5.9 (12)	15.4 (23)	2.082	5.434
$TaSi_2$	hexagonal	2473	9.1	237.0	6.25	5.9 (12)	15.2 (23)	2.335	6.014
$CrSi_2$	hexagonal	1823	5.0	108.167	5.19	4.7 (11)	14.0 (22)	1.651	4.918
$MoSi_2$	hexagonal	2293	6.31	152.11	5.79	1.8 (6)	26.3 (33)	0.714	10.416

This, as in the case of cubic crystals, means that the (111) face of silicon is more reactive than the other faces.

In Table 3, the thickness $R(I)_M$ is calculated by the formula (2), and the thicknesses $R(I)_a$, $R(I)_b$ and $R(I)_c$, as well as σ_a, σ_b and σ_c are calculated by the formula (4) and (5).

Table 3

Thickness of the surface layer and anisotropy of the surface energy of silicides rhombic system

Compound	Syngonia	T_m, K	$R(I)_M$, nm	$R(I)_a$, nm	$R(I)_b$, nm	$R(I)_c$, nm	σ_a, J/m^2	σ_b, J/m^2	σ_c, J/m^2
$ZrSi_2$	rhombic	1973	7.3	2.8 (8)	153.3 (108)	2.8 (8)	0.757	41.433	0.757
$HfSi_2$	rhombic	2023	7.1	2.7 (7)	166.7 (114)	2.7 (7)	0.679	47.498	0.679
$FeSi_2$	rhombic	1483	5.3	52.1 (53)	26.6 (34)	33.2 (42)	14.578	7.443	9.290
Co_2Si	rhombic	1868	4.8	11.8 (24)	2.8 (8)	19.3 (13)	4.492	1.090	7.511
Ni_2Si	rhombic	1591	4.8	19.0 (27)	6.7 (13)	2.8 (8)	6.298	2.221	0.928

Table 3 demonstrates that the $ZrSi_2$ and $HfSi_2$ crystals behave in a similar way. In the $R(I)_b$ direction, a large thickness of the surface layer is observed, leading to the formation of a dendritic structure (Fig. 3). A large surface energy is also observed on this edge.

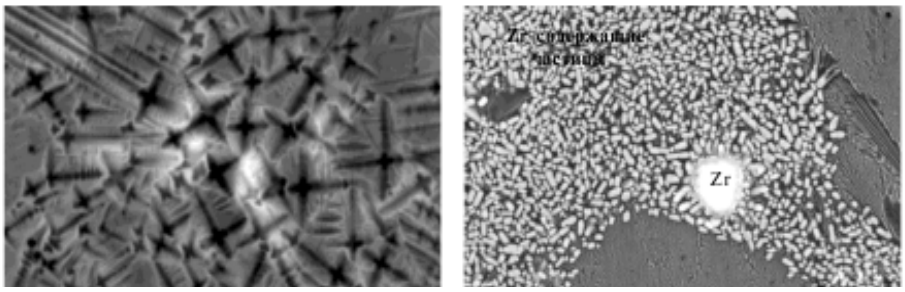

Figure 3. SEM images of the area of the dendritic structure (a) and eutectic (b) on the silicon surface during the formation of $ZrSi_2$ [16]

The thickness of the surface layer of iron disilicide $FeSi_2$ is approximately the same in all directions. This leads to spherical symmetry when grinding $FeSi_2$ in a planetary mill (Fig. 4).

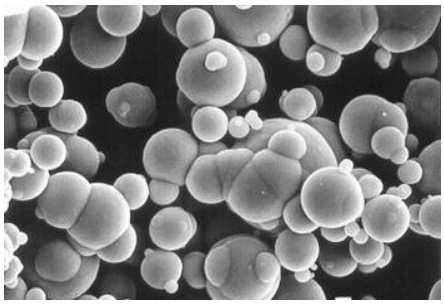

Figure 4. $FeSi_2$ in a planetary mill [21]

Figure 5 indicates an image of a nickel disilicide similar to cobalt disilicide. Image (a) describes a Ni_2Si silicide domain, where faces (b) and (c) represent the silicon silicide lattice as viewed from directions (a) and (b). It also shows the faces (101) – orange, (010) – blue, (110) – black lines. Silicon atoms Si, designated A and B at the Ni_2Si/Si interface, are shown by black spheres. Images (d) – (e) indicate layers of silicon atoms Si at the Ni_2Si/Si interface in unstressed and deformed states. The black and white atoms represent Si atoms in the Ni_2Si plane with Si end groups, and the yellow spheres represent the atoms of the Si substrate.

Overall, based on tables 1-3 it was identified that the thickness of the surface layer and specific surface energy for cubic, hexagonal and rhombic crystals have significant differences. First, the difference between the atoms of chemical elements from the periodic table and their compounds depends, first of all, on their electronic structure, which forms one or another interaction potential (such works have just begun to be studied, for example, work [22]). In this work, a pair potential was constructed, which showed that a hexagonal structure turns out to be a more favorable structure than a face-centered cubic one. Second difference between cubic, hexagonal and rhombic crystals is in their relationship with Poisson's

ratio and Young's modulus, that is, on two material parameters [23-24]. Third, the thickness of the surface layer between cubic, hexagonal, and rhombic crystals also differs only in one parameter — the atomic (molar) volume of the crystal [19]. However, the analysis of all patterns still needs to be carefully analyzed.

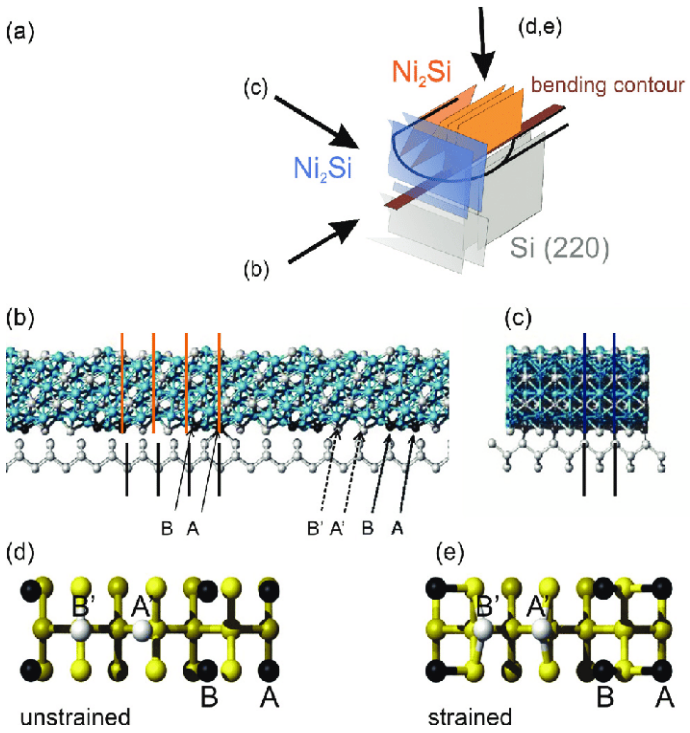

Figure 5. Nickel disilicide Ni_2Si [21]

Conclusions

In our proposed empirical model of atomically smooth metals [19] for silicon silicides of cubic, hexagonal, and rhombic systems, the thickness of the surface layer and the surface energy of the crystal faces are calculated. The average thickness of the studied crystals $R(I)_M$ does not exceed 10 nm, that is, it is a nanostructure. There is a large spread in the thicknesses in directions a, b, c of hexagonal and rhombic silicides, as well as their surface energy. This spread is associated with a change in the pair interaction potentials between atoms and a change in their Young's modulus.

Acknowledgements

The work was carried out under the program of the Ministry of Education and Science of the Republic of Kazakhstan Grants No. 0118RK000063 and No. F.0780.

References

1 Seibt M. Electronic states at dislocations and metal silicide precipitates in crystalline silicon and their role in solar cell materials / M. Seibt, R. Khalil, V. Kveder, W. Schruter // Appl. Phys. A. — 2009. — Vol. 96. — P. 235–253.

2 Zubarev E.N. Effect of working gas pressure on the formation of mixed zones in Mo/Si multilayer X-ray mirrors fabricated by magnetron sputtering / E.N. Zubarev // Advances in physical sciences. — 2011. — Vol. 181. — No. 5. — P. 491–501.

3 Глушков В.Л. Характеристики поверхности щелочных металлов с учетом дискретности кристаллической решетки и фриделевских осцилляций электронной плотности / В.Л. Глушков, О.С Еркович // Вестн. МГТУ им. Н.Э. Баумана. Сер. Естественные науки. — 2017. — Вып. 73. — № 4. — С. 75–89.

4 Shebzukhova I.G. Anisotropy of surface energy and electron work function IIB of metals / I.G. Shebzukhova, L.P. Arefieva // Physical and Chemical Aspects of Study of Clusters Nanostructures and Nanomaterials. — 2020. — No. 12. — P. 319.

5 Bokarev V.P. Anisotropy of physicochemical properties of single-crystal surfaces / V.P. Bokarev, G.Ya. Krasnikov // Electronic technology. Series 3. Microelectronics. — 2016. — No. 4 (164). — P. 25–32.

6 Gomoyunova M.V. Formation of ultrathin layers of iron silicides on the surface of monocrystalline silicon / M.V. Gomoyunova, I.I. Pronin, D.E. Malygin, N.R. Gall, D.V. Vyalikh, S.L. Molodtsov // Surf. Sci. — 2006. — Vol. 600. — P. 2449–2457.

7 Tsay J.S. Microscopic interfacial structures and magnetic properties of ultrathin Co⁄Si (111) Co⁄Si (111) films / J.S. Tsay, T.Y. Fu, M.H. Lin, C.S. Yang, Y.D. Yao // Appl. Phys. Lett. — 2006. — Vol. 88. — P. 102–113.

8 Mühlbauer S. Skyrmion lattice in a chirial magnet / S. Mühlbauer, B. Binz, F. Jonietz, C. Pfleiderer, A. Rosch, A. Neubauer, R. Georgii, P. Boeni // Science. — 2009. — Vol. 323. — P. 915–928.

9 Gomoyunova M.V. Formation of manganese silicides on the Si (111) 7x7 surface / M.V. Gomoyunova, G.S. Grebenyuk, I.I. Pronin, B.V. Senkovsky, D.V. Vyalykh // Solid State Physics. — 2015. — Vol. 57. — No. 3. — P. 609–618.

10 Galkin K.N. Electrical properties of two-dimensional iron layers in ordered phases Si (111) 7x7 and Si (111) 2x2-fe / K.N. Galkin, S.A. Dotsenko, N.G. Galkin // Chemical Physics and Mesoscopy. — 2009. — Vol. 11. — No. 3. — P. 334–342.

11 Grigorenko S.G. Titanium intermetallic compounds. Features, properties, application (Review) / S.G. Grigorenko, G.M. Grigorenko, O.M. Zadorozhnyuk // Modern electrometallurgy. — 2017. — № 3 (128). — P. 51–63.

12 Afonin N.N. Properties of thin films based on iron oxide and titanium formed on single-crystal silicon / N.N. Afonin, V.A. Logacheva, Yu.S. Shramchenko, A.M. Khoviv // Journal of Inorganic Chemistry. — 2011. — Vol. 56. — No. 5. — 821–832.

13 Sotiriou G.A. Janus-Like Plasmonic-Magnetic Nanoparticles / G.A. Sotiriou, A.M. Hir, P.Y. Lozach, A. Teleki, F. Krumeich, S.E. Pratsinis // Chem. Mater. — 2011. — Vol. 23 (7). — P. 1985–1993.

14 Соловьев Я.А. Влияние температуры быстрой термической обработки на электрофизические свойства пленок никеля на кремнии / Я.А. Соловьев, В.А. Пилипенко // Докл. БГУИР. — 2020. — № 18 (1). — С. 81–88.

15 Jiang D.E. Prediction of strong adhesion at the $MoSi_2$/Fe interface / D.E. Jiang, A. Emily, E.A. Carter // Acta Materialia. — 2015. — Vol. 53. — P. 4489–4497.

16 Angles V.V. Synthesis of multicomponent nanocrystalline coatings based on titanium nitride in arc low-pressure discharges / V.V. Angles, N.N. Koval, Yu.F. Ivanov, Yu.A. Petukhov, A.V. Kalin, A.D. Teresov // Surface. X-ray, synchrotron and neutron research. — 2013. — No. 3. — P. 57–64.

17 Filonov A.B. Semiconductor silicides: properties and prospects of application / A.B. Filonov, V.E. Borisenko, W. Henrion, H. Lange // Journal of Luminescence. — 1999. — Vol. 80. — 479–493.

18 Кичигин В.И. Исследование механизма катодных процессов на силицидах кобальта методом электрохимической импедансной спектроскопии / В.И. Кичигин, А.Б. Шеин // Вестн. ТГУ. Сер. Химия. — 2013. — Вып. 18. — № 5. — С. 2209–2215.

19 Yurov V.M. Surface layer thickness, surface energy, and atomic volume of an element / V.M. Yurov, S.A. Guchenko, V.C. Laurinas // Physical and chemical aspects of studying clusters, nanostructures and nanomaterials. — 2018. — No. 10. — P. 691–701.

20 Galkin N.G. Silicon-silicide quasi-zero dimensional heterostructures for silicon based photonics, opto- and thermoelectronics / N.G. Galkin, D.L. Goroshko, E.A. Chusovitin, K.N. Galkin // Physics Status Solidi C. — 2013. — Vol. 10. — P. 1670–1683.

21 Alberti A. Role of the early stages of Ni-Si interaction on the structural properties of the reaction products / A. Alberti, A. La Magna // J. Appl. Phys. — 2013. — Vol. 114. — P. 121–301.

22 Podolskaya E.A. Description of the geometry of crystals with a hexagonal close-packed structure based on pair interaction potentials / E.A. Podolskaya, A.M. Krivtsov // Solid State Physics. — 2012. — Vol. 54. — 1327–1334.

23 Гольдштейн Р.В. Ауксетическая механика кристаллических материалов / Р.В. Гольдштейн, В.А. Городцов, Д.С. Лисовенко // Механика твердого тела. — 2010. — № 4. — С. 43–54.

24 Yurov V.M. Structural phase transition in surface layer of metals / V.M. Yurov, S.A. Guchenko, V.Ch. Laurinas, O.N. Zavatskaya // Bulletin of the Karagandy University – Physics Series. — 2019. — № 1 (93). — P. 50–60.

В.М. Юров, В.И. Гончаренко, В.С. Олешко, Қ.М. Маханов

Кейбір металдардың силицидтерінің беттік энергиясының анизотропиясы

Мақалада қатты дене бетінің эмпирикалық моделі ұсынылған. Элементтің атомдық көлемі немесе оның қосылыстары беттік қабаттың қалыңдығы бір параметр арқылы өрнектелген. Сонымен қатар химиялық элементтің немесе кристалдың балқу температурасы беттік энергияда бір параметр арқылы өрнектелді. Модельде кристалдың әр қыры үшін беттік қабаттың қалыңдығы мен беттік энергияны есептеуге мүмкіндік беретін теңдеулер ұсынылған. Мысал ретінде кубты, гексогональды және ромбтық сингониялы кристалдық құрылымға ие кейбір металдардың силицидтері үшін осы шамалардың есептеулері жасалды. Кубтық силицидтерде беттік қабаттың қалыңдығы 3–9 нм, ал моноқабаттар саны 7–16 құрайды. Кремний беттеріне металды тұндыру үрдісін зерттеулер көрсеткендей, кремний силицидінің қалыптасуы, беттік энергиясы ең жоғары болатын (111) қырда түзіледі. (100) қырында реакция тек тотыққан бетінде жүреді. Гексагональды силицидтерде, беттік қабаттың қалыңдықтарының шамаларында да, сондай–ақ, беттік энергия шамаларында да елеулі анизотропия байқалады. Мысалы, хром-дисилицидін (111) қырында қалыптастырғанда, *c* бағытындағы аралдардың өлшемдері (001) қырдағыға қарағанда үлкен болатыны байқалған. Авторлар мақалада кубтық, гексогональдық және ромбтәрізді кристалдар үшін беттік қабаттың қалыңдығы мен беттік меншікті энергияның бір–бірінен едәуір айырмашылығы бар екендігін көрсеткен. Айырмашылық неде? Біріншіден, периодтық кестедегі химиялық элементтердің атомдарымен олардың қосындыларының арасындағы айырмашылық, ең алдымен олардың өзара әрекеттесу потенциалын құрайтын электрондық құрылымына байланысты. Екіншіден, кубтық, гексогональдық және ромбтәрізді кристалдар арасындағы айырмашылық олардың Пуассон коэффициентімен және

Юнг модулімен байланыстарына қатысты, демек, олар екі материалдық параметрден. Үшіншіден, кубтық, гексогональдық және ромбтәрізді кристалдар арасындағы беттік қабаттың қалыңдығы да тек бір параметрмен — кристалдың атомдық (молярлық) көлемімен ерекшеленеді. Дегенмен, барлық заңдылықтарды талдау нәтижелері зерттеу жұмыстарын әлі де мұқият орындауды қажет етеді.

Кілт сөздер: металл силициді, беттік энергия, беттік қабаттың қалыңдығы, қатты дене, химиялық элемент, кристалл, беттік қабат, Пуассон коэффициенті, Юнг модулі.

В.М. Юров, В.И. Гончаренко, В.С. Олешко, К.М. Маханов

Анизотропия поверхностной энергии силицидов некоторых металлов

В статье предложена эмпирическая модель поверхности твердого тела. Толщина поверхностного слоя показана через один параметр — атомный объем элемента или его соединений. Поверхностная энергия выражена также через один параметр — температуру плавления химического элемента или кристалла. В модели предложены уравнения, которые позволяют вычислить толщину поверхностного слоя и поверхностную энергию для каждой грани кристалла. В качестве примера сделаны расчеты этих величин для силицидов некоторых металлов, имеющих кристаллическую структуру кубической, гексагональной и ромбической сингонии. У кубических силицидов толщина поверхностного слоя составляет 3–9 нм, а число монослоев — 7–16. Исследования нанесения металла на грани кремния показали, что формирование силицида кремния происходит на грани (111), обладающей наибольшей поверхностной энергией. Реакция на грани (100) наблюдается только на окисленной поверхности. У гексагональных силицидов видна заметная анизотропия, как в значениях толщин поверхностного слоя, так и в величинах поверхностной энергии. Например, при формировании дисилицида хрома на грани (111) в направлении *c* обнаружено, что размеры островков становятся больше, чем на грани (001). Авторами показано, что толщина поверхностного слоя и удельная поверхностная энергия для кубических, гексагональных и ромбических кристаллов существенно от них отличаются. В чем заключается различие? Во-первых, отличие между атомами химических элементов из периодической таблицы и их соединениями зависит, прежде всего, от их электронного строения, формирующего тот или иной потенциал взаимодействия. Во-вторых, разница между кубическими, гексагональными и ромбическими кристаллами состоит в их связи с коэффициентом Пуассона и модулем Юнга, то есть зависит от двух материальных параметров. В-третьих, толщина поверхностного слоя между кубическими, гексагональными и ромбическими кристаллами также отличается только одним параметром — атомным (молярным) объемом кристалла. Однако анализ всех закономерностей нужно тщательно перепроверить.

Ключевые слова: силицид металла, поверхностная энергия, толщина поверхностного слоя, твердое тело, химический элемент, кристалл, поверхностный слой, коэффициент Пуассона, модуль Юнга.

References

1 Seibt, M., Khalil, R., Kveder, V., & Schruter W. (2009). Electronic states at dislocations and metal silicide precipitates in crystalline silicon and their role in solar cell materials. *Appl. Phys.A.,* 96, 235–253.

2 Zubarev, E.N. (2011). Effect of working gas pressure on the formation of mixed zones in Mo/Si multilayer X-ray mirrors fabricated by magnetron sputtering. *Advances in physical sciences*, 181, 5, 491–501.

3 Glushkov, V.L. & Erkovich, O.S. (2017). Kharakteristiki poverkhnosti shchelochnykh metallov s uchetom diskretnosti kristallicheskoi reshetki i fridelevskikh ostsilliatsii elektronnoi plotnosti [Characteristics of the surface of alkali metals taking into account the discreteness of the crystal lattice and Friedel oscillations of the electron density]. *Vestnik MGTU imeni N.E. Baumana. Seriia Estestvennye nauki — Bulletin of N.E. Bauman University. Series Natural Sciences, Vol. 73, 4*, 75–89 [in Russian].

4 Shebzukhova, I.G. & Arefieva, L.P. (2020). Anisotropy of surface energy and electron work function IIB of metals. *Physicochemical aspects of studying clusters, nanostructures and nanomaterials*, 12, 319.

5 Bokarev, V.P., & Krasnikov, G.Ya. (2016). Anisotropy of physicochemical properties of single-crystal surfaces. *Electronic technology. Series 3. Microelectronics*, 4 (164), 25–32.

6 Gomoyunova, M.V., Pronin, I.I., Malygin, D.E, Gall, N.R., Vyalikh, D.V., & Molodtsov, S.L. (2006*).* Formation of ultrathin layers of iron silicides on the surface of monocrystalline silicon. *Surf. Sci.,* 600, 2449–2457.

7 Tsay, J.S., Fu, T.Y., Lin, M.H., Yang, C.S., & Yao, Y.D. (2006). Microscopic interfacial structures and magnetic properties of ultrathin Co⁄Si (111) Co⁄Si (111) films. *Appl. Phys. Lett.,* 88, P. 102–113.

8 Mühlbauer, S., Binz, B., Jonietz, F., Pfleiderer, C., Rosch, A., & Neubauer, A., et al. (2009*).* Skyrmion lattice in a chirial magnet. *Science*, 323, 915–928.

9 Gomoyunova, M.V., Grebenyuk, G.S., Pronin, I.I., Senkovsky, B.V., & Vyalykh, D.V. (2015). Formation of manganese silicides on the Si (111) 7x7 surface. *Solid State Physics*, 57, 3, 609–618.

10 Galkin, K.N., Dotsenko, S.A. & Galkin, N.G. (2009). Electrical properties of two-dimensional iron layers in ordered phases Si (111) 7x7 and Si (111) 2x2-fe. *Chemical Physics and Mesoscopy*, 11, 3, 334–342.

11 Grigorenko, S.G., Grigorenko, G.M. & Zadorozhnyuk, O.M. (2017). Titanium intermetallic compounds. Features, properties, application (Review). *Modern electrometallurgy*, *3* (128), 51–63.

12 Afonin, N.N., Logacheva, V.A., Shramchenko, Yu.S., & Khoviv, A.M. (2011). Properties of thin films based on iron oxide and titanium formed on single-crystal silicon. *Journal of Inorganic Chemistry*, 56, 5, 821–832.

13 Sotiriou, G.A., Hir, A.M., Lozach, P.Y., Teleki, A., Krumeich, F., & Pratsinis, S.E. (2011). Janus-Like Plasmonic-Magnetic Nanoparticles. *Chem. Mater.*, 23 (7), 1985–1993.

14 Soloviev, Ya.A., & Pilipenko, V.A. (2020). Vliianie temperatury bystroi termicheskoi obrabotki na elektrofizicheskie svoistva plenok nikelia na kremnii [Influence of conditions of rapid heat treatment on the electrophysical properties of thin chromium films on silicon]. *Doklady BGUI — Reports of BSUIR*, *18(1),* 81–88 [in Russian].

15 Jiang, D.E., Emily, A. & Carter, E.A. (2005). Prediction of strong adhesion at the $MoSi_2$/Fe interface. *Acta Materialia*, 53, 4489–4497.

16 Angles, V.V., Koval, N.N., Ivanov, Yu.F., Petukhov, Yu.A., Kalin, A.V., & Teresov, A.D. (2013). Synthesis of multicomponent nanocrystalline coatings based on titanium nitride in arc low-pressure discharges. *Surface. X-ray, synchrotron and neutron research*, 3, 57–64.

17 Filonov, A.B., Borisenko, V.E., Henrion, W., & Lange, H. (1999). Semiconductor silicides: properties and prospects of application. *Journal of Luminescence*, 80, 479–493.

18 Kichigin, V.I. & Shein, A.B. (2013). Issledovanie mekhanizma katodnykh protsessov na silitsidakh kobalta metodom elektrokhimicheskoi impedansnoi spektroskopii [Study of the mechanism of cathodic processes on cobalt silicides by the method of electrochemical impedance spectroscopy]. *Vestnik TGU. Khimiia — Bulletin of TSU. Chemistry*, *Vol. 18, 5,* 2209–2215 [in Russian].

19 Yurov, V.M, Guchenko, S.A. & Laurinas, V.C. (2018). Surface layer thickness, surface energy, and atomic volume of an element. *Physical and chemical aspects of studying clusters, nanostructures and nanomaterials*, 10, 691–701.

20 Galkin, N.G., Goroshko, D.L., Chusovitin, E.A., & Galkin, K.N. (2013). Silicon-silicide quasi-zero dimensional heterostructures for silicon based photonics, opto- and thermoelectronics. *Physica Status Solidi C.,* 10, 1670–1683.

21 Alberti, A. & La Magna, A. (2013). Role of the early stages of Ni-Si interaction on the structural properties of the reaction products. *J. Appl. Phys.*, 114, 121–301.

22 Podolskaya, E.A. & Krivtsov, A.M. (2012). Description of the geometry of crystals with a hexagonal close-packed structure based on pair interaction potentials. *Solid State Physics*, 54, 1327–1334.

23 Goldstein, R.V., Gorodtsov, V.A. & Lisovenko, D.S. (2010). Aukseticheskaia mekhanika kristallicheskikh materialov [Auxetic Mechanics of Crystalline Materials]. *Mekhanika tverdogo tela — Mechanics of Solids, 4,* 43–54 [in Russian].

24 Yurov, V.M., Guchenko, S.A., Laurinas, V.Ch., & Zavatskaya, O.N. (2019). Structural phase transition in surface layer of metals. *Bulletin of the Karagandy University – Physics*, 1 (93), 50–60.

DOI 10.31489/2021PH4/35-45

UDC: 677.017

V.G. Zdorenko[1], V.Yu. Kucheruk[2], S.V. Barilko[1*], S.N. Lisovets[3]

[1]National Technical University of Ukraine "Igor Sikorsky Kyiv Polytechnic Institute";
[2]Vinnytsia National Technical University;
[3]V.I.Vernadsky Taurida National University
([*]E-mail: poo4ta@bigmir.net)

Non-contact Ultrasound Method of Thread Tension Determination for Light Industry Machinery

It has been established that with the help of a pulsed ultrasonic signal of complex shape, it is possible to determine the tension of a filament with a high linear density in a special waveguide with a rectangular cross-section. It has been proved that the amplitude ratios of ultrasonic waves that interact with different textile filaments are influenced by their linear density, the angle between the passage direction of part of the waves enveloping the fibers in the middle and the surface of these fibers, as well as the angle between the direction of wave propagation enveloping the thread itself from the outside, and the surface of the whole material. It should be noted that the corresponding bypass angles of the ultrasonic waves of the textile depend on the material porosity, frequency of the ultrasonic waves, and their power. To enable non-contact control of the change in the tension of the thread branch, it is advisable to use a pulsed ultrasonic signal with two different peaks of the waves, amplitudes, which are adjusted to the linear density of the thread and its conditional radius. Additionally, the use of this method will provide operational technological control in the production of textile fabrics.

Keywords: thread tension, amplitude ratios, ultrasound waves, waveguide, a linear density of thread, basis weight, textile fabrics.

Introduction

One of the most important tasks for light industry enterprises is to improve the quality of textile products and their competitiveness. Nowadays, the quality of various textile fabrics depends on the main technological parameters, the provision of which facilitates to obtain its proper level.

One of the main parameters is the basis weight of fabrics. Compliance with the appropriate basis weight of fabrics depends on the thread tension on textile machines on which fabrics are made. Due to the excessive tension of threads, their breakage on the process of equipment can occur, which leads to the lack of fabrics, downtime of textile machines, and loss of funds and time to restart them. Nowadays as the thread tension control systems on various textile machines are mostly only mechanical [1, 2], this allows to determine the actual value of this parameter in the course of such systems and to make the correct adjustments with the necessary precision, which can significantly affect the quality of the finished product.

Experimental

There are contact devices for determining the thread tension [3], but they do not allow their installation without affecting the textile material. This leads to an additional increase in tension when measuring it, which can make a significant error from the contact pressure of the sensor on the material itself. There are also optical non-contact devices for determining various parameters of threads [2, 4], but they can have significant errors due to the dustiness of the environment in the production environment.

The creation of ultrasound non-contact methods and means for determining the thread tension on different textile machines will allow operational technological control of this parameter and will provide feedback to the thread tension control systems, which will be adjusted to the actual value of this parameter. This will eliminate the shortcomings of the thread tension systems and improve the quality and competitiveness of the finished fabrics.

Results and Discussion

The movement of threads with a certain tension on the working bodies of knitting machines is the movement on guides of various shapes. If we consider such interaction of a thread with a cylindrical guide with the radius of curvature R [5], it is possible to use the amplitude ratios of ultrasound waves [6] that in-

teract with a thread to determine the tension by changing the diameter of the thread and its density (may vary by means of reducing the interfibrous porosity of the material). In general, the dependence for determining the tension of the leading thread branch by amplitude ratios of ultrasound waves reflected from the fibers of the material to the waves that only fall on it in its interaction with the working bodies of knitting machines can be represented as follows:

$$P_1 = P_0 + \left(R + r^*\right)\left(e^{\mu_T \phi_T} - 1\right) \times$$
$$\times \left(R + \left(1 - \frac{P_0 \cdot \left(R + r^*\right)}{P_0 r^* + E_1 b_k \cdot \left(R + r^*\right)^2} \right) \cdot r^* \right)^{-1} \times$$
$$\times \left(P_0 - \frac{B_0}{2} \cdot \left(R + \left(1 - \frac{P_0 \cdot \left(R + r^*\right)}{P_0 r^* + E_1 b_k \cdot \left(R + r^*\right)^2} \right) \cdot r^* \right)^{-2} \right), \quad (1)$$

$$r^* = \frac{2 Z_1 \cdot \sqrt{\frac{1}{\left| W_{T\text{з.}} \right|^2} - 1}}{\pi^2 f \rho_2 \cdot \cos \nu_{\text{з.}}}. \quad (2)$$

where P_0 is the tension of the driven thread branch; P_1 is the tension of the leading thread branch; R is the radius of curvature of the cylindrical guide; Z_1 is the acoustic air resistance; f is the frequency of ultrasound vibrations; ρ_2 is the bulk density of the tread; $\left| W_{T\text{з.}} \right| = P_{1w} / P_{01w}$ is the ratios of the pressure amplitude P_{1w} of ultrasound waves passing through the fibers of the thread material to the pressure amplitude P_{01w} of waves that just fall on it taking into account the attenuation; $\nu_{\text{з.}}$ is the angle between the direction of the part of the waves that surround the thread and its surface; r^* is the conventional radius of the thread, which is determined by the non-contact ultrasound sensor; μ_T is the coefficient of friction of the thread; ϕ_T is the angle of circumference of the thread of the guide surface; E_1 is the modulus of thread elasticity during compression; b_k is the width of trace contact thread on the guide; B_0 is the coefficient of thread rigidity when bent.

In such cases, it is necessary to use ultrasound waves that pass through the fibers of the material, as well as those that bypass the thread itself. To increase sensitivity of the sensors, it is advisable to use waveguides to determine the thread tension on different knitting machines.

Methods of control of various properties of textile fibers [7-10] do not let carry out operative technological control of the thread tension. Therefore, an amplitude method based on the developed method of controlling technological parameters of textile materials can be applied to control this parameter [11, 12]. The new method is characterized by the fact that the change in the amplitude of ultrasound waves in the waveguide determines the tension of the thread with high linear density on knitting machines.

In practice, it is advisable to use low-power sensors and corresponding waveguides to increase the sensitivity of the ultrasound waves toward the change of the diameter of the thread. Waveguides with a rectangular section are effective.

Fig. 1 represents surfaces depicting the dependence of the amplitude ratios of ultrasound waves $\left| W_{T\text{з.}} \right|$ on the tension of the P_0 driven and P_1 leading thread branch for cotton materials, viscose threads, capron threads, wool.

Fig. 2 illustrates the surfaces that depict the dependence of the amplitude ratios of ultrasound waves $\left| W_{T\text{з.}} \right|$ on the conventional radius of the thread r^* and the parameter $\cos \nu_{\text{з.}}$ that shows the influence of the part of the waves which surround the thread and its fibers (if large interfibrous porosity is present). It should be noted that Figures 1 and 2 show surfaces for different materials (cotton, viscose threads, capron threads, wool) which depict dependence of amplitudes of the ultrasound waves that surround the thread (since this is a large part of the ultrasound signal at which the amplitude detector of the thread tension detector captures voltage that is proportional to the amplitude of the waves transmitted to the sensor).

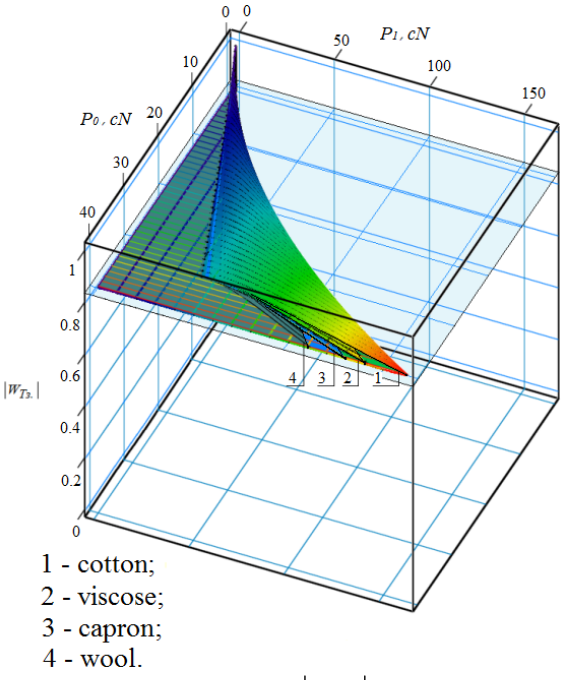

1 - cotton;
2 - viscose;
3 - capron;
4 - wool.

Figure 1. Surfaces showing dependence of ratios $|W_{Tз.}| = P_{1w} / P_{01w}$ of the pressure amplitude P_{1w} of ultrasound waves passing through the fibers of the thread material to the pressure amplitude P_{01w} of waves that just fall on material on the tension P_0 and P_1 for different threads:

1 – dependence $|W_{Tз.}|$ on tension parameters P_0 and P_1 for cotton;
2 – dependence $|W_{Tз.}|$ on tension parameters P_0 and P_1 for viscose threads;
3 – dependence $|W_{Tз.}|$ on tension parameters P_0 and P_1 for capron threads;
4 – dependence $|W_{Tз.}|$ on tension parameters P_0 and P_1 for wool.

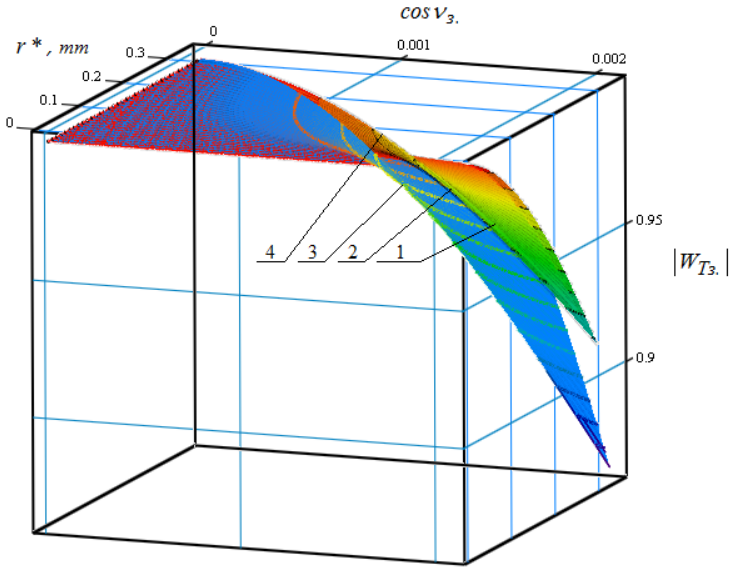

Figure 2. Surfaces showing dependence of ratios $|W_{Tз.}| = P_{1w} / P_{01w}$ of the pressure amplitude P_{1w} of ultrasound waves passing through the fibers of the thread material to the pressure amplitude P_{01w} of waves that just fall on material on parameters r^* and $\cos\nu_{з.}$ for different threads

These surfaces will let simplify the obtained formulas for practical implementation of non-contact means of thread tension control using special waveguides.

In the research course, it has been found out that the amplitude ratios of ultrasonic waves that interact with different textile filaments are influenced by their linear density T and parameter $\cos\nu$. It should be noted that the parameter $\cos\nu$ depends on the material porosity, the frequency f of ultrasonic waves and their power.

To have a contactless control of the tension change of the thread branch, it is advisable to use a pulsed ultrasonic signal with two different peaks of wave amplitudes (see Fig. 3), which are adjusted to the linear density T of the thread and its conditional radius r. Measuring the thread tension with the help of two peaks of wave amplitudes will allow taking into account the part of the ultrasonic signal that passes through the interfiber pores and the part of the signal that bypasses the thread itself.

If a waveguide is used to determine the tension change of a particular branch of the thread using sounding of the material with an ultrasonic pulse signal with two different peaks of amplitude, then the expression for this parameter can be written as follows:

$$P^* = \frac{P}{2}\cdot\left(\left(\frac{r}{r*}\right)^3 + \left(\frac{\cos\nu_2}{\cos\nu_2^*}\right)^3\right),$$

$$P^* = \frac{Pr^3}{2}\cdot\left(\sqrt{\frac{T}{\frac{Z_1}{\pi f r n\cdot\cos\nu_1}\cdot\sqrt{\frac{1}{|W_1|^2}-1}}}\right)^{-3} +$$

$$+\frac{P}{2}\cdot\left(\frac{\pi^2 f r n\rho_2\cos\nu_2}{Z_1}\right)^3\cdot\left(\sqrt{\frac{1}{\left(|W_2|-\frac{P_{1w}}{K_V P_{01w}^*}\right)^2}-1}\right)^{-3}, \quad (3)$$

$$P^* = \frac{Pr^3}{2}\cdot\left(\sqrt{\frac{T}{\frac{Z_1}{\pi f r n\cdot\cos\nu_1}\cdot\sqrt{\left(\frac{U_1}{U_i}\right)^2-1}}}\right)^{-3} +$$

$$+\frac{P}{2}\cdot\left(\frac{\pi^2 f r n\rho_2\cos\nu_2}{Z_1}\right)^3\cdot\left(\sqrt{\frac{1}{\left(\frac{U_i^*}{U_1^*}-\frac{U_i}{K_V U_1^*}\right)^2}-1}\right)^{-3},$$

$$K_V = K_p^{\left(\frac{P_{01w}}{P_{1w}}\right)} = K_p^{\left(\frac{U_1}{U_i}\right)}, \quad (4)$$

$$\delta = \frac{P^*\left(\text{using ultrasonic method measurement}\right) - P^*\left(\text{using standard contact method measurement}\right)}{P^*\left(\text{using standard contact method measurement}\right)}\cdot 100\%, \quad (5)$$

where i – 2, 3, 4…, the number of the voltage amplitude value from the receiving transducer when changing the thread branch tension as for its previous state; U_1 – the voltage amplitude which is proportional to the

smaller peak of the pulsed ultrasonic signal when it propagates in the waveguide without a thread; U_i – the voltage amplitude which is proportional to the smaller peak of the pulsed ultrasonic signal when it propagates in a waveguide with a thread with a change in its tension, different values of which are associated with the sequence number i; U_1^* – the voltage amplitude which is proportional to the larger peak of the pulsed ultrasonic signal when it propagates in the waveguide without a thread; U_i^* – the voltage amplitude which is proportional to the larger peak of the pulsed ultrasonic signal, when it propagates in a waveguide with a thread with a change in its tension, the different values of which are associated with the sequence number i; $|W_1|$ – module of complex coefficient of ultrasonic waves transmission which is equal to the voltage ratio U_i / U_1; $|W_2|$ – module of complex coefficient of ultrasonic waves transmission which is equal to the voltage ratio U_i^* / U_1^*; ν_1 – the angle between the direction of the waves enveloping the thread fibers in its middle, and the surface of these fibers; ν_2 – the angle between the direction of the part of the waves that envelop the thread from its outer side, and the surface of the whole material; ν_2^* – the angle between the direction of the part of the waves that envelop the thread from its outer side, and the surface of the whole material when changing the fibers tension; r – conventional radius of the controlled thread in case of the absence of tension; n – the number of the ultrasonic wave passes of the cross section of the waveguide with the thread which is necessary for the oscillations to enter the receiving transducer; K_V – the ratio of the air volume between the thread fibers; K_p – initial coefficient of interfiber porosity of the thread material; T – linear thread density; P – initial thread tension; P^* – the current tension of the thread being determined; P_{01w} – the pressure amplitude in the wave of the smaller peak of the pulse signal that passes through the waveguide without a thread; P_{1w} – the pressure amplitude in the wave of the smaller peak of the pulse signal that passes through the waveguide with the thread when changing its tension; P_{01w}^* – the pressure amplitude in the wave of the larger peak of the pulse signal that passes through the waveguide without a thread.

By means of the received aspect (3), it is possible to define in practice a change of current thread tension with a big linear density on the technological equipment if necessary. It is also possible to further investigate the change in the interfiber porosity of different threads during their tension.

Some results obtained in theoretical and experimental studies are represented in Table 1.

Table 1

Experimental data of non-contact method

Parameter	Experimental data		
T	445 mg/m		
r	1.50 mm		
f	40 kHz		
$\cos \nu_2$	0.00335		
K_p	2.8		
P	19.6 cN		
n	3		
i	-	2	3
Determining P^* using contact method:	-	0	19.6 cN
r^*	-	1.50 mm	1.47 mm
$\cos \nu_2^*$	-	0.00335	0.00334

Voltage oscillograms	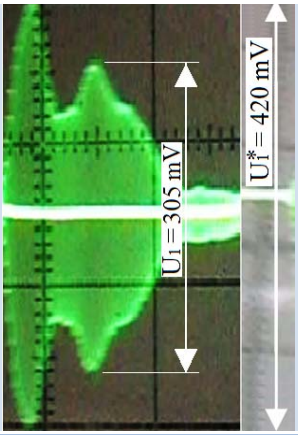	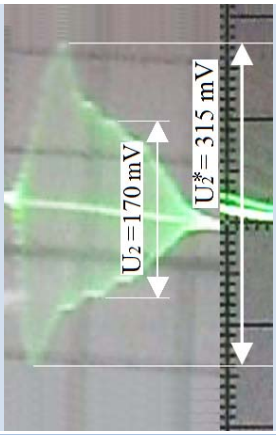	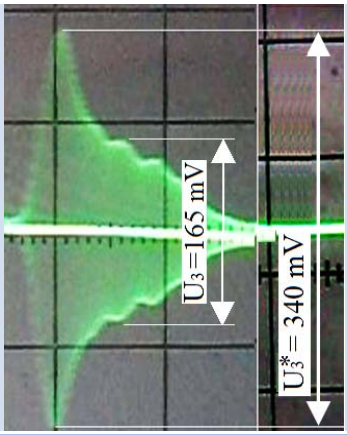
Voltage amplitude	U_1 = 305 mV U_1^* = 420 mV	U_2 = 170 mV U_2^* = 315 mV	U_3 = 165 mV U_3^* = 340 mV
$\lvert W_1 \rvert = \frac{U_i}{U_1}$	1	0.557	0.541
$\lvert W_2 \rvert = \frac{U_i^*}{U_1^*}$	1	0.750	0.810
Determining P^* using non-contact method:	-	0	20.364 cN
Variance δ	-	0	3.9 %
i	4	5	6
Determining P^* using contact method:	49.0 cN	68.6 cN	98.0 cN
r^*	1.02 mm	0.99 mm	0.95 mm
$\cos \nu_2^*$	0.00282	0.00222	0.00183
Voltage oscillograms	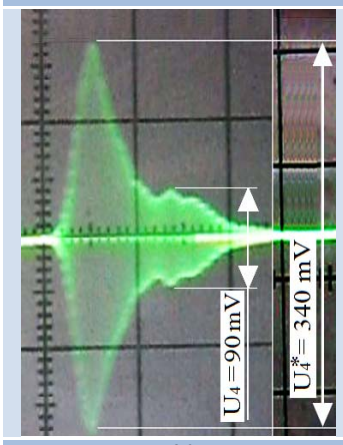	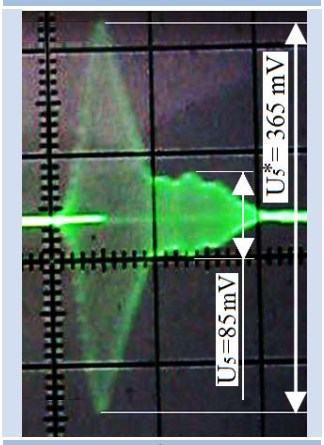	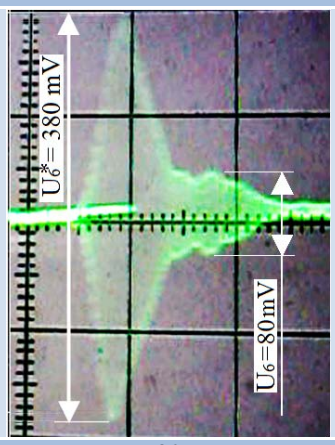
Voltage amplitude	U_4 = 90 mV U_4^* = 340 mV	U_5 = 85 mV U_5^* = 365 mV	U_6 = 80 mV U_6^* = 380 mV
$\lvert W_1 \rvert = \frac{U_i}{U_1}$	0.295	0.279	0.262
$\lvert W_2 \rvert = \frac{U_i^*}{U_1^*}$	0.810	0.869	0.905
Determining P^* using non-contact method:	47.904 cN	68.333 cN	98.544 cN
Variance δ	-2.2 %	-0.39 %	0.56 %

These results show that it is possible to create an accurate non-contact method for determining the thread tension with a high linear density.

The part of the ultrasound signal, which passes directly through the structure of the thread itself, can also be used to determine the change of interfibrous porosity of the threads. The effect of determining the change of interfibrous porosity in the thread tension process has also been considered in this article and has been experimentally recorded by using ultrasound impulse signals of a complex shape, as shown in Table 1. and Fig. 3.

Non-contact determination of the thread tension using a waveguide, with all oscillograms of pulsed ultrasonic signals are represented in Fig. 3. The correspondence of each oscillogram of pulse signals to the current value of the thread tension in the waveguide is noticed. It is clear that the first peak of the amplitude of the ultrasonic signal decreases, and the second peak of the amplitude increases. The combination of measuring information about the amplitude informative parameters of the two peaks of ultrasonic waves makes it possible to consider the part of the oscillations that bypasses the controlled material and to reduce the error of tension measurement.

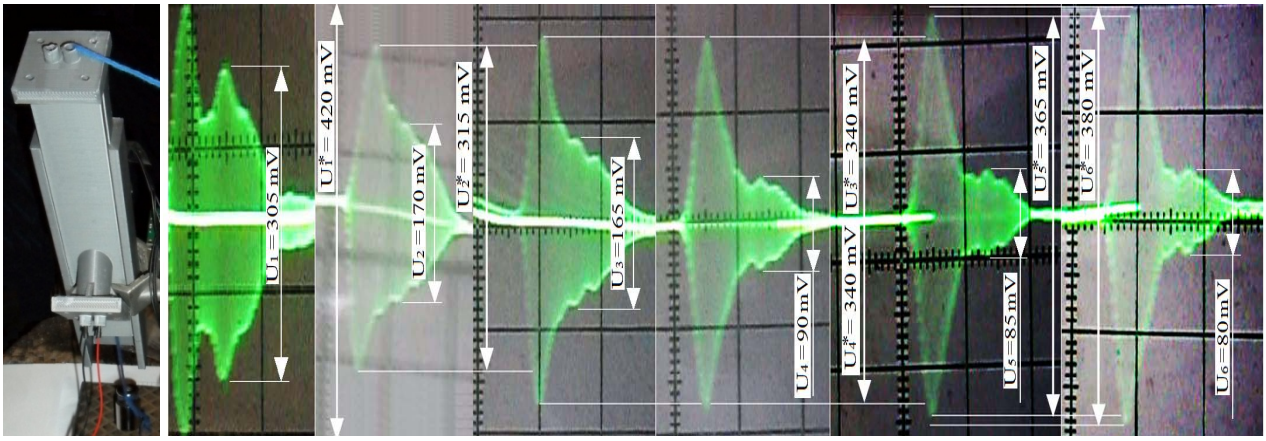

Figure 3. Non-contact determination of thread tension in a waveguide:

a – transmission of an impulse ultrasound signal through a thread in a waveguide without repetition;
b – appearance of an impulse ultrasound signal of a complex shape with two peaks of amplitudes which determine tension and change of interfibrous porosity of the thread after passing through and repetition of waves in a waveguide

The increase of the second peak amplitude of an ultrasound signal of a complex shape indicates increase in the magnitude of tension and decrease of a nominal diameter of the thread in accordance with the surfaces illustrated in Fig. 2, and the decrease of the first peak amplitude of an ultrasound signal shows decrease of interfibrous porosity of the thread with increasing its tension and deformation.

Figure 4 graphically demonstrates the theoretical dependencies and experimental data, which were also given in Table 1. From the obtained data parameters, one can see that in the area of the curve when the thread tension is in the range from 20 cN to 50 cN, its diameter and interfiber porosity decrease significantly. At the beginning of the thread tension process, when the interfiber porosity is significant, some of the waves pass through the pores between the fibers, so the higher peak of the amplitude is further increased. At a tension of 50 cN, the higher peak of the amplitude increases due to the part of the waves enveloping the thread with a reduced diameter from the outside of its surface. The other part of the oscillations, which initially further increased the amplitude of this peak, now passing through the reduced pores between the fibers of the material from the middle, reduces the resulting amplitude. Therefore, Figure 4 represents that the amplitude of this peak during the action of the thread tension in this range of its values (20 cN – 50 cN) remains the same.

Studies have shown that with the help of impulse ultrasound signals it is possible to determine not only the tension of threads with high linear density but also the degree of twist of complex threads by changing their interfibrous porosity, which, in turn, can be controlled by changing the amplitudes of ultrasonic waves.

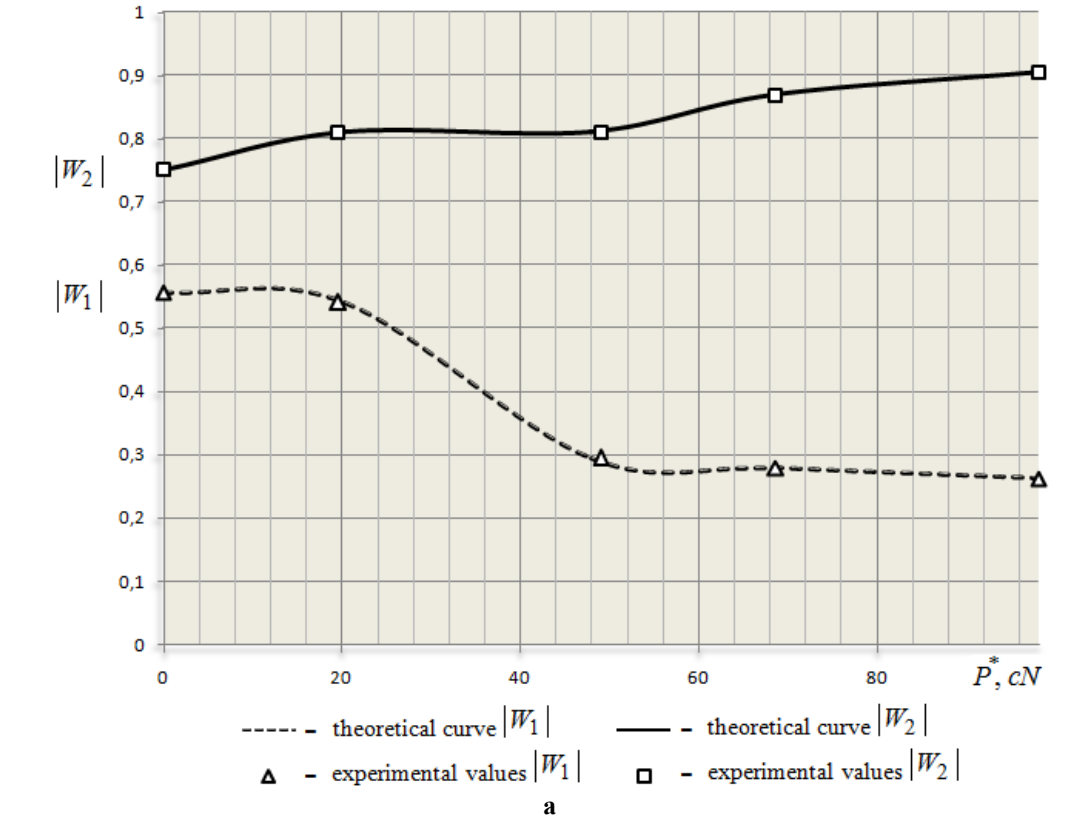

a

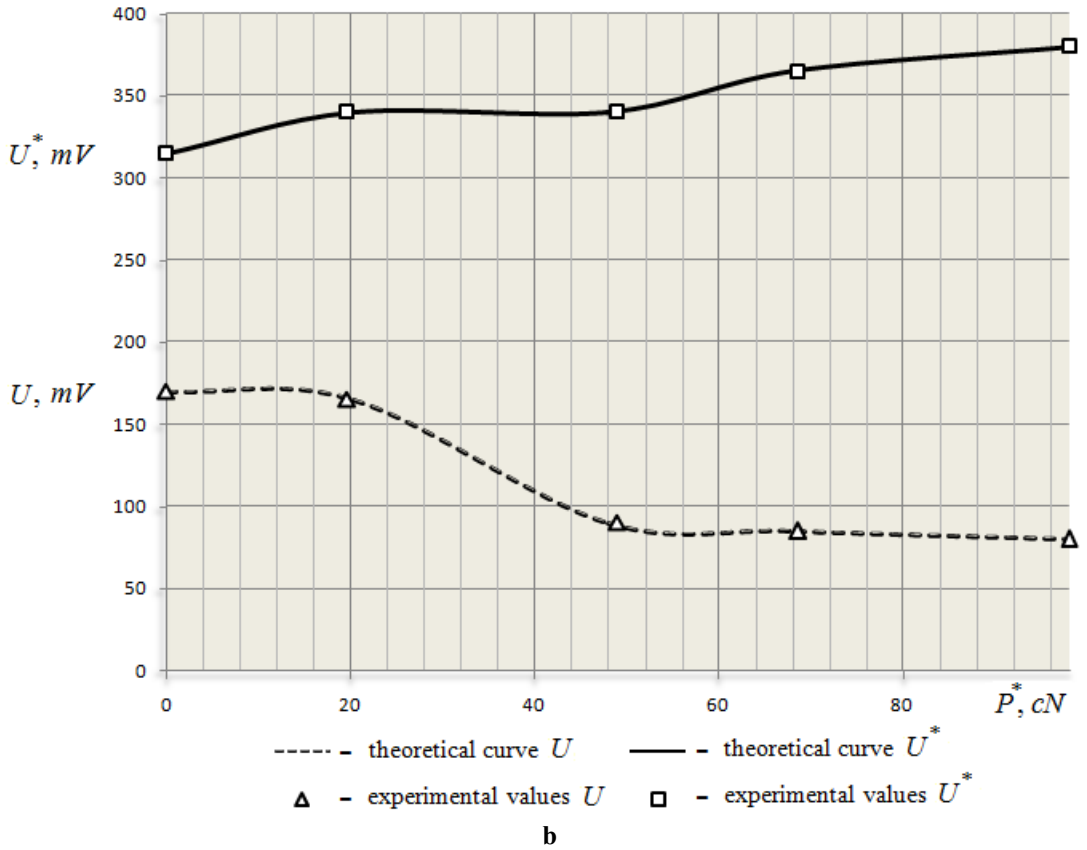

b

Figure 4. Dependencies of amplitude parameters on the thread tension in the waveguide: *a* – dependencies of amplitude parameters $|W_1|$, $|W_2|$ waves on the thread tension P^*; *b* – dependencies of the amplitude voltages parameters U_i, U_i^* on the thread tension P^*

The amplitude ratios of ultrasonic waves that interact with the thread material, make it possible to create contactless control systems of the thread tension for the production of textile fabrics.

Conclusions

In the course of the research, it was found out that impulse ultrasound signals can be used to determine the thread tension of different raw material composition. A pulsed ultrasonic signal of complex shape allowed to determine the tension of a filament with a high linear density in a special waveguide with a rectangular cross-section. To enable non-contact control of the change in the tension of the thread branch, the use of a pulsed ultrasonic signal with two different peaks of the wave amplitudes were adjusted to the linear density of the thread and its conditional radius. It was possible to see from the general comparison of pulse signals correspondence of each of their oscillogram to current value of a tension of a thread in a waveguide. During the non-contact determination of thread tension in a waveguide the first peak of the amplitude of the ultrasonic signal decreased, and the second peak of the amplitude increased. The combination of measuring information about the amplitude informative parameters of the two peaks of ultrasonic waves implemented to consider the part of the oscillations that bypasses the controlled material and to reduce the error of tension measurement. An increase in the amplitude of the second peak of the ultrasonic signal of complex shape showed an increase in tension and a decrease in the conditional diameter of the thread, and a decrease in the amplitude of the first peak of the ultrasonic signal demonstrated a decrease in interfiber porosity with increasing tension and deformation. From the obtained data on the amplitude parameters of ultrasonic waves, in the area of the curve graph, when the tension of the filament was in the range from 20 cN to 50 cN, its diameter and interfiber porosity significantly decreased. At the beginning of the thread tension process, when the interfiber porosity was significant, the part of the waves passed through the pores between the fibers, so the higher peak of the amplitude was further increased. At a tension of 50 cN, the higher peak of the amplitude increased due to the part of the waves enveloping the thread. The other part of the oscillations, which initially further increased the amplitude of this peak, then passed through the reduced pores between the fibers of the material from the middle, reduced its resulting amplitude. Therefore, the amplitude of this peak during the action of tension on the thread in this range of its values (20 cN – 50 cN) remained the same. Conducted research will facilitate to use non-contact ultrasound methods and means for the operating control of the thread tension in the process of production of various textile fabrics. In the future, it will improve the quality by maintaining within the regulated limits of basis weight of the fabrics with the required accuracy, as well as the competitiveness of domestic products in textile industry.

References

1 Vasconcelos FB. Influence of yarn tension variations before the positive feed on the characteristics of knitted fabrics / FB. Vasconcelos, JPP. Marcicano, RA. Sanches // Textile Research Journal. — 2015. — Vol. 85 (17). — P. 1864–1871.

2 Koranne M. Fundamentals of yarn winding / M. Koranne. — New Delhi: Woodhead Publishing India Pvt Limited, 2013. — P. 190.

3 Hu Xintong. Tension modeling and analysis of braiding carriers during radial-direction and axial-direction braiding / Xintong Hu, Yujing Zhang, Zhuo Meng, Yize Sun // The Journal of The Textile Institute. — 2019. — P. 1–12.

4 Tong Yun. Intelligent Control of the Dynamic Tension of Yarn by Means of Sensors in Winding Process / Yun Tong // Applied Mechanics and Materials. — 2014. — P. 2305–2308.

5 Щербань В.Ю. Механика нити / В.Ю. Щербань, О.Н. Хомяк, Ю.Ю. Щербань. — Киев: КНУТД, 2002. — 196 с.

6 Zdorenko V. The use of ultrasonic method for determining the basis weight of textile materials / V. Zdorenko, O. Kyzymchuk, S. Barylko, L. Melnyk // The Journal of The Textile Institute. — 2018. — Vol. 109. — Issue 3. — P. 410–418.

7 Barylko S. Adaptive ultrasonic method for controlling the basis weight of knitted fabrics / S. Barylko, V. Zdorenko, O. Kyzymchuk, S. Lisovets, L. Melnyk, Olena Barylko // Journal of Engineered Fibers and Fabrics. — 2019. — Vol. 14. — P.1–7.

8 Ambroziak A. Example of Tension Fabric Structure Analysis / A. Ambroziak, P. Klosowski, O. Kyzymchuk, et al. // TASK QUARTERLY. — 2019. — 14 № 1–2. — P. 5–14.

9 Shaeffer R.E. Tensioned Fabric Structures: A Practical Introduction / R.E. Shaeffer. — New York: American Society of Civil Engineers Press, 1996. — P. 80.

10 Postle R., Pan N. Experimental Methods for Measuring Fabric Mechanical Properties: A Review and Analysis / R. Postle, N. Pan // Textile Research Journal. — 1999. — Vol. 69. — P. 866–875.

11 Gloy Y.-S., Gries T., Spies G. Non destructive testing of fabric weight in the weaving process // 13th International Symposium on Nondestructive Characterization (NDCM-XIII), 20–24 May 2013, Le Mans, France. Режим доступа: https://www.ndt.net/article/ndcm2013/content/papers/46_Gloy_Rev1.pdf

12 Lyons D. Acoustic measurement of fiber properties / D. Lyons, J. Graham // Textile Research Journal. — 1975. — No. 7. — P. 549–553.

В.Г. Здоренко, В.Ю. Кучерук, С.В. Барылко, С.Н. Лисовец

Жеңіл өнеркәсіп машиналары үшін жіптің керілуін анықтайтын байланыссыз ультрадыбыстық әдіс

Күрделі пішінді импульсті ультрадыбыстық дабылды қолдана отырып, тікбұрышты қимасы бар арнайы толқын өткізгіште жоғары сызықтық тығыздығы бар жіптің керілуін анықтауға болатындығы анықталды. Әртүрлі тоқыма жіптерімен өзара әрекеттесетін ультрадыбыстық толқындардың амплитудалық қатынасына олардың сызықтық тығыздығы, жіп талшықтарын оның ортасында айналдыратын толқындардың бір бөлігінің өту бағыты мен осы талшықтардың беті арасындағы бұрыш, сондай-ақ жіптің сыртқы жағынан айналатын толқындардың бір бөлігінің таралу бағыты мен бүкіл материалдың беті арасындағы бұрыштың әсер ететіндігі дәлелденді. Тоқыма бұйымдарына ультрадыбыстық толқындарының сәйкес өту бұрыштары материалдың кеуектілігіне, ультрадыбыстық толқындардың жиілігіне және олардың қуатына байланысты екенін атап өткен жөн. Ультрадыбыстық толқындардың амплитудалық қатынасының жіптің керілуіне алынған тәуелділіктерінің графигі және оларды тәжірибелік мәліметтермен салыстыру берілген. Жіп тармағының керілуінің өзгеруін байланыссыз басқару мүмкіндігі үшін жіптің сызықтық тығыздығына және оның шартты радиусына сәйкес келетін екі түрлі толқындық амплитудасы бар импульсті ультрадыбыстық дабылды қолданған жөн. Сонымен қатар, әдісті қолдану тоқыма маталарды өндіру кезінде жедел технологиялық бақылауды қамтамасыз ететіні көрсетілді. Аталған байланыссыз ультрадыбыстық әдіс тоқу машиналарында жіптердің керілуін реттеу жүйесін жетілдіруге, сондай-ақ өндіріс кезінде олардың үзілгенін анықтауға көмектеседі. Бұл өз кезегінде технологиялық жабдықтардың тоқтап қалуын қысқартады, дайын өнімнің сапасын жақсартады және оның нарықтағы бәсекегеқабілеттілігін қамтамасыз етеді.

Кілт сөздер: жіптің тартылуы, амплитудалық коэффициенттер, ультрадыбыстық толқындар, толқын өткізгіш, жіптің сызықтық тығыздығы, бетінің тығыздығы, тоқыма маталар.

В.Г. Здоренко, В.Ю. Кучерук, С.В. Барылко, С.Н. Лисовец

Бесконтактный ультразвуковой метод определения натяжения ниток для машин легкой промышленности

Установлено, что с помощью импульсного ультразвукового сигнала сложной формы можно определять натяжение нити с большой линейной плотностью в специальном волноводе с прямоугольным сечением. Доказано, что на амплитудные соотношения ультразвуковых волн, которые взаимодействуют с различными текстильными нитями, влияют их линейная плотность, угол между направлением прохождения части волн, огибающих волокна нити в ее середине, и поверхностью этих волокон, а также угол между направлением распространения части волн, огибающих нить с внешней ее стороны, и поверхностью всего материала. Следует отметить, что соответствующие углы обхода ультразвуковых волн текстиля зависят от пористости материала, частоты ультразвуковых волн и их мощности. Приведены графики полученных зависимостей амплитудных соотношений ультразвуковых волн от натяжения нити и их сравнение с экспериментальными данными. Для возможности бесконтактного контроля изменения натяжения ветви нити целесообразно применять импульсный ультразвуковой сигнал с двумя различными пиками амплитуд волн, которые настраиваются под линейную плотность нити и ее условный радиус. Показано, что использование этого метода позволит обеспечить оперативный технологический контроль в процессе производства текстильных полотен. Данный бесконтактный ультразвуковой метод поможет улучшить систему регулирования натяжения нитей на трикотажных машинах, а также определять их обрывность в процессе производства. Это, в свою очередь, уменьшит простой технологического оборудования, повысит качество готовой продукции и обеспечит ее конкурентоспособность на рынке.

Ключевые слова: натяжение нити, амплитудные соотношения, ультразвуковые волны, волновод, линейная плотность нити, поверхностная плотность, текстильные полотна.

References

1 Vasconcelos, F.B., Marcicano, JPP. & Sanches, RA. (2015). Influence of yarn tension variations before the positive feed on the characteristics of knitted fabrics, *Textile Research Journal,* 85, 1864–1871.

2 Koranne, M. (2013). *Fundamentals of yarn winding*. New Delhi: Woodhead Publishing India Pvt Limited.

3 Hu Xintong, Zhang Yujing, Meng Zhuo, & Sun Yize (2019). Tension modeling and analysis of braiding carriers during radial-direction and axial-direction braiding, *The Journal of The Textile Institute*, 1–12.

4 Tong Yun (2014). Intelligent Control of the Dynamic Tension of Yarn by Means of Sensors in Winding Process*, Applied Mechanics and Materials,* 2305–2308.

5 Shcherban, V.Yu., Khomiak, O.N. & Shcherban, Yu.Yu. (2002). Mekhanika niti [*Mechanics of thread]*. Kyiv: KNUTD [in Russian].

6 Zdorenko, V., Kyzymchuk, O., Barylko, S., & et al. (2018). The use of ultrasonic method for determining the basis weight of textile materials, *The Journal of The Textile Institute*, 109, 410–418.

7 Barylko, S., Zdorenko, V., Kyzymchuk, O., & et al. (2019). Adaptive ultrasonic method for controlling the basis weight of knitted fabrics, *Journal of Engineered Fibers and Fabrics*, 14, 1–7.

8 Ambroziak, A., Klosowski, P., Kyzymchuk, O., & et al. (2019). Example of Tension Fabric Structure Analysis, *TASK QUARTERLY*, 14 No 1–2, 5–14.

9 Shaeffer, R.E. (1996). *Tensioned Fabric Structures: A Practical Introduction,* American Society of Civil Engineers Press, New York.

10 Postle, R. & Pan, N. (1999). Experimental Methods for Measuring Fabric Mechanical Properties: A Review and Analysis, *Textile Research Journal*, 69, 866–875.

11 Gloy, Y.S., Gries, T. & Spies, G. (2013). Nondestructive testing of fabric weight in the weaving process. 13th International Symposium on Nondestructive Characterization. (NDCM-XIII), May 20–24, Le Mans, France. Retrieved from: https://www.ndt.net/article/ndcm2013/content/papers/46_Gloy_Rev1.pdf

12 Lyons, D. & Graham, J. (1975). Acoustic measurement of fiber properties, *Textile Research Journal*, 7, 549–553.

DOI 10.31489/2021PH4/46-51

UDC 539.893

A.U. Abuova[1], T.M. Inerbaev[1,2], F.U. Abuova[1*], G.A. Kaptagay[3]

[1]L.N. Gumilyov Eurasian National University, Nur-Sultan, Kazakhstan;
[2]South China Normal University, Guangzhou, China;
[3]Kazakh National Women's Teacher Training University, Almaty, Kazakhstan
(E-mail: Fatika_82@mail.ru)

Theoretical study of the Ni–C system in the pressure range of 0–100 GPa

This work is devoted to the search for stable compounds and structures in the Ni–C system in the pressure range of 0–100 GPa. Based on the density functional theory, a search for stable compounds and structures in the Ni–C system was carried out using modern algorithms for predicting crystal structures. As a result, one stable intermediate compound Ni_3C with the structure of cementite, previously synthesized at 184 GPa, was revealed. Ni_3C nickel carbide is dynamically stable, which is confirmed by the absence of imaginary modes in the phonon spectra. According to the results obtained, Ni_3C is formed by the reaction of $3Ni + C \leftrightarrow Ni_3C$ above 23 GPa and is stable up to at least 100 GPa. Spin-polarized calculations showed that the Ni_3C has no magnetic moment in the entire pressure range. For carbon-rich compounds, performed calculations on the crystal structure prediction did not reveal any phase that would be energetically favorable relative to a mixture of pure nickel and carbon. Also, it was shown that the most energetically favorable modification of metastable carbide Ni_7C_3 is orthorhombic Ni_7C_3-*Pbca*.

Keywords: density functional theory, crystal structure prediction, USPEX, AIRSS, high pressure, phase stability, phonon spectra, nickel carbide.

Introduction

The Ni–C system at high pressure is of interest both from the point of view of Earth sciences and materials science. Nickel carbides are of active interest as catalysts in the chemical deposition of a gas mixture (CVD) to produce high-quality graphene [1]. In addition, nanoparticles of metal carbides, particularly nickel, in the carbon matrix make up nanocomposite thin films, which have a wide profile of application in metallurgy [2]. On the other hand, nickel is the second most common element in the Earth's core after iron [3]. According to cosmochemical data, the core contains 5 wt.% Ni [4]. However, seismic observations show that the core density is significantly lower than that of pure Fe and Fe–Ni alloy under P-T core conditions [5], which suggests the presence of a light element in the core. The question "what exactly are these elements, and what is their number?" remains the subject of active discussions today. Recent estimates of the composition of the inner core indicate a carbon content of up to 2.0 wt.% [4], which makes it a potential candidate for the role of a light element in the Earth's core. Therefore, to study the composition and structure of the Earth's core, it is important to investigate the Fe–Ni–C system at high pressures. To study the ternary Fe-Ni-C system, first, the binary Fe-C and Ni–C systems should be investigated. In the last decade, the Fe–C system has been actively studied at high pressure both theoretically and experimentally [6–9]. To date, there is only one experimental work [10] on the Ni–C system at high pressure and there is no theoretical study on this system. Thus, it is considerable to carry out theoretical study on the Ni–C system.

There are no stable binary Ni–C compounds at atmospheric pressure. In a recent work [10], it was shown that at high pressure (~184 GPa), a stable compound of Ni_3C with the structure of cementite (Fe_3C) is formed. To date, this is the only known stable compound in the Ni–C system.

This work is devoted to the search for stable compounds and structures in the Ni-C system in the pressure range of 0–100 GPa.

Experimental

Calculations implemented by authors on licensed USPEX and AIRSS software allow calculating the electronic structure of periodic systems with the use of the density functional theory.

The search for stable crystal structures in the Ni–C system was carried out using evolutionary algorithms and the random sampling method implemented in the USPEX and AIRSS software packages at pressures of 0, 25, 50, and 100 GPa. The search was conducted using the variable composition method and the USPEX code, while the structures were generated by the AIRSS code for fixed compositions, namely the carbon-enriched part of the Ni–C system.

The number of structures of the initial generation in the calculations by the USPEX method was equal to 50. After their optimization, 60% of the structures with the lowest enthalpy were selected, which were used to generate a new generation in the following percentage ratio: by heredity – 35%, by atomic mutations – 20%, by permutation of lattice parameters – 10% and 35% of all structures of the new generation were generated randomly. In the case of calculations of AIRSS methods, 2000–3200 structures were randomly generated and optimized, from which the most energetically favorable structures were selected. In all calculations, optimization was performed within the framework of density functional theory (DFT), using the conjugate gradient algorithm. The optimization parameters were as follows: the cutting energy of the plane wave basis was 450 eV, the Monkhorst-Pack k-point grid [11] with a point density equal to 0.5 Å-1, the electronic blur was according to the Methfessel-Paxton scheme [12], the parameter σ = 0.05 eV. Calculations of the ground state energies of the most promising of the predicted structures were conducted within the framework of the density functional theory (DFT) by the pseudo potentials method, in the VASP 5.3 software package [13, 14] with higher accuracy: the cut-off energy is 600 eV, the density of k–points is 0.2 $Å^{-1}$, the parameter σ = 0.1 eV. The exchange-correlation interaction was taken into account in the approximation of the generalized gradient according to the Purdue-Burke-Ernzerhof (PBE) scheme [15].

To calculate the phonon spectra, the lattice dynamics method was used in the framework of the quasi-harmonic approximation in the PHONOPY software package [16].

Results and Discussion

Using modern methods of structure prediction, the only energetically advantageous compound Ni_3C was found, as well as a number of metastable structures NiC, NiC_2, and NiC_3 (Fig. 1). Ni_3C stabilizes in the cementite structure (Pnma) above 23 GPa relative to the reaction 3Ni + C ↔ Ni_3C (Figure 2a). The most favorable among the predicted structures of the remaining compounds turned out to be energetically unfavorable relative to a mixture of pure nickel and carbon in the entire studied pressure range (0–100 GPa), with ΔH reaching values of 0.4 eV/f.u. for NiC, NiC_2, and NiC_3 (Figure 1). In the Fe–C system, in addition to Fe_3C, Fe_7C_3 is also thermodynamically stable. Fe_7C_3 iron carbide has two stable modifications: Fe_7C_3–Pbca and Fe_7C_3–P63mc. Similarly, Ni_7C_3 nickel carbide was also considered in the form of two modifications. The structural models Ni_7C_3–Pbca and Ni_7C_3–P63mc were constructed by replacing all iron atoms with nickel atoms in the structures Fe_7C_3–Pbca and Fe_7C_3–P63mc [17]. The calculation of the ground state energy of the obtained structures showed that Ni_7C_3–Pbca is an energetically more favorable structure than Ni_7C_3–P63mc by ~0.42 eV/f. u., however, it is energetically less favorable relative to the mechanical mixture of 7/3Ni_3C + 2/3C in the entire pressure range considered (Fig. 2b).

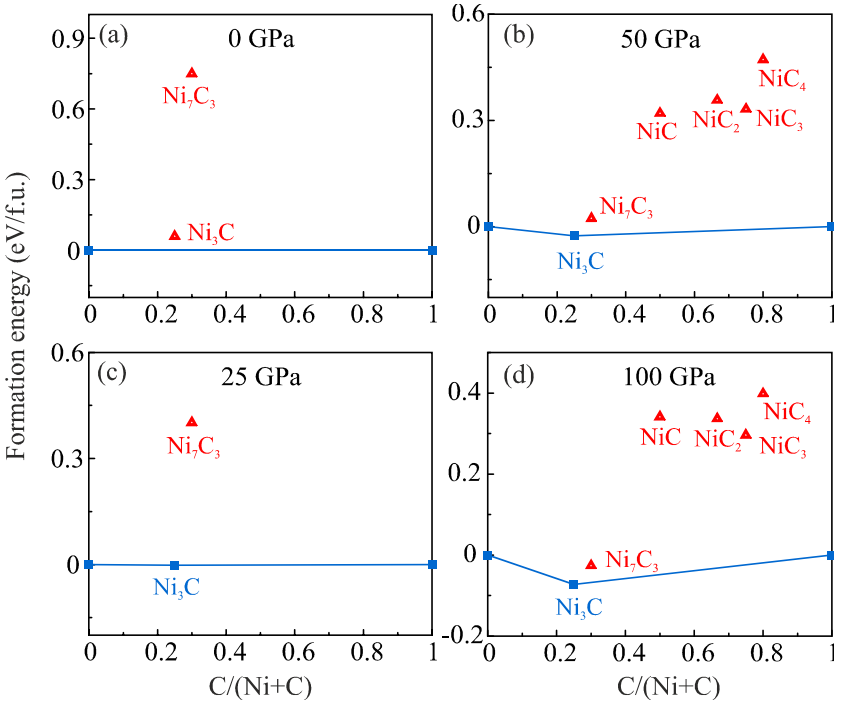

Figure 1. Thermodynamic convex hulls at various pressures and temperatures of 0 K

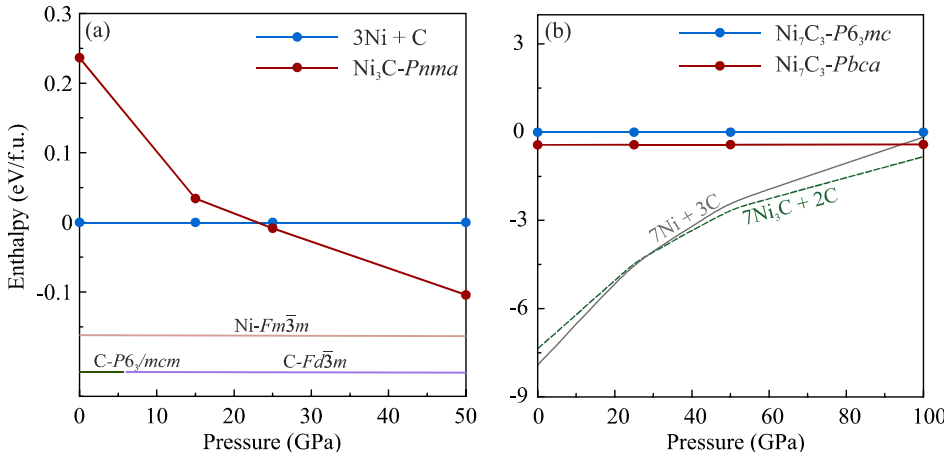

Figure 2. The dependence of the enthalpy on the pressure of Ni_3C–*Pnma* with respect to the decomposition reaction to the association of 3Ni + C (a) and the dependence of the enthalpy on the pressure for modifications of Ni_7C_3 with the application of possible decomposition reactions (b)

Spin-polarized calculations showed the absence of a magnetic moment in the entire studied pressure range. According to the calculations of the phonon dispersion curves, Ni_3C at 25 GPa is characterized by the presence of only real modes, which indicates the dynamic stability of this phase (Fig. 3).

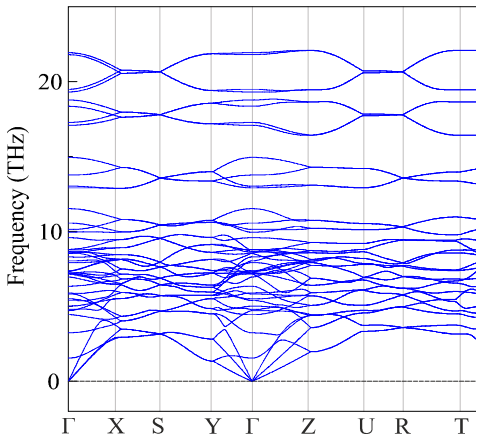

Figure 3. Ni_3C-*Pnma* phonon spectrum at 25 GPa

Also, for comparison with the experimental data [10], the equation of state in the range of 0–200 GPa was calculated. It can be seen from Figure 4 and Table 1 that our results are in good agreement with the experiment.

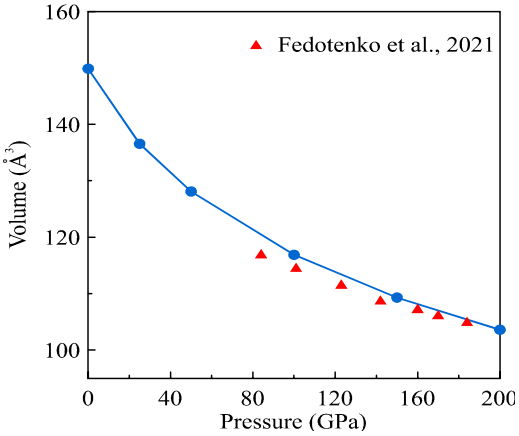

Figure 4. Pressure-volume dependence for Ni_3C–*Pnma*

Table 1

Calculated parameters V_0 and K_0 in comparison with experimental data [10]

	V_0 (Å^3)	K_0 (ГПа)
Experiment	147,7(8)	157(10)
This work	149,88	168

Conclusions

Within the scope of this study, a search for stable structures in the Ni–C system was carried out. It was shown that the Ni–C system in the pressure range of 0–100 GPa is characterized by one intermediate compound NiC. This nickel carbide is stabilized relative to the mechanical mixture of Ni and C above 23 GPa. The dynamic stability of Ni_3C is confirmed by the absence of imaginary frequencies in the phonon spectrum. Also, for comparison with experimental data, the Ni_3C equation of state was calculated in the pressure range of 0–200 GPa. The obtained result is in good agreement with the experiment.

Acknowledgments

This work was carried out within the framework of the grant project AP09562464 “Search for functional (superhard) materials in Ni–B, Ni–C and Ni–N systems” for 2021 of the Ministry of Education and Science of the Republic of Kazakhstan.

References

1 Hofmann S. CVD-enabled graphene manufacture and technology / S. Hofmann, P. Braeuninger-Weimer, R.S. Weatherup // The journal of physical chemistry letters. — 2015. — Vol. 6, No. 14. — P. 2714–2721. DOI: 10.1021/acs.jpclett.5b01052

2 Bayer B.C. In situ observations of phase transitions in metastable nickel (carbide)/carbon nanocomposites / B.C. Bayer, D.A. Bosworth, F.B. Michaelis, R. Blume, G. Habler, R. Abart, R.S. Weatherup, P.R. Kidambi, J.J. Baumberg, A. Knop-Gericke // The Journal of Physical Chemistry C. — 2016. — Vol. 120, No. 39. — P. 22571–22584. DOI: 10.1021/acs.jpcc.6b01555

3 Birch F. Elasticity and constitution of the Earth's interior / F. Birch // Journal of Geophysical Research. — 1952. — Vol. 57, No. 6. — P. 227–286. DOI: 10.1029/JZ057i002p00227

4 Litasov K.D. Composition of the Earth’s core: A review / K.D. Litasov, A. Shatskiy // Russian Geology and Geophysics. — 2016. — Vol. 57, No. 1. — P. 22–46. DOI: 10.15372/GiG20160103

5 Stevenson D.J. Models of the Earth's Core / D.J. Stevenson // Science. — 1981. — Vol. 214 (4521). — P. 611–619. DOI: 10.1126/science.214.4521.611

6 Bazhanova Z.G. Fe–C and Fe–H systems at pressures of the Earth's inner core / Z.G. Bazhanova, A.R. Oganov, O. Gianola // Physics-Uspekhi. — 2012. — Vol. 55, No. 5. — P. 489–497. DOI: 10.3367/UFNe.0182.201205 c.0521

7 Litasov K.D. Thermal expansion of iron carbides, Fe_7C_3 and Fe_3C, at 297–911 K determined by in situ X-ray diffraction / K.D. Litasov, S.V. Rashchenko, A.N. Shmakov, Y.N. Palyanov, A.G. Sokol // Journal of Alloys and Compounds. — 2015. — Vol. 628. — P. 102–106. DOI: 10.1016/j.jallcom.2014.12.138

8 Prescher C. High Poisson's ratio of Earth's inner core explained by carbon alloying / C. Prescher, L. Dubrovinsky, E. Bykova, I. Kupenko, K. Glazyrin, A. Kantor, C. McCammon, M. Mookherjee, Y. Nakajima, N. Miyajima // Nature Geoscience. — 2015. — Vol. 8, No. 3. — P. 220. DOI: 10.1038/ngeo2370

9 Weerasinghe G.L. Computational searches for iron carbide in the Earth's inner core / G.L. Weerasinghe, R. Needs, C.J. Pickard // Physical Review B. — 2011. — Vol. 84, No. 17. — P. 174110. DOI: 10.1103/PhysRevB.84.174110

10 Fedotenko T. Synthesis and Compressibility of Novel Nickel Carbide at Pressures of Earth’s Outer Core / T. Fedotenko, S. Khandarkhaeva, L. Dubrovinsky, K. Glazyrin, P. Sedmak, N. Dubrovinskaia // Minerals. — 2012. — Vol. 11, No. 5. — P. 516. DOI: 10.3390/min11050516

11 Monkhorst H.J. Special points for Brillouin-zone integrations / H.J. Monkhorst, J.D. Pack // Physical review B. — 1976. — Vol. 13, No. 12. — P. 5188. DOI: 10.1103/PhysRevB.13.5188

12 Methfessel M. High-precision sampling for Brillouin-zone integration in metals / M. Methfessel, A. Paxton // Physical Review B. — 1989. — Vol. 40, No. 6. — P. 3616. DOI: 10.1103/physrevb.40.3616

13 Kresse G. Efficiency of ab-initio total energy calculations for metals and semiconductors using a plane-wave basis set / G. Kresse, J. Furthmüller // Computational Materials Science. — 1996. — Vol. 6 (1). — P. 15–50. DOI: 10.1016/0927–0256(96)00008–0

14 Kresse G. From ultrasoft pseudopotentials to the projector augmented-wave method / G. Kresse, D. Joubert // Physical Review B. — 1999. — Vol. 59, No. 3. — P. 1758. DOI: 10.1103/PhysRevB.59.1758

15 Perdew J.P. Generalized gradient approximation made simple / J.P. Perdew, K. Burke, M. Ernzerhof // Physical review letters. — 2015. — Vol. 77, No. 18. — P. 3865. DOI: 10.1103/PhysRevLett.77.3865

16 Togo A. First principles phonon calculations in materials science / A. Togo, I. Tanaka // Scripta Materialia. — 2015. — Vol. 108. — P. 1–5. DOI: 10.1016/j.scriptamat.2015.07.021

17 Sagatov N. New high-pressure phases of Fe_7N_3 and Fe_7C_3 stable at Earth's core conditions: evidences for carbon–nitrogen isomorphism in Fe-compounds / N. Sagatov, P.N. Gavryushkin, T.M. Inerbaev, K.D. Litasov // RSC Advances. — 2019. — Vol. 9, No. 7. — P. 3577–3581. DOI: 10.1039/C8RA09942A

А.У. Абуова, Т.М. Инербаев, Ф.У. Абуова, Г.А. Каптагай

0–100 ГПа қысым диапазонындағы Ni–C жүйесін теориялық зерттеу

Мақала 0–100 ГПа қысым диапазонында Ni–C жүйесіндегі тұрақты қосылыстар мен құрылымдарды іздеуге арналған. Тығыздықтың функционалды теориясының негізінде Ni–C жүйесінде кристалдық құрылымдарды болжаудың заманауи алгоритмдерін пайдалана отырып, тұрақты қосылыстар мен құрылымдар іздестірілді. Нәтижесінде бұрын 184 ГПа синтезделген цементит құрылымымен бір тұрақты Ni_3C аралық байланыс табылды. Ni_3C никель карбиді динамикалық тұрақты, бұл фонондық спектрлерде қиялдық модасының болмауымен расталады. Алынған нәтижелерге сәйкес, Ni_3C $3Ni + C \leftrightarrow Ni_3C$ 23 ГПа-дан жоғары реакция нәтижесінде пайда болады және кем дегенде 100 ГПа-ға дейін тұрақты болады. Айналдыру поляризациясымен есептеулер Ni_3C-де қысымның барлық диапазонында магниттік момент жоқ екенін көрсетті. Көміртекке бай қосылыстар үшін кристалдық құрылымды болжау бойынша есептеулер таза никель мен көміртегі қоспасымен салыстырғанда энергетикалық жағынан қолайлы болатын бірде-бір фазаны анықтаған жоқ. Сондай-ақ, Ni_7C_3 метастабильді карбидтің ең энергетикалық тиімді модификациясы орторомбиялық Ni_7C_3-Pbca екендігі көрсетілген.

Кілт сөздер: тығыздықтың функционалды теориясы, кристалды құрылымды болжау, USPEX, AIRSS, жоғары қысым, фазалық тұрақтылық, фонондық спектрлер, никель карбиді.

А.У. Абуова, Т.М. Инербаев, Ф.У. Абуова, Г.А. Каптагай

Теоретическое исследование системы Ni–C в диапазоне давлений 0–100 ГПа

Статья посвящена поиску стабильных соединений и структур в системе Ni–C в диапазоне давлений 0–100 ГПа. На основе теории функционала плотности был проведен поиск стабильных соединений и структур в системе Ni–C с использованием современных алгоритмов прогнозирования кристаллических структур. В результате было обнаружено одно стабильное промежуточное соединение Ni_3C со структурой цементита, ранее синтезированное при 184 ГПа. Карбид никеля Ni_3C динамически стабилен, что подтверждается отсутствием воображаемых мод в фононных спектрах. Согласно полученным данным, Ni_3C образуется в результате реакции $3Ni + C \leftrightarrow Ni_3C$ выше 23 ГПа и стабилен по меньшей мере до 100 ГПа. Расчеты со спиновой поляризацией показали, что Ni_3C не имеет магнитного момента во всем диапазоне давлений. Для соединений, богатых углеродом, проведенные расчеты по прогнозированию кристаллической структуры не выявили ни одной фазы, которая была бы энергетически благоприятной по сравнению со смесью чистого никеля и углерода. Также было показано, что наиболее энергетически выгодной модификацией метастабильного карбида Ni_7C_3 является орторомбический Ni_7C_3-Pbca.

Ключевые слова: теория функционала плотности, предсказание кристаллической структуры, USPEX, AIRSS, высокое давление, фазовая стабильность, фононные спектры, карбид никеля.

References

1 Hofmann, S., Braeuninger-Weimer, P. & Weatherup, R.S. (2015). CVD-enabled graphene manufacture and technology. *The journal of physical chemistry letters, 6, No. 14,* 2714–2721. DOI: 10.1021/acs.jpclett.5b01052

2 Bayer, B.C., Bosworth, D.A., Michaelis, F.B., Blume, R., Habler, G., Abart, R., & et al. (2016). In situ observations of phase transitions in metastable nickel (carbide)/carbon nanocomposites. *The Journal of Physical Chemistry C, 120, No. 39,* 22571–22584. DOI: 10.1021/acs.jpcc.6b01555

3 Birch, F. (1952). Elasticity and constitution of the Earth's interior. *Journal of Geophysical Research, 57, No. 6,* 227–286. DOI: 10.1029/JZ057i002p00227

4 Litasov, K.D. & Shatskiy, A. (2016). Composition of the Earth’s core: A review. *Russian Geology and Geophysics, 57, No. 1,* 22–46. DOI: 10.15372/GiG20160103

5 Stevenson, D.J. (1981). Models of the Earth's Core. *Science, 214 (4521),* 611–619. DOI: 10.1126/science.214.4521.611

6 Bazhanova, Z.G., Oganov, A.R. & Gianola, O. (2012). Fe–C and Fe–H systems at pressures of the Earth's inner core. *Physics-Uspekhi, 55, No. 5,* 489–497. DOI: 10.3367/UFNe.0182.201205 c.0521

7 Litasov, K.D., Rashchenko, S.V., Shmakov, A.N., Palyanov, Y.N., & Sokol, A.G. (2015). Thermal expansion of iron carbides, Fe_7C_3 and Fe_3C, at 297–911 K determined by in situ X-ray diffraction. *Journal of Alloys and Compounds, 628,* 102–106. DOI: 10.1016/j.jallcom.2014.12.138

8 Prescher, C., Dubrovinsky, L., Bykova, E., Kupenko, I., Glazyrin, K., Kantor, A., & et al. (2015). High Poisson's ratio of Earth's inner core explained by carbon alloying. *Nature Geoscience, 8, No. 3,* DOI: 10.1038/ngeo2370

9 Weerasinghe, G.L., Needs, R. & Pickard, C.J. (2011). Computational searches for iron carbide in the Earth's inner core. *Physical Review B, 84, No. 17,* 174110. DOI: 10.1103/PhysRevB.84.174110

10 Fedotenko, T., Khandarkhaeva, S., Dubrovinsky, L., Glazyrin, K., Sedmak, P., & Dubrovinskaia, N. (2012). Synthesis and Compressibility of Novel Nickel Carbide at Pressures of Earth's Outer Core. *Minerals, 11, No. 5,* 516. DOI: 10.3390/min11050516

11 Monkhorst, H.J. & Pack, J.D. (1976). Special points for Brillouin-zone integrations, *Physical review B, 13, No. 12,* 5188. DOI: 10.1103/PhysRevB.13.5188

12 Methfessel, M. & Paxton, A. (1989). High-precision sampling for Brillouin-zone integration in metals. *Physical Review B, 40, No. 6,* 3616. DOI: 10.1103/physrevb.40.3616

13 Kresse, G., Joubert, D. & Furthmüller, J. (1996). Efficiency of ab-initio total energy calculations for metals and semiconductors using a plane-wave basis set. *Computational Materials Science, 6(1),* 15–50. DOI: 10.1016/0927-0256(96)00008-0

14 Kresse, G. (1999). From ultrasoft pseudopotentials to the projector augmented-wave method. *Physical Review B, 59, No. 3,* 1758. DOI: 10.1103/PhysRevB.59.1758

15 Perdew, J.P., Burke, K. & Ernzerhof, M. (2015). Generalized gradient approximation made. *Physical review letters, 77, No. 18,* 3865. DOI: 10.1103/PhysRevLett.77.3865

16 Togo, A. & Tanaka, I. (2015). First principles phonon calculations in materials science. *Scripta Materialia, 108,* 1–5. DOI: 10.1016/j.scriptamat.2015.07.021

17 Sagatov, N., Gavryushkin P.N., Inerbaev T.M., & Litasov, K.D. (2019). New high-pressure phases of Fe_7N_3 and Fe_7C_3 stable at Earth's core conditions: evidences for carbon–nitrogen isomorphism in Fe-compounds. *RSC Advances, 9. No. 7,* 3577–3581. DOI: 10.1039/C8RA09942A

DOI 10.31489/2021PH4/52-60

UDC 53.07

A.U. Aldiyarov, K.I. Beisenov*, U.P. Suiinzhanova, D.E. Yerezhep

Al-Farabi Kazakh National University, Almaty, Kazakhstan
*(*E-mail: khasen.007@gmail.com)*

Study of polyamorphic transformations in the cryomatrix of nitrogen in cryovacuum condensates of water

One of the important tasks of modern physics of condensed matter is to establish an unambiguous connection between the conditions of formation and the properties of the resulting solid phase. Its solution will contribute to major breakthroughs in the creation of materials with desired properties. As any scientific and technological problem, this approach is associated with the need to address a wide range of fundamental issues. The basis for success in this direction is the implementation of a complex not only with model tests, when the investigated substance is important from a practical point of view, but in itself has interesting physical properties; such objects can be fully attributed to chemical properties. Hydrogen-bonded substances, in which, in addition to van der Waals forces, interactions due to the presence of an intermolecular hydrogen bond play an important role. The obtained method of cryomatrix isolation facilitates assuming that in the process of cryocondensation of pure components of water and ethanol at an intermediate stage in the adsorbed layer, there is a process of formation of clusters with a short-range order similar to the liquid state of water or ethanol.

Keywords: crystallization, mixes, glass transition dynamics, crystal cell.

Introduction

The structure of water crystals is often determined by the presence of hydrogen bonds. This is due to the fact that the water molecule is a symmetric proton donor and acceptor. This distinguishes the water molecule from isoelectronic homologues such as NH_3 and HF. The NH_3 molecule has three protons and one pair, and the HF molecule has one proton and three single pairs. Thus, only in the system of H_2O molecules, hydrogen bonds (H-bonds) completely determine the geometry of H_2O crystals and the properties of condensed water. This is determined by the strong orientation of the H-bond, which means that if a hydrogen atom is between two oxygen atoms, then the spatial organization of such a system cannot be arbitrary. The formation of one hydrogen bond leads to a decrease in the activation barrier for the formation of the next H-bond, and so on. Since this cooperative property of hydrogen bonds is due to the interaction of two with hydrogen, one molecule is acidic and the other is alkaline. In this regard, it seems necessary to pay more attention to the structure of the water molecule [1, 2].

The structure of the water molecule. H_2O molecule consists of two hydrogen atoms and one oxygen atom. When studying the optical spectra of water, it was found that in the absence of motion (without oscillations and rotations), hydrogen and oxygen ions should be located on the vertices of a right triangle with an angle of 104.5°. The nuclei of a water molecule are surrounded by an electron cloud with a radius of 0.138 nm, consisting of positive electrons that are unevenly distributed within the sphere. Two of them are in the first orbit, in the immediate vicinity of the oxygen nucleus and do not play a significant role in the formation of the bond between oxygen and hydrogen, the remaining eight electrons are paired in four eccentric

orbits in the tetrahedral direction from the oxygen nucleus. The charge of the eight electrons completely compensates for the charge of the oxygen nucleus, but the electrons rotating in two orbitals without protons form two negative centers, that is, the single electrons form two arms from the oxygen nucleus to the vertices of the imaginary tetrahedron, the H_2O molecule. The interval between H^+ and O^2 ions in the unexcited state is 0.96 Å . Due to this structure, the water molecule is a dipole, because the density of electrons in the region of O^2 — ions is much higher than in the region of H^+ ions. One can imagine two small bulging water molecules in the region of the protons, as illustrated in Figure 1.

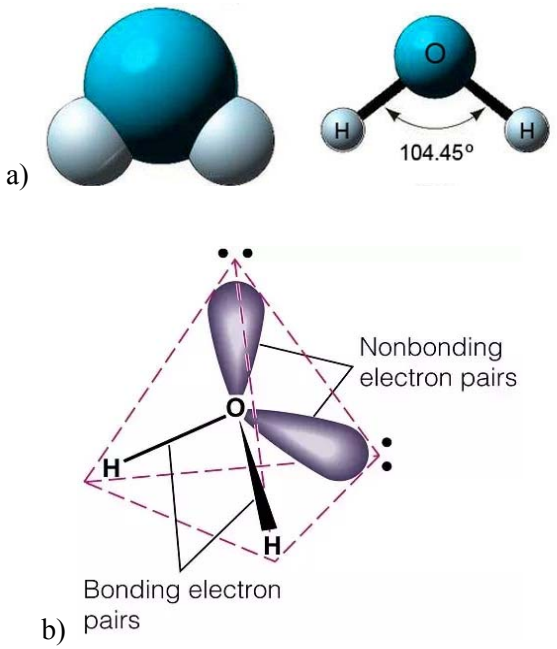

Figure 1. Geometric diagram of the monomer H_2O (a), plane model (b)

Dynamics of water molecules. As in a rigid structure, the nuclei of molecules in a crystal lattice are in a state of continuous oscillation at 0 K. An important feature of these oscillations is that they can be characterized by a limited number of fundamental oscillations, called normal modes. This is an oscillation in which all the nuclei oscillate at the same frequency and in the same phase. The water molecule has three normal modes ν_1, ν_2, ν_3. Any possible vibration of this molecule can be described as a superposition of these three modes.

The oscillations that move the H-nuclei in the direction of the OH bond are called the OH bond oscillations as shown in Figure 2. These oscillations occur at frequencies ν_1 and ν_3. The oscillations in which the H nuclei move in a direction almost perpendicular to the O–H bonds (ν_2 mode), are called the deformation vibrations of the H–O–H bonds or the bending oscillations of the H–O–H bonds. In fact, in the ν_1 mode, the H–O–H bond has a small amount of bending, while in the ν_2 mode, a small amount of O–H elongation corresponds. ν_3 is called asymmetric tensile vibration or asymmetric tensile vibration or asymmetric tensile vibration, and is different from ν_1 symmetric tensile vibration. These frequencies are derived from Raman and infrared spectra [3].

The transition of the water molecule from the basic state of oscillation, described by the mode ν_2, to the excitation corresponds to the infrared absorption band 1595 cm^{-1}. During this transition ν_2 describing the mode υ_2 quantum number varies from 0 to 1, and υ_1 and υ_3 describe the modes, ν_1 and ν_3 are zero quantum numbers. Similarly, the transition of a water molecule from the basic state of oscillation to the state in which only the first normal mode is moving (the state in which the quantum numbers $\upsilon_1=1$, $\upsilon_2=0$, and $\upsilon_3=0$) corresponds to an absorption band of 3657 cm^{-1}. The third normal mode corresponds to an absorption band with a maximum frequency of 3756 cm^{-1}. The given parameters correspond to an empty water molecule. During the transition to the condensed state, there are changes in the parameters of intermolecular interactions, as well as a significant expansion of the absorption bands of fundamental frequencies as a result of the formation of hydrogen bonds and their transition to lower vibration frequencies. This leads, in particular, to the superposi-

tion of the elongated vibration ranges, so that in the condensed states these frequencies are not separated, but are appeared as a single absorption band [4–5].

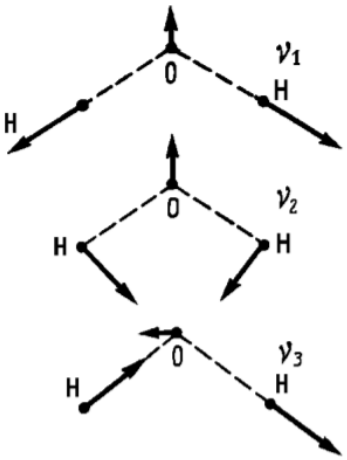

Figure 2. Normal oscillation modes of water molecules

Experimental

When studying the structural and phase transformations in the cryovacuum-condensate in the technological process, it is important to have information about the growth rate, refractive index and reflective characteristics of the cryocondensate-substrate system with a wide frequency range from 4200 to 400 cm^{-1}. To carry out this type of research, the existing experimental equipment was used in the Laboratory of Cryophysics and Cryotechnology of the Faculty of Physics and Technology. In addition, the need for low-temperature measurements and the study of cryocondensation films in the thickness range of 25–30 μm has led to an increase in requirements for both the functional capabilities of a number of important units and its technological parameters. These requirements relate to the maximum vacuum in the operating chamber of the unit, as well as the need to measure in the average IR range (400 cm^{-1}) [6–7].

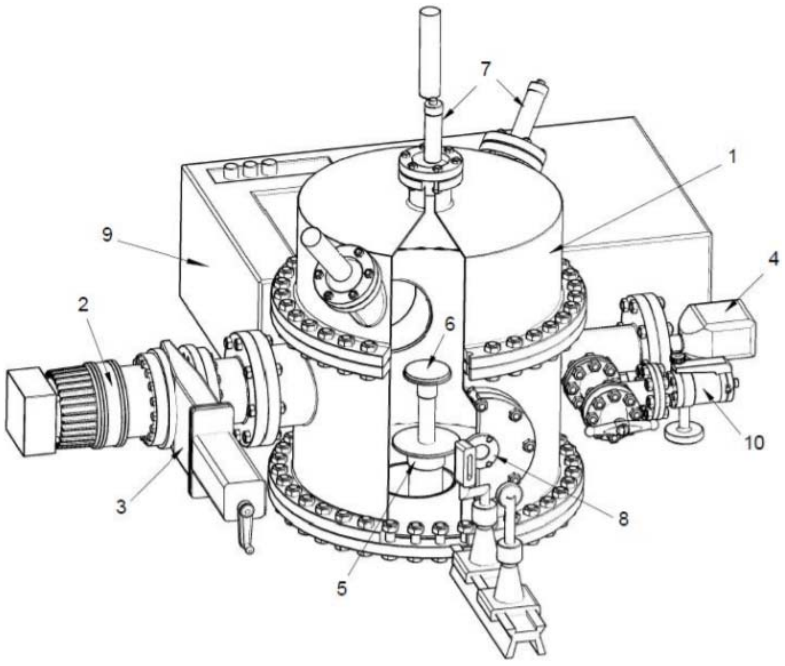

1 – vacuum chamber; 2 – vacuum pump Turbo-V 301; 3 – slide vacuum cover CFF–100;
4 – pressure sensor FRG-700; 5 – Gifford-McMahon refrigerator; 6 – substrate; 7 – laser interferometer;
8 – Optical channel of IR spectrometer; 9 – IR spectrometer; 10 – Leakage system

Figure 3. Schematic of the experimental unit

Figure 3 shows the schematic diagram of a universal vacuum cryogenic spectrophotometer in which a water cryocondensate is obtained in a vacuum chamber. The main installation unit is a cylindrical vacuum chamber with a diameter and height of 450 mm (1). The evacuation of the vacuum chamber was carried out by a turbo-molecular pump (2) Turbo-V 301 connected to the chamber of the CFF-100 sliding gate valve (3). The SH-110 dry circulation pump (not shown) is used as a forevacuum pump). The final vacuum in the chamber reached a value of not less than P=10–^{8} Topp (P=10–^{6} Pa). The pressure in the chamber was measured with a wide-range pressure sensor with FRG-700 controller.

In the center of the chamber is the Gifford-McMahon microcryogenic system (5), on the upper flange of which is mounted a mirror substrate (6), which serves as a surface for ethanol condensation. The substrate is made of copper, its working surface is covered with silver. The diameter of the substrate is d=60 mm. The minimum condensation temperature is T=16K. The temperature was measured with a DT 670–1.4 silicon sensor and a M335/20s temperature controller. Thickness and condensation rate are measured with a two-beam laser interferometer based on P25a-SS-0–100 — photomultiplier tubes (7). The absorption spectra were measured in the frequency range 400 cm^{-1}÷4200 cm^{-1}. Through ADC, the signals of the photomultiplier are sent to the computer and controlled by the PowerGraph program [8].

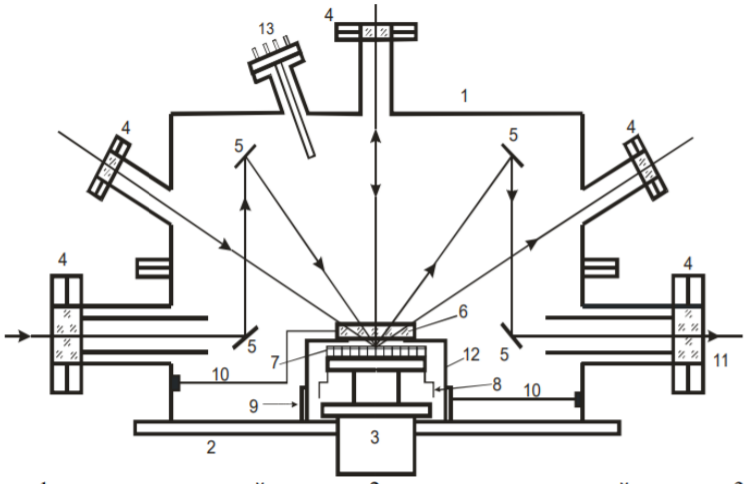

1 — vacuum chamber housing; 2 — the base of the vacuum chamber; 3 — McMahon micro-refrigerator; 4 — optical windows; 5 — light guides; 6 — protective plates KBr; 7 — substrate; 8 — cryopump; 9 — damper; 10 — magnetic drive; 11 — optical window KBr;

Figure 4. Schematic of the vacuum chamber of the spectrophotometer

Figure 4 designates the cross-section of the vacuum chamber of the spectrophotometer. The base of the chamber is a massive plate (2) with a diameter of 450 mm and a thickness of 35 mm. It is equipped with a chamber housing (1) with welded connecting pipes. The camera body is covered by a lid, the presence of which allows to adjust and install the camera. The microcryogenic machine (3) is located at the bottom of the chamber. At the top and body of the cover, there are windows (4) for the introduction of laser interferometer radiation, for measuring the growth rate and controlling the thickness of the sample, as well as for the introduction of globe radiation in the IR range. All vacuum seals of metal prefabricated parts are sealed with copper seals, and salt optics are sealed with Indian seals.

Particularly in Figure 4, by using a magnetic drive (10), it is possible to install and remove a KBr (6) plate on the substrate, the purpose of which is to overlap the work surface (7) with uncontrolled precondensation processes and protect it from secondary processes during heating. The distance between the back and the protective panel is 5 mm. Furthermore, additional copper plates (8) are placed on the low-temperature flange of the micro-refrigerator, which acts as a cryocondensation pump. The protective housing (12) has holes that can be overlapped with the magnetic drive (10) of the cylindrical valve (9) for suction of the cryopump. This increases the basic vacuum level in the chamber. In addition, combining the substrate with a protective film, its overlap with a protective plate creates a closed volume near the substrate, the pressure of which is much lower than the external pressure in the vacuum chamber [9].

The matrix gas treatment system includes additional units of the injection system, the scheme of which is illustrated in Figure 5 [10].

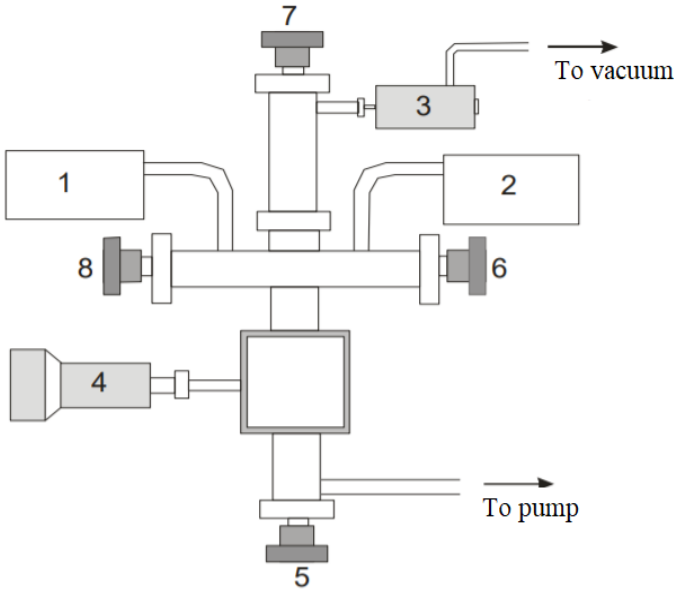

1 — test gas “1”, 2 — test gas “2”, 3 — valves, 4 — baratrons, 5, 6, 7, 8 — taps.

Figure 5. Schematic of the cryodensor vapor extraction system

The temperature of the substrate is measured in thermocouples (Au+0.07 % Fe) — Cu, with an accuracy of at least 0.5 degrees in the lower temperature range; IR spectrometer frequency range 400 cm^{-1}÷4200 cm^{-1} (ICS-29); film thickness — 30 microns (two-beam laser interferometer) [11–13].

As an example, interferons obtained during growth in the substrate at a temperature of ethanol condensate in the substance T = 16 K and a gas phase pressure P=8×10–^{4} Pa (Figure 6).

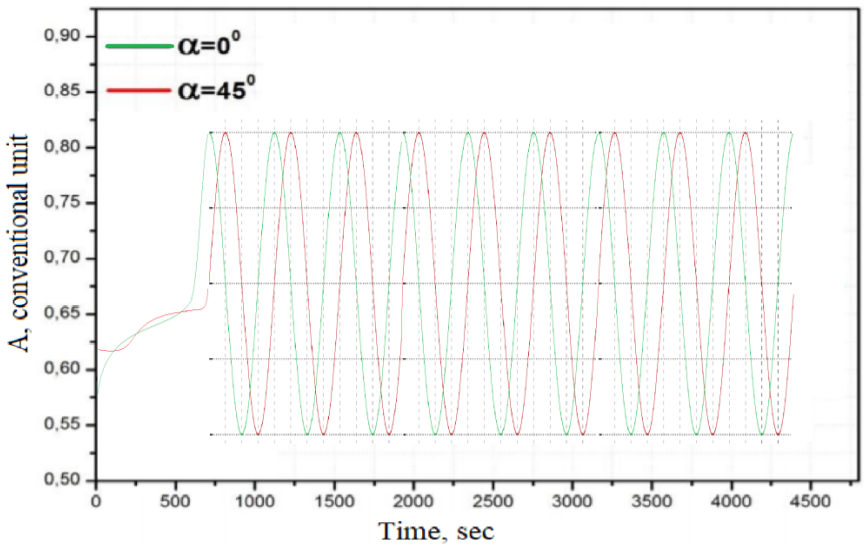

Figure 6. Typical interferograms of condensate film growth

Data registration was performed automatically every 0.5 seconds. The main sources of measurement error are the error in determining the time (interference period) and the angle of incidence. During the alignment of the installation, the angle of incidence of the interferometer was set with an error not exceeding 0.5 %. The error in determining the growth time of the film does not exceed 4.5 % [14–15].

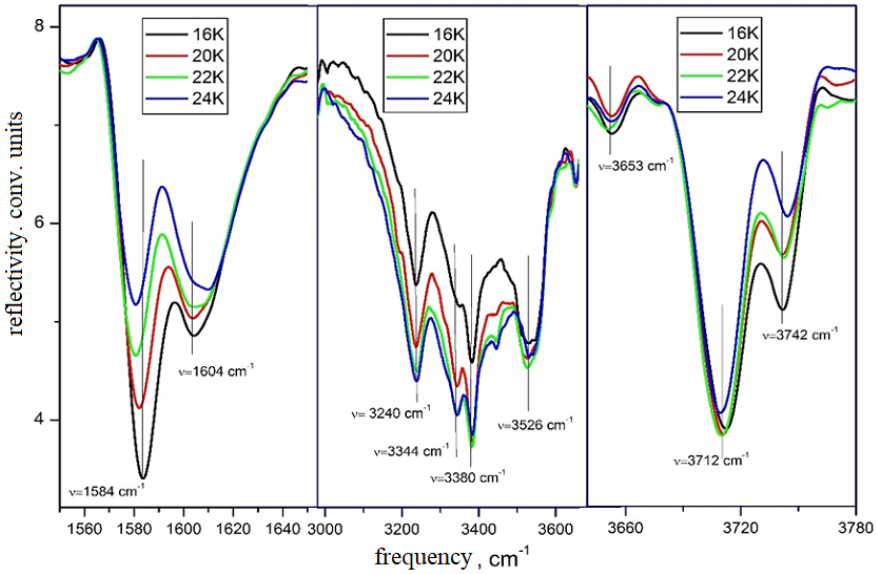

Figure 7. Reflection spectra of water in a nitrogen matrix

In the Fig. 7 the spectra of reflections of the samples in the temperature range of the matrix 16–24 K are given. These are presented in the frequency range of deformation oscillations of water (left drawing), hydrogen-bound states (central drawing) and quasi-free valence symmetric and asymmetric oscillations (right drawing). Similar data are provided in Fig. 8 for the temperature range 26–32 K.

As can be seen from the presented data, the reflection spectra have features specific to matrix-isolated states of water. In the frequency range of deformation curves (left pattern) there are two strips of absorption with a maximum of ν = 1584 cm — 1 and ν = 1604 cm — 1. The first band refers to the deformation oscillations of H_2O monomers in solid nitrogen. The band with a maximum of ν = 1604 cm — 1 can be related to the amount of water polymers in the matrix. In this case, of course, with the increase in temperature of the substrate, the monotonous decrease in the amplitude of the oscillations of the monomers is accompanied by the growth rate of absorption of the polymer.

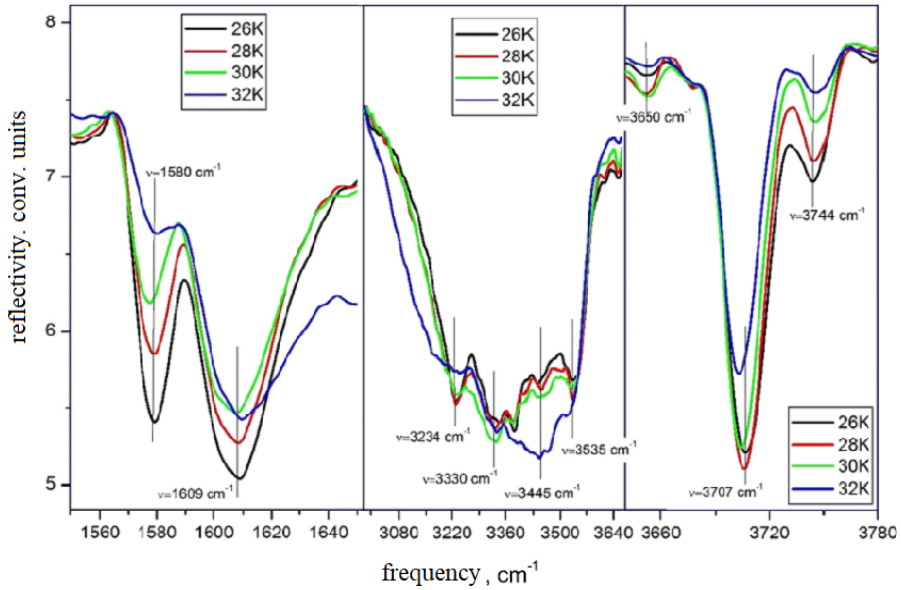

Figure 8. Reflection spectra of water in a nitrogen matrix

The matrix temperature range (Figure 8) is from 26 K to 32 K in the frequency ranges of bending vibrations (left figure), hydrogen-bonded states (central figure), and quasi-free stretching symmetric and asymmetric vibrations (right figure).

The central fragments of Fig. 7 and 8 represent the frequency range of hydrogen-bonded O–H bonds. The spectra given in this range and their agreement with these allow to make assumptions about the availability of polyaggregates of different scales. Thus, the minimum at a frequency of 3234 cm — 1 corresponds to the square meters, the absorption at a frequency of 3330 cm — 1 corresponds to the polymer, and the peak at a frequency of 3526 cm — 1 can relate to the dimers [16]. We do not plan to analyze in detail the cluster composition of the model in this work. It is important to note that the increase in the temperature of the matrix at low temperatures leads to the transformation of spectra in this frequency range.

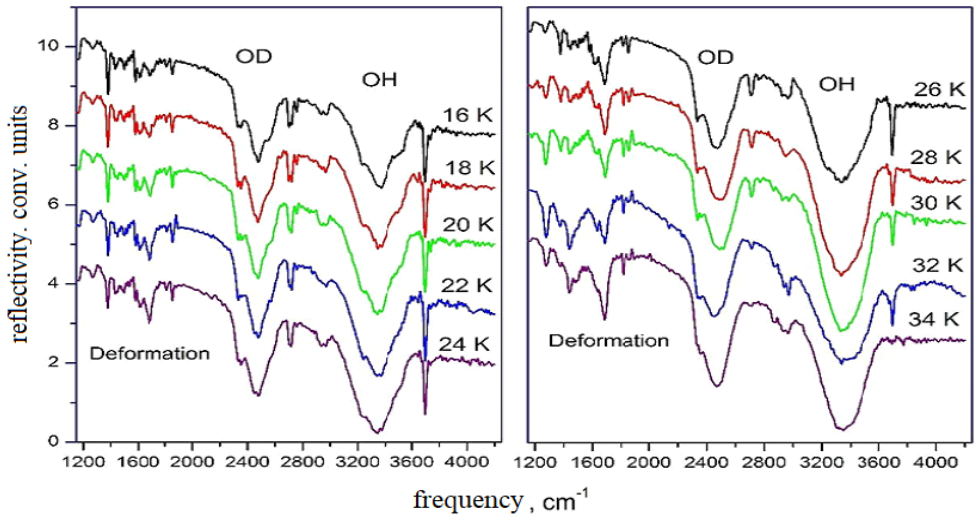

Figure 9. Reflection spectra of an isotopic mixture of water (3 %)
in a nitrogen cryomatrix at different substrate temperatures

Figure 9 demonstrates data in the frequency range of bending and stretching vibrations of the O–H and O–D bonds. As can be seen from the figure, the vibrational spectra contain features characteristic of matrix-isolated systems, in which aggregates of water and heavy water of various sizes are present. A gradual increase in the temperature of the sample leads to a transformation of the spectrum, but the degree of these transformations is different for different types of vibrations of molecules of the isotopic mixture of water.

Conclusions

In accordance with our data, it can be argued that the temperature of the transition from glassy amorphous ice to the state of a superviscous liquid is Tg = 137 K ± 2 degrees. A further increase in temperature leads to a stepwise transformation in the layer. This may be associated with competing crystallization processes through the growth of cubic and hexagonal nuclei, as well as direct crystallization of liquid superviscous water formed at Tg and existing together with the crystalline phase up to temperatures of about 200 K.

Our studies revealed the anomalous behavior of the samples at temperatures preceding sublimation. This is the abrupt behavior of the heating curve, which is accompanied by an extremum pressure in the chamber. In our opinion, these experimental data confirm the point of view expressed in the works [17]. The point is that a multicomponent system consisting of amorphous and crystalline components at a fixed temperature should have different equilibrium pressures of the gas phase corresponding to the partial activation energies of sublimation. Because if the activation energy of the amorphous form of ice is greater than the corresponding values for crystalline modifications, this will lead to the fact that at high temperatures amorphous water will evaporate at an earlier stage, and then recondense on crystalline components into a crystalline form.

Acknowledgments

The study has been carried out with the financial support of the Ministry of Education and Science of the Republic of Kazakhstan under grant AP08855738.

References

1 Bjerrum N. Structure and properties of ice / N. Bjerrum // Science. — 1952. — Vol. 115, № 2989. — P. 385–390.

2 Bertie J.E. Infrared spectra of ices II, III and V in the range 4000–350 cm^{-1} / J.E. Bertie, E. Whalley // The Journal of Chemical Physics — 1964. — Vol. 40, № 8. — P. 1637–1645.

3 Gonzalez L. Density functional theory study on ethanol dimers and cyclic ethanol trimers / L. Gonzalez, O. Mo, M. Yanez // The Journal of Chemical Physics — 2019. — Vol. 111. — P. 3855.

4 Parent Ph. Structure of the water ice surface studied by x-ray absorption spectroscopy at the O K-edge / Ph. Parent, C. Laffon, C. Mangeney, F. Bournel, M. Tronc // The Journal of Chemical Physics. — 2002 — Vol. 117 — P. 10842.

5 Yue1 Y. Clarifying the glass-transition behaviour of water by comparison with hyperquenched inorganic glasses / Y. Yue1, C.A. Angell // Nature. — 2004. — Vol. 427, № 19. — P. 717–720.

6 Sivakumar T.C. Raman spectroscopic studies of the OH stretching region of low density amorphous solid water and of polycrystalline ice Ih / T.C. Sivakumar, S.A. Rice, M.G. Sceats // The Journal of Chemical Physics — 1978. — Vol. 69, № 8. — P. 3468–3476.

7 Зацепина Г.Н. Физические свойства и структура воды / Г.Н. Зацепина. — М.: Изд-во Моск. ун-та, 1987. — 171 с.

8 Алдияров А. ИК-спектрометрическое исследование тонкопленочных криовакуумных конденсатов метана и смеси метана и воды / А. Алдияров, М. Арюткина, А. Дробышев // Физика низких температур. — 2011. — Т. 37. — № 6. — С. 524.

9 Drobyshev A. Metastability of ethanol nanoclusters in nitrogen cryomatrix / A. Drobyshev, A. Aldiyarov, K. Katpaeva, E. Korshikov, V. Kurnosov, D. Sokolov // Physics of low temperatures — 2013. — Vol. 39. — P. 11.

10 Whalley E. Crystal structures of the high-pressure forms of ice / E. Whalley // Transactions of the Faraday Society — 1958. — Vol. 54, № 6. — P. 1613.

11 Zimmerman R. The infrared spectrum of ice; temperature dependence of the hydrogen bond potential function / R. Zimmerman, G. Pimental // Advances in molecular spectroscopy, New York Bentwood. — 1962. — Vol. 2. — P. 726–737.

12 Пиментел Д. Водородная связь / Д. Пиментел, О. Мак-Клеллан. — М.: Мир, 1964. — 462 с.

13 Сергеев Д.М. О резонансном туннелировании квазичастиц через наноконтакт «алюминий—оксид алюминия—алюминий» при низких температурах / Д.М. Сергеев, С.К. Кущанов // Вестн. Караганд. ун-та. Сер. Физика. — 2017. — 2(86). — С. 21–29.

14 Антонченко В.Я. Основы физики воды / В.Я. Антонченко, А.С. Давыдов, В.В. Ильин. — Киев: Наук. думка, 1991. — 672 с.

15 Haas C. Properties and lattice intersections of ice / A.J. Tursi, C. Haas // Tech. Rep. 5, Frick chemistry laboratory, Princeton Univ. — Princeton, 1960. — P. 273.

16 Tursi A.J. Matrix-isolation study of the water dimer in solid nitrogen / A.J. Tursi, E.R. Nixon // The Journal of Chemical Physics — 2012. — Vol. 52. — P. 1521.

17 Дробышев А. ИК-спектрометрические и термодесорбционные исследования полиморфных и полиаморфных превращений в криовакуумных льдах воды / А. Дробышев, А. Алдияров, Д. Жумагалиулы, В. Курносов, Н. Токмолдин // Физика низких температур. — 2014. — Т. 33. — С. 627.

А.У. Алдияров, Х.И. Бейсенов, Ұ.П. Сүйінжанова, Д.Е. Ережеп

Полиаморфты өзгерістерді судың криовакумды конденсаттарындағы нитрогенді криоматрицаларын зерттеу

Конденсацияланған заттың қазіргі заманғы физикасының маңызды міндеттерінің бірі – түзілу шарттары мен нәтижесінде пайда болған қатты фазаның қасиеттері арасында бірмәнді байланыс орнату. Оның шешімі қажетті қасиеттері бар материалдарды жасаудағы үлкен жетістіктерге ықпал етеді. Кез келген ғылыми-техникалық мәселелер сияқты, бұл тәсіл де кең ауқымды сұрақтарды шешу қажеттілігімен байланысты. Бұл бағыттағы табыстың негізі кешенді тек модельдік сынақтармен жүзеге асыру болып табылады, егер зерттелетін зат практикалық тұрғыдан маңызды болса, бірақ өзі қызықты физикалық қасиеттерге ие болса; мұндай объектілерді химиялық қасиеттерге толық жатқызуға болады. Сутегі байланысқан заттар, оларда ван-дер-Ваальс күштерінен басқа, молекулааралық сутегі байланысының болуына байланысты өзара әрекеттесу маңызды рөл атқарады. Алынған криоматриксті оқшаулау әдісі адсорбцияланған қабаттағы аралық сатыдағы су мен этанолдың таза компоненттерін криоконденсациялау процесінде сұйық күйге ұқсас қысқа диапазонды кластерлер түзілу процесі жүреді деген болжам жасайды.

Кілт сөздер: кристалдану, қоспалар, әйнектің ауысу динамикасы, кристалл жасушасы, криоконденсация.

А.У. Алдияров, Х.И. Бейсенов, Ұ.П. Сүйінжанова, Д.Е. Ережеп

Исследование полиаморфных превращений в криоматрице азота в криовакуумных конденсатах воды

Одна из важных задач современной физики конденсированного состояния — установить однозначную связь между условиями образования и свойствами образующейся твердой фазы. Его решение будет способствовать крупному прорыву в создании материалов с заданными свойствами. Как и любая научно-техническая проблема, такой подход связан с необходимостью решения широкого круга фундаментальных проблем. Основой успеха в этом направлении является выполнение комплекса не только модельных испытаний, когда исследуемое вещество важно с практической точки зрения, но само по себе имеет интересные физические свойства. К таким объектам в полной мере можно отнести химические свойства. Вещества с водородными связями, в которых, помимо сил Ван-дер-Ваальса, важную роль играют взаимодействия, обусловленные наличием межмолекулярной водородной связи. Полученный метод криометрического выделения делает предположение, что в процессе криоконденсации чистых компонентов воды и этанола на промежуточной стадии в процессе адсорбции происходит образование кластеров, сосуществующих друг с другом.

Ключевые слова: кристаллизация, смеси, динамика стеклования, кристаллическая ячейка, процесс криоконденсации.

References

1 Bjerrum, N. (1952). Structure and properties of ice. *Science.* 385–390.

2 Bertie, J.E. & Whalley, E. (1964). Infrared spectra of ices II, III and V in the range 4000–350 cm-1. *The Journal of Chemical Physics, 40, 8,* 1637–1645.

3 Gonzalez, L., Mo, O. & Yanez, M. (2019). Density functional theory study on ethanol dimers and cyclic ethanol trimers. *The Journal of Chemical Physics,* 111, 3855.

4 Parent, Ph., Laffon, C., Mangeney, C., Bournel, F., & Tronc M. (2002). Structure of the water ice surface studied by x-ray absorption spectroscopy at the O K-edge. *The Journal of Chemical Physics,* 117, 10842.

5 Yue1, Y. & Angell, C.A. (2004). Clarifying the glass-transition behaviour of water by comparison with hyperquenched inorganic glasses. *Nature,* 427, 19, 717–720.

6 Sivakumar, T.C., Rice, S.A. & Sceats, M.G. (1978). Raman spectroscopic studies of the OH stretching region of low density amorphous solid water and of polycrystalline ice Ih. *The Journal of Chemical Physics.* 69, 8, 3468–3476.

7 Zatsepina, G.N. (1987). *Fizicheskie svoistva i struktura vody [Physical properties and structure of water]*. Moscow: Izdatelstvo Moskovskogo universiteta [in Russian].

8 Aldiiarov, A., Ariutkina, M. & Drobyshev, A. (2011). IK-spektrometricheskoe issledovanie tonkoplenochnykh kriovakuumnykh kondensatov metana i smesi metana i vody [IR spectrometric study of thin-film cryovacuum condensate methane and methane mixtures and water]. *Fizika nizkikh temperatur — Physics of low temperatures,* 37 (6), 524 [in Russian].

9 Drobyshev, A., Aldiyarov, A., Katpaeva, K., Korshikov, E., Kurnosov, V., & Sokolov, D. (2013). Metastability of ethanol nanoclusters in nitrogen cryomatrix. *Physics of low temperatures,* 39, 11.

10 Whalley, E. (1958). Crystal structures of the high-pressure forms of ice. *Transactions of the Faraday Society,* 54, 6, 1613.

11 Zimmerman, R. & Pimental, G. (1962). The infrared spectrum of ice; temperature dependence of the hydrogen bond potential function. *Advances in molecular spectroscopy, New York Bentwood, 2,* 726–737.

12 Pimentel, D. & Mak-Klellan, O. (1964). *Vodorodnaia sviaz [Hydrogen bond]*. Moscow: Mir [in Russian].

13 Sergeev, D.M. & Kushchanov, S.K. (2017). O rezonansnom tunnelirovanii kvazichastits cherez nanokontakt «aliuminii – oksid aliuminiia – aliuminii» pri nizkikh temperaturakh [About resonance tunneling of quasiparticles through nanocontact “aluminum—aluminium oxide—aluminum” at low temperatures]. *Vestnik Karagandinskogo universiteta. Seriia Fizika — Bulletin of the Karaganda University – Physics,* 2 (86), 21–29 [in Russian].

14 Antonchenko, V.Ya., Davydov, A.S. & Ilin, V.V. (1991). *Osnovy fiziki vody [Basics of water physics]*. Kiev: Naukova Dumka [in Russian].

15 Haas, C. (1960). Properties and lattice intersections of ice. *Tech. Rep. 5, Frick chemistry laboratory Princeton University — Princeton.*

16 Tursi, A.J. & Nixon E.R. (2012). Matrix-isolation study of the water dimer in solid nitrogen. *The Journal of Chemical Physics*, 52, 1521.

17 Drobyshev, A., Aldiiarov, A., Zhumagaliuly, D., Kurnosov, V., & Tokmoldin, N. (2014). IK-spetkrometricheskie i termodesorbtsionnye issledovaniia polimorfnykh i poliamorfnykh prevrashchenii v kriovakuumnykh ldakh vody [IR spectrometric and thermodesorption studies of polymorphic and polyamorphic transformations in cryovacuum water bodies]. *Fizika nizkikh temperatur — Physics of low temperatures,* 627 [in Russian].

DOI 10.31489/2021PH4/61-67

UDC 536.5

A.P. Sarode[1*], O.H. Mahajan[2]

[1]*Dr. A. G. D. Bendale Girls College, Jalgaon, India*
[2]*Department, M.J. College, Jalgaon, India*
(*)*E-mail: abhijitsarode@yahoo.com)*

Theoretical aspects of Photoacoustic Signal Generation with Solid Crystals

Today, non-destructive analysis techniques play an important role in industrial applications and scientific, as well as technological research. Photoacoustic method is one of such non-destructive methods in which generation of acoustic waves takes place due to the absorption of the modulated incident radiation. Photoacoustic signal is a base for photoacoustic research. The generation of the photoacoustic signal is related to the nature of the cell used for investigation. Though a variety of explainations about signal generation in photoacoustic interaction are reported by many researchers, many aspects are yet to be studied in detail. While investigating a solid crystal in photoacoustics, factors as mode of operation, scheme of excitation, the shape of the cell, and pressure fluctuations in the cell are considered for analysing photoacoustic signal generation. Also, design and performance optimization of the photoacoustic cell play paramount role in determining efficiency of related signal generation. In this paper, theoretical aspects of photoacoustic signal generation for solid crystals are presented. While obtaining the expression for pressure fluctuations with solid crystal, cylindrical configuration of photoacoustic cell is preferred to get a better signal–to–noise ratio. Along with the analysis of other factors, pressure fluctuations generated by the enclosed gas in photoacoustic cell is mathematically determined.

Keywords: photoacoustic signal, solid crystal, energy transfer, light–matter interaction, non-radiative de-excitation, photoacoustic cell, photoacoustic transducers.

Introduction

A.G. Bell discovered photoacoustic effect in 1880 by using solar radiation, a chopper and an earphone as an acoustic sensor [1]. The generation of acoustic waves due to light absorption in the target material is called as photoacoustic effect [2, 3]. After the invention of laser, photoacoustic research changed drastically. When a laser beam is passed through a solid crystal placed in a closed cell, absorption of laser energy in the molecules of the crystal leads to the generation of photoacoustic signal [4, 5].

Several researchers studied various aspects of photoacoustic signal in the last three decades. Across two media interfaces, studies on heat transfer and effect of solid – gas thermal contact resistance on photoacoustic signal generation were amply discussed [6]. The pulse shape of the photoacoustic signal in the form of cylindrical ultrasonic pressure waves generated by the irradiation of laser in a weakly absorbing liquid was described [7]. In pulsed photoacoustic spectroscopy, signals have been studied to describe origin of the complex transients [8]. Attenuation and deformation of the photoacoustic signal due to thermoelastic and viscose losses were also studied [9]. The study of nano-scale temperature rises on photoacoustic signal generation based on thermal nonlinearity of optical absorbers gave a new dimension to this field [10]. Photoacoustic signal amplitude and its relationship with concentration of the gas enclosed in the cell were experimentally studied as well. The researchers also studied the stability of photoacoustic signals generated while studying trace gas components [11]. Recently theoretical aspects of transient temperature on cubic crystal surface during photoacoustic signal generation has been described [12]. Along with the other research, mathematical aspects of displacement fields of a cuboid crystal in photoacoustic signal generation in a cell are discussed [13].

Processess in Photoacoustic Signal Generation

The creation of thermal energy within the sample is caused by non-radiative de-excitation processes that ordinarily occur in the photoacoustic cell [14]. After modulating the incident radiation, the creation of thermal energy within the sample will be periodic and will result in a thermal or pressure wave having the same frequency as that of modulation. The thermal wave or pressure wave transfers energy to the sample boundary, which results in a periodic temperature shift [15]. The creation of an acoustic wave in the adjacent surrounding gas to the crystal is caused by a periodic variation in the temperature at the sample's surface and this wave propagates through the volume of the gas to the detector where a signal is produced [16]. When

this detector or microphone signal is plotted as a function of wavelength, it represents a spectrum that is proportional to the crystal's absorption spectrum.

Factors involved in photoacoustic signal generation

The important factors involved in photoacoustic signal generation with a solid crystal are

1) Operation mode;
2) Method of Excitation;
3) Structure of the cell;
4) Pressure fluctuations in the cell.

Operation Mode

The confined air around the crystal in a closed photoacoustic cell will vibrate according to the modulation frequency of the source of the incident radiation. When the mode of operation is resonant, one of the resonant frequencies of the signal in the cavity will be the modulation frequency of the incident source. The pressure fluctuations in the cell will generate an acoustic wave whose amplitude will be amplified at the frequency of modulation of the incident radiation. The signal's amplification will be proportional to the quality factor Q. The relationship between the signal's resonant frequency and its bandwidth is represented by the quality factor. To amplify just the modulating frequency of the produced signal inside the cell, a significant gap between neighboring resonance frequencies, as well as a high–quality factor should be maintained [17]. The amplification of all remaining resonant frequencies will be inversely proportional to the difference between the square of modulating frequency and the square of produced signal's resonant frequency. If the photoacoustic cell is operating in resonant mode, then implemented modulation frequencies are relatively high – about 3 kHz. The goal of this selection is to reduce noise that is correlated with the reciprocal of the frequency.

External acoustic noise, noise due to amplification, and intrinsic noise of the detector are all associated with each other. For higher frequencies, the cavity length is shorter. Therefore, an intermediate value between a longer absorption length and a shorter cavity length should be preferred while choosing the resonant frequency. Mostly, smaller cavity lengths are recommended in order to have a compact cell with a faster response time [18].

Method of Excitation

The photoacoustic effect is based on sample heating caused by optical absorption, as previously stated. Periodic heating and cooling of the sample are required to generate pressure fluctuations in order to create acoustic waves that can be monitored by pressure-sensitive transducers.

Modulated Excitation

Radiation sources whose intensity changes periodically in the shape of a square or sine wave, resulting in a 50 percent duty cycle, are used in modulated excitation systems. This can be achieved by, for example, mechanically chopping light source. To overcome the barrier of the 50 percent duty cycle, option to vary the phase of the emitted radiation rather than the amplitude is preferred. The determination of UV or IR absorption spectra of opaque solid crystals is done using chopped or modulated lamps or IR sources from commercial spectrometers [19].

The most popular sources for photoacoustic analysis are modulated continuous–wave lasers. The photoacoustic cell is a crucial part of the photoacoustic effect. This fact can be used to improve signal quality via acoustic resonance. Therefore, acoustic resonance curves must be taken into account while designing photoacoustic cells.

Pulsed Excitation

Laser pulses with durations in the nanosecond range are commonly used for excitation in pulsed photoacoustic spectroscopy. Since the repetition rates are only a few Hz, the outcome is a short period of illumination followed by a considerably longer period of darkness, resulting in a low duty cycle. This causes the sample medium to expand rapidly and adiabatically, resulting in a short shock pulse. In such cases, data analysis is done in the time domain. Hence, oscilloscopes, boxcar systems, and fast A to D converters are used to record the signal. The frequency – domain transformation of the signal pulse produces a wide spectrum of acoustic frequencies up to the ultrasonic range [20]. In this way, laser beams modulated in the form

of short laser pulses generate broadband acoustic sources and a sine wave of a laser excites a single acoustic frequency.

Structure of the cell

The internal cavity of a resonant photoacoustic cell is fabricated to the appropriate size to match the acoustic wavelength of the photoacoustic signal [21]. Figure 1 shows a schematic representation of a cylindrical photoacoustic cell for a solid crystal. By attaching additional buffers to the central section of the cell, having different cross-sections, its structure can be modified. The addition of buffers helps to avoid noise caused by the cell's coupling with other measuring equipment.

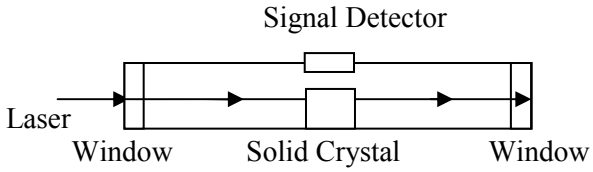

Figure 1. A schematic diagram of cylindrical photoacoustic cell for a solid crystal

A one-dimensional photoacoustic cell is a resonator with short dimensions that is oriented perpendicularly to the propagating acoustic signal. Standing acoustic waves produced by exciting sound signals are amplified when propagating sound waves are reflected back into the cell if the phase difference between the waves is 2π or, in its multiple. The phase difference is dependent upon the reflections of waves at the ends of the cell, as well as the acoustic path length. A pressure antinode will be formed at the closed end of the cell. The cell material has a higher acoustic impedance than that of air is the reason for this phenomenon [22].

Because of the matching nature with the symmetry of the laser beam, the cylindrical form of the photoacoustic cell is the most common for a small size acoustic sensor or a microphone, the measured signal is proportional to the amplitude of pressure fluctuations at its position. By placing the sensor at the node of the generated amplified wave, unwanted sound signals, generated in resonance from the external sources, can be reduced. For a cylindrical photoacoustic cell, desired value of the Q factor value can be set up to 900.

Pressure fluctuations in the cell

Let $þ$ be the pressure fluctuation in the gas, T be its temperature, and V be its volume surrounding the crystal in a closed photoacoustic cell. The change in pressure in the surrounding gas is given by

$$d\text{þ} = \left(\frac{\partial \text{þ}}{\partial T}\right) \text{V dT} + \left(\frac{\partial \text{þ}}{\partial V}\right) \text{T dV}. \quad (1)$$

It has been assumed that (a) conduction of heat from the enclosed gas in the cell to the gas outside the cell is negligibly small, (b) the sample dilation has negligible impact on the model of mechanical piston, (c) heat energy distribution in the solid sample has uniform nature along its plane, (d) during laser absorption, only thermoelastic bending is considered. This situation is schematically represented in Figure 2.

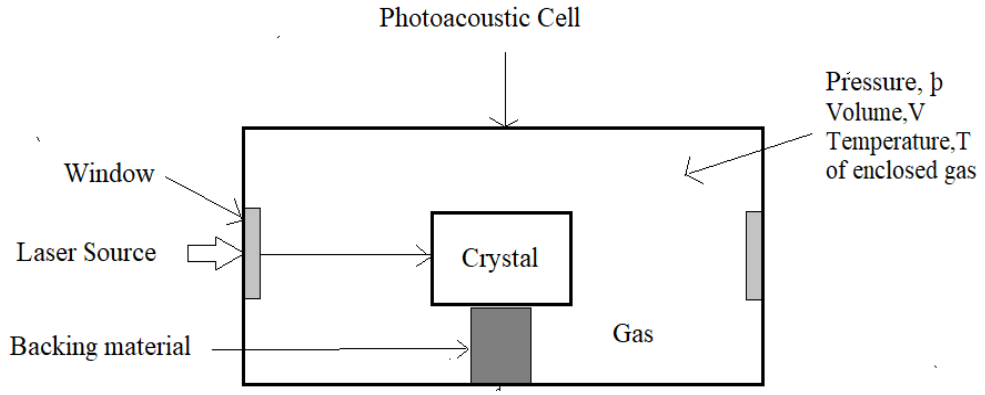

Figure 2 : A crystal kept in a Photoacoustic Cell

For ideal gas, at constant volume,

$$\left(\frac{\partial p}{\partial T}\right) = \frac{\text{þ}}{\text{T}}, \tag{2}$$

At constant temperature,

$$\left(\frac{\partial p}{\partial V}\right) = -\frac{\text{þ}}{\text{V}}. \tag{3}$$

Here, p is assumed to be uniform in the cell. According to the condition of structural design,

$$l_g < \frac{\text{As}}{2}. \tag{4}$$

So, the pressure fluctuation in the cell becomes

$$d\text{þ} = \frac{\text{þ}}{\text{T}}\, d\text{T} - \frac{\text{þ}}{\text{V}}\, d\text{V}. \tag{5}$$

If σ is internal stress, ρ is density of the material of the crystal, u be the displacement field in the crystal and $\frac{\partial^2 u}{\partial t^2}$ be the second derivative of displacement field in the crystal, then

$$\left(\frac{\partial \sigma}{\partial x}\right) = \rho\, \frac{\partial^2 \text{u}}{\partial \text{t}^2} \tag{6}$$

According to the Landau and Lifshitz [23],

$$\sigma = -\text{K}\beta\,(\Delta\text{T})\,\delta + 2\mu\left(\frac{\partial u}{\partial t} - \frac{\delta}{3}\,\frac{\partial^2 \text{u}}{\partial \text{t}^2}\right) + \text{Ku} \tag{7}$$

where K is isothermal compressibility having value

$$\text{K} = -\,\frac{1}{\text{V}}\frac{\partial \text{V}}{\partial \text{þ}}, \tag{8}$$

at constant temperature and β is thermal expansion coefficient of the material of the crystal, whose value is

$$\beta = \frac{1}{\text{V}}\frac{\partial \text{V}}{\partial \text{T}}, \quad \text{at constant pressure þ.} \tag{9}$$

Substituting this value in equation (6),

$$\mu\left(\frac{\partial^2}{\partial \text{x}^2} + \frac{\partial^2}{\partial \text{y}^2} + \frac{\partial^2}{\partial \text{z}^2}\right)^2 \text{U} + \left(\text{K} + \frac{\mu}{3}\right)\nabla\nabla\text{u} - \rho\,\frac{\partial^2 \text{u}}{\partial \text{t}^2} = \text{K}\beta\,(\Delta\text{T}). \tag{10}$$

If Δs is change in the surface area of the crystal surface due to the thermal expansion, and if $\Delta\theta$ is temperature fluctuations in the same surface, then the pressure fluctuations in the enclosed gas in the cell are given by

$$d\text{þ} = \frac{\text{þ}}{\text{T}}\, d\text{T} - \frac{\text{þ}}{\text{V}}\,\Delta\text{s} + \frac{\text{þ}}{\text{T}}\,\Delta\theta. \tag{11}$$

Conclusions

An exact equation for pressure fluctuations in the enclosed gas around the solid crystal kept in a cylindrical–shaped photoacoustic cell is exactly determined. This expression allows the calculation of various parameters of photoacoustic signal related to solid crystal in the designed photoacoustic cell. The signal dependence in terms of operation mode, method of excitation, and structure of the cell is theoretically presented. This theoretical approach constitutes an important step towards the determination of various

aspects of photoacoustic signal generation for solid crystals. This work will be useful in photoacoustic research to explore more scientific and industrial applications in various fields in the future.

References

1 Rosencwaig, A. & Gersho, A. (1976). Theory of the photoacoustic effect with solids. *Journal of Applied Physics, 47,* 64–68.

2 West, G., Barrett, J.J., Siebert, D.R., & Reddy, K.V. (1983). Photoacoustic Spectroscopy. *Review of Scientific Instruments, 54:7,* 797–817.

3 McDonald, F.A. & Wetsel, G.C.Jr.(1978). Generalized Theory of the Photoacoustic Effect. *Journal of Applied Physics, 49:4,* 2313–2322.

4 Sigrist, M.W. (1999). Photoacoustic spectroscopy, method and instrumentation. *Encyclopedia of spectroscopy and spectrometry. Vol. 3,* 1810–1812.

5 Silfvast, W.T. (2004). *Laser Fundamentals,* Cambridge University Press, Cambridge.

6 Lima, C.A.S., Miranda, L.C.M., & Santos, R. (1981). Sample gas thermal contact resistance and the photoacoustic signal generation. *Journal of Applied Physics. 52,* 137–140.

7 Kuo, C.Y., Vieira, M.M.F. & Patel, C.K.N. (1984). Transient optoacoustic pulse generation and detection. *Journal of Applied Physics. 55,* 3333–3336.

8 Schurig, D.A., Klunder, G.L., Shannon, M.A., & Russo, R.E. (1992). Signal analysis of transients in pulsed photoacoustic spectrpscopy. *Review of Scientific Instruments, 64 (2),* 363–373.

9 Hoelen, C.G.A. & de Mul, F. F. M. (1999). A new theoretical approach to photoacoustic signal generation. *Journal of the Acoustical Society of America, 106*, 695–706.

10 Simandoux, O., Prost, A., Gateau, J., & Bossy, E. (2015). Influence of nanoscale temperature rises on photoacoustic generation: Discrimination between optical absorbers based on thermal nonlinearity at high frequency. Photoacoustics, 3 (1), 20–25. doi:10.1016/j.pacs.2014.12.002

11 Zhu, Z., Luo, J., Liu, J., & Fang, Y. (2020). Effects of pressure and noise on the stability of photoacoustic signals of trace gas components. International Journal of Agricultural and Biological Engineering, 13 (5), 187 — 193.

12 Sarode, A.P. & Mahajan, O.H. (2020). Theoretical aspects of transient temperature on cubic crystal surface in a photoacoustic effect. *Bulletin of the Karaganda University – Physics, 2020–99(3),* 73–79. DOI 10.31489/2021PH4/10.31489/2020Ph3/73–79.

13 Sarode, A.P. & Mahajan, O.H. (2021). Displacement fields of a Cuboid crystal in a Photoacoustic Cell: Mathematical aspects. *Bulletin of the Karaganda University – Physics, 1(101),* 6–11. DOI 10.31489/2021PH4/10.31489/2021Ph1/6–11.

14 Mandelis, A. (1987). Photoacoustic and Thermal Wave Phenomena in Semiconductors, North-Holland, Amsterdam.

15 Malin'ski M. (2005). Determination of air-tightness of the packaging of electronic devices by the thermoacoustic method. *Arch. Acoust., 30 (3),* 345–355.

16 Wilcken, K. & Kauppinen, J. (2003). Optimization of a Microphone for Photoacoustic Spectroscopy. *Applied Spectroscopy, 59:9,* 1087–1092.

17 Chrobak, L. & Malinski, M. (2013). Design and optimization of the photoacoustic cell for nondestructive photoacoustic spectroscopy, *Nondestructive Testing and Evaluation, 28, No. 1,* 17–27. http://dx.doi.org/10.1080/10589759.2012.667408

18 Raghu, O. & Philip, J. (2003). A dual channel photoacoustic cell for imaging experiments on solid samples. *J. Instrum. Soc. India, 33 (3),* 155–158.

19 Chrobak L. & Malinski M. (2009). Transmission and absorption based photoacoustic methods of determination of the optical absorption spectra of Si samples — comparison, *Solid State Commun., 149,* 1600–1604.

20 Rabasovic, M.D., Nikolic, J.D., Markushev, D.D., & Jovanovic-Kurepa, J. (2008). Pulsed photoacoustic gas cell design for low pressure studies, *Optical. Materials, 30,* 1197–1200.

21 Jorge M.P.P.M., Mendes Filho J., Oliveira A.C., Braga A.J.P, Cesar C.L., Morato S.P., Vieira Jr, N.D., & Vieira M.M.F. (1999). *Resonant photoacoustic cell for low temperature measurements, Cryogenics, 39,* 193–195.

22 Yehya, F. & Chaudhary, A. K. (2011). Designing and modeling of efficient resonant photoacoustic sensors for spectroscopic applications. *Journal of Modern Physics. 2,* 200–209.

23 Landau, L.D. & Lifshitz, E. M. (1987). *Fluid Mechanics,* Pergamon Press, Oxford.

А.П. Сароде, О.Х. Махаджан

Қатты кристалды фотоакустикалық дабылдарды генерациялаудың теориялық аспектілері

Бүгінгі таңда беріктік бақылау әдістері өнеркәсіптік қолдануда, сонымен қатар, ғылыми жаңа технологиялық зерттеулерде маңызды рөл атқарады. Фотоакустикалық әдіс — бұл беріктік бақылау әдістерінің бірі, онда акустикалық толқындардың пайда болуы модуляцияланғаннан түскен сәулеленуді сіңіру арқылы жүреді. Фотоакустикалық дабыл фотоакустикалық зерттеулердің негізі болып табылады. Фотоакустикалық дабылдың пайда болуын зерттеу қолданылатын ұяшықтың

табиғатымен байланысты. Көптеген зерттеушілер фотоакустикалық өзара әрекеттесу кезінде дабыл генерациясының әртүрлі түсіндірмелері туралы есеп берсе де, бірқатар аспектілері әлі егжей-тегжейлі зерттелмеген. Фотоакустикадағы қатты кристалды зерттеу кезінде фотоакустикалық дабылдың пайда болуын талдау үшін жұмыс режимі, қозу схемасы, ұяшық пішіні және ұяшықтағы қысымның ауытқуы сияқты факторлар ескеріледі. Сонымен қатар, фотоакустикалық ұяшықтың құрылымы мен өнімділігін оңтайландыру тиісті дабылдың тиімділігін анықтауда маңызды рөл атқарады. Мақала авторлары қатты кристалдарға арналған фотоакустикалық дабылдың пайда болуының теориялық аспектілерін ұсынған. Қатты кристалды қысым флактуациялары үшін өрнекті алған кезде, дабыл/шу арақатынасын жақсарту үшін фотоакустикалық жасушаның цилиндрлік құрылымына артықшылық беріледі. Басқа факторларды талдаумен қатар, фотоакустикалық ұяшықтағы газ шығаратын қысымның ауытқуы математикалық түрде анықталады.

Кілт сөздер: фотоакустикалық дабыл, қатты кристалл, энергияны беру, жарық пен заттың өзара әрекеттесуі, сәулеленбеген қозуды өшіру, фотоакустикалық ұяшық, фотоакустикалық түрлендіргіштер.

А.П. Сароде, О.Х. Махаджан

Теоретические аспекты генерации фотоакустических сигналов с твердыми кристаллами

Сегодня методы неразрушающего анализа играют важную роль в промышленном применении, в научных, а также технологических исследованиях. Фотоакустический метод является одним из таких неразрушающих методов, при котором генерация акустических волн происходит за счет поглощения модулированного падающего излучения. Фотоакустический сигнал является основой для фотоакустических исследований. Генерация фотоакустического сигнала связана с природой ячейки, используемой для исследования. Хотя многие исследователи сообщают о различных объяснениях генерации сигналов при фотоакустическом взаимодействии, некоторые аспекты еще предстоит детально изучить. При исследовании твердого кристалла в фотоакустике для анализа генерации фотоакустического сигнала учитываются такие факторы, как режим работы, схема возбуждения, форма ячейки и колебания давления в ячейке. Кроме того, оптимизация конструкции и производительности фотоакустической ячейки играет важную роль в определении эффективности генерации соответствующего сигнала. Авторами статьи представлены теоретические аспекты генерации фотоакустического сигнала для твердых кристаллов. При получении выражения для флуктуаций давления с твердым кристаллом предпочтительна цилиндрическая конфигурация фотоакустической ячейки, чтобы получить лучшее соотношение «сигнал/шум». Наряду с анализом других факторов, математически определяются колебания давления, создаваемые заключенным газом в фотоакустической ячейке.

Ключевые слова: фотоакустический сигнал, твердый кристалл, передача энергии, взаимодействие света и вещества, безызлучательное отключение возбуждения, фотоакустическая ячейка, фотоакустические преобразователи.

References

1 Rosencwaig, A. & Gersho, A. (1976). Theory of the photoacoustic effect with solids. *Journal of Applied Physics, 47,* 64–68.

2 West, G., Barrett, J.J., Siebert, D.R. & Reddy, K.V. (1983). Photoacoustic Spectroscopy. *Review of Scientific Instruments, 54:7,* 797–817.

3 McDonald, F.A., & Wetsel, G.C.Jr.(1978). Generalized Theory of the Photoacoustic Effect. *Journal of Applied Physics, 49:4,* 2313–2322.

4 Sigrist, M.W. (1999). Photoacoustic spectroscopy, method and instrumentation. *Encyclopedia of spectroscopy and spectrometry. Vol 3,* 1810–1812.

5 Silfvast, W.T. (2004). *Laser Fundamentals,* Cambridge University Press, Cambridge.

6 Lima, C.A.S., Miranda, L.C.M., & Santos, R. (1981). Sample gas thermal contact resistance and the photoacoustic signal generation. *Journal of Applied Physics. 52,* 137–140.

7 Kuo, C.Y., Vieira, M.M.F. & Patel, C.K.N. (1984). Transient optoacoustic pulse generation and detection. *Journal of Applied Physics. 55,* 3333–3336.

8 Schurig, D.A., Klunder, G.L., Shannon, M.A. & Russo, R.E. (1992). Signal analysis of transients in pulsed photoacoustic spectrpscopy. *Review of Scientific Instruments, 64(2),* 363–373.

9 Hoelen, C.G.A., & de Mul, F. F. M. (1999). A new theoretical approach to photoacoustic signal generation. *Journal of the Acoustical Society of America, 106*, 695–706.

10 Simandoux, O., Prost, A., Gateau, J., & Bossy, E. (2015). Influence of nanoscale temperature rises on photoacoustic generation: Discrimination between optical absorbers based on thermal nonlinearity at high frequency. Photoacoustics, 3(1), 20–25. doi:10.1016/j.pacs.2014.12.002

11 Zhu, Z., Luo, J., Liu, J. & Fang, Y. (2020). Effects of pressure and noise on the stability of photoacoustic signals of trace gas components. International Journal of Agricultural and Biological Engineering, 13(5), 187 — 193.

12 Sarode A.P., & Mahajan O.H. (2020). Theoretical aspects of transient temperature on cubic crystal surface in a photoacoustic effect. *Bulletin of the Karaganda University – Physics, 2020–99(3),* 73–79. DOI 10.31489/2021PH4/10.31489/2020Ph3/73–79.

13 Sarode, A.P., & Mahajan, O.H. (2021). Displacement fields of a Cuboid crystal in a Photoacoustic Cell: Mathematical aspects. *Bulletin of the Karaganda University – Physics, 1(101),* 6–11. DOI 10.31489/2021PH4/10.31489/2021Ph1/6–11.

14 Mandelis, A. (1987). Photoacoustic and Thermal Wave Phenomena in Semiconductors, North-Holland, Amsterdam.

15 Malin´ski M. (2005). Determination of air-tightness of the packaging of electronic devices by the thermoacoustic method. *Arch. Acoust., 30(3),* 345–355.

16 Wilcken, K. & Kauppinen, J. (2003). Optimization of a Microphone for Photoacoustic Spectroscopy. *Applied Spectroscopy, 59:9,* 1087–1092.

17 Chrobak, L. & Malinski, M. (2013). Design and optimization of the photoacoustic cell for nondestructive photoacoustic spectroscopy, *Nondestructive Testing and Evaluation, 28, No. 1,* 17–27. http://dx.doi.org/10.1080/10589759.2012.667408

18 Raghu, O. & Philip, J. (2003). A dual channel photoacoustic cell for imaging experiments on solid samples. *J. Instrum. Soc. India, 33(3),* 155–158.

19 Chrobak L. & Malinski M. (2009). Transmission and absorption based photoacoustic methods of determination of the optical absorption spectra of Si samples — comparison, *Solid State Commun., 149,* 1600–1604.

20 Rabasovic, M.D., Nikolic, J.D., Markushev, D.D., & Jovanovic-Kurepa J. (2008). Pulsed photoacoustic gas cell design for low pressure studies, *Optical. Materials, 30,* 1197–1200.

21 Jorge M.P.P.M., Mendes Filho J., Oliveira A.C., Braga A.J.P, Cesar C.L., Morato S.P., Vieira Jr, N.D. & Vieira M.M.F. (1999). *Resonant photoacoustic cell for low temperature measurements, Cryogenics, 39,* 193–195.

22 Yehya, F. & Chaudhary, A.K. (2011). Designing and modeling of efficient resonant photoacoustic sensors for spectroscopic applications. *Journal of Modern Physics. 2,* 200–209.

23 Landau, L. D. & Lifshitz, E. M. (1987). *Fluid Mechanics,* Pergamon Press, Oxford.

DOI 10.31489/2021PH4/68-77

UDC 62-531.7; 62-868; 67-05; 66-041

A. Nizhegorodov[1], A. Gavrilin[2], B. Moyzes[2*], K. Kuvshinov[2]

[1]Irkutsk National Research Technical University;
[2]National Research Tomsk Polytechnic University, Tomsk, Russia
([*]E-mail: nastromo_irkutsk@mail.ru)

Thermal Unit with Controlled Distribution of Flow Speeds of Processed Raw Materials in Zones of Electrified Modules

The article reviews the possibility of thermal treatment of vermiculite concentrates in thermal units of the modular-launch type after the defects of the units appeared during operation were fixed. It was observed that the temperatures of the electric heaters and the refractory surface of the firing modules distribute unevenly horizontally: the temperatures decreased significantly from center to periphery. This feature showed a technical solution — the division of the total flow of the expanded vermiculite into local and controlled flows between the thermal zones of the furnace modules taking into account their temperatures. The required time for particles movement in each thermal zone was determined, as well as average local speeds of their movement in the indicated zones were by comparing the thermal capacities of local vermiculate flows. The calculations of local flow rates were carried out and the total productivity of the modernized furnace was determined. The productivity of modernized furnace is 24% higher than the prototype furnace. It is shown that with an increase in productivity but equal to electricity consumption, the specific energy consumption of firing processes decreases by the same 24%. It makes the furnace more perfect and competitive.

Keywords: electric modular–launch furnace, firing module, non-uniform temperature distribution, temperature zones, accelerating tray, heaters, heat power, average local speeds, local productivity, total productivity.

Introduction

The research in the field of technologies for the production and use of expanded vermiculite has been conducted since the 30s years of the last century. This indicates the relevance of this issue and the importance of the product [1–11]. Electric furnaces for vermiculite firing, which will be reviewed in the article [12], were developed in the early 2000s as an alternative to fired furnaces operating on hydrocarbon fuel [9].

The expanded particles' streams in such furnace units have been uncontrollable till the present time and their flow was determined by the action of the gravity forces of the particles. This is their obvious disadvantage.

Even in the very first modular-launch furnaces (2003–2005), it was noticed and experimentally confirmed that the temperatures of suspended heating elements and refractory surfaces of firing modules were distributed non-uniformly.

Temperature measurements in different areas showed that in the central zones of the modules, the temperatures of the refractory bases are significantly higher than in the side zones. During the heat treatment of vermiculite at the furnace exit in the central zone, the end product was completely expanded, but overheated and partially burnt, and in the edge zones it remained under-expanded. This feature illustrated a technical solution – to separate the flow of expanded vermiculite into local flows in thermal zones, taking into account their temperatures, and to develop a system for controlling local flows.

The purpose of the research is to increase the efficiency of the thermal unit by means of the rational distribution of local flows of heat-treated raw materials along the width of the firing modules without the increasing of its electrical power.

Experimental

Consideration of the furnace design and operation.

Vermiculite concentrate is supplied to the furnace by a dispenser equipped with a hopper 1, a drive 2, a drum 3, and an inclined tray 4 by length l_0. The raw material through the inclined tray 4 is poured onto the accelerating tray 5 of the upper module 6. Then the raw material goes to the firing space under the cover 7, where the electric heater 8 is fixed. It is held by the hooks 9 and the fixing heads 10 (Figure 1). Then vermiculite is poured onto the second accelerating tray 11 of the middle module 12 and then onto the tray 13 of the lower module 14. The finished product comes out from the tray 13 of the lower module 14. The firing space 15 of each module is formed by a refractory surface 16 made of refractory bricks, by the lower part of the cover 7 and by side walls (not shown in Figure 1).

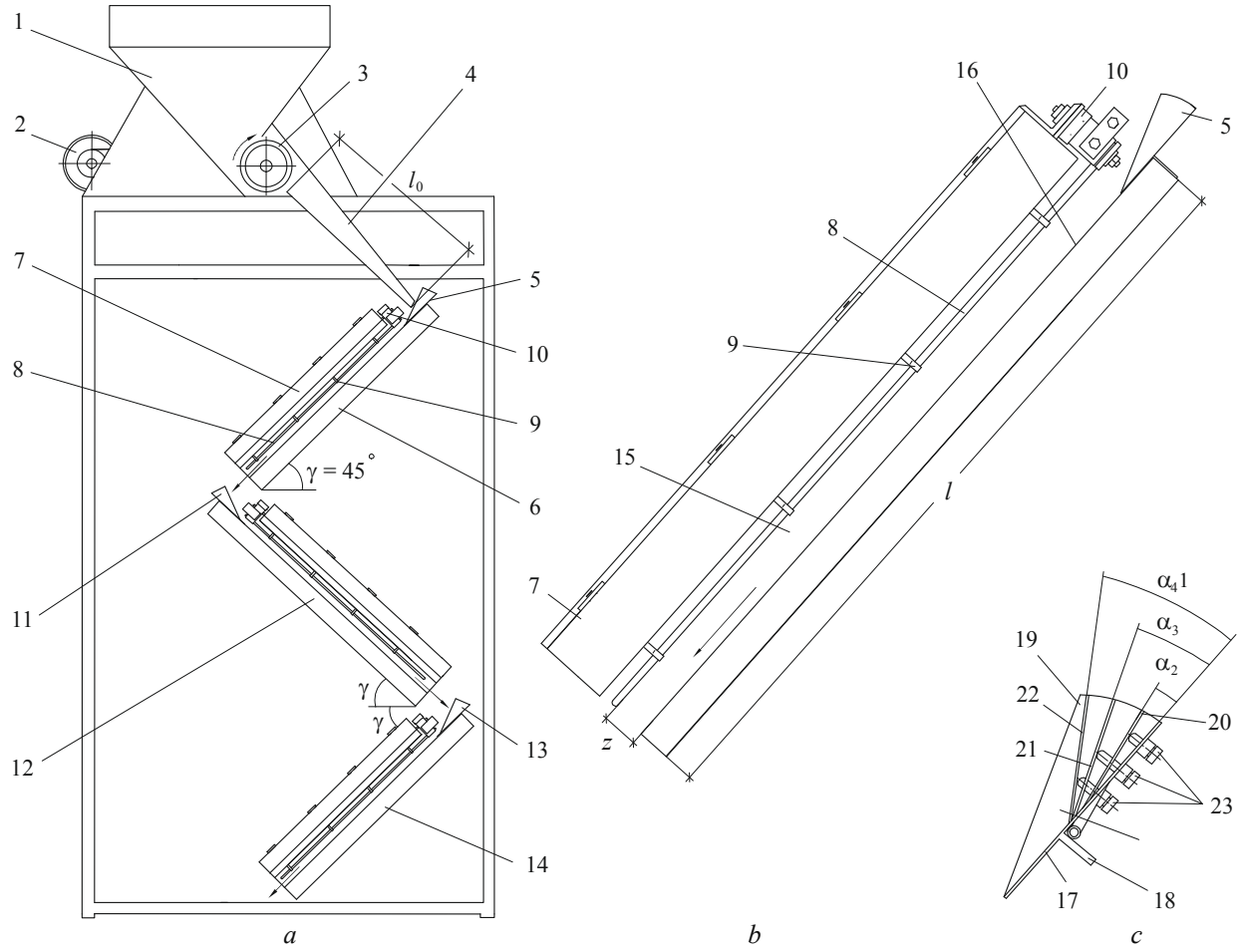

Figure 1. Modular launch furnace:
a – modular launch furnace; *b* – firing module; *c* – accelerating tray

There are the accelerating trays (Figure 1, 2) in the upper part of each module. They consist of a base plate 17, a stop 18 with side walls 19 and a set of hinged plates 20–22. The inclination angles of hinged plates α_2, α_3, and α_4 can be adjusted using screws 23.

The dispenser drum is made with longitudinal grooves 24–26, step-variable in depth (Figure 2). In this case, the greatest depth is at the grooves 24 located above the central plate 22 of the accelerating tray. There are adjacent grooves 25 above the plates 21. They have a shallower depth. The further from the center the grooves are located, the shallower their depth:

$$t_4 > t_3 > t_2 > t_1.$$

The number of plates of the accelerating tray and the number of grooves may be different, depending on the width of the refractory surface of module B and the temperature distribution on the electric heaters. Moreover, the length of the grooves on the drum b_1, b_2, b_3, and b_4 and the width of the plates of the accelerating tray can also be different.

Vermiculite concentrate particles falling on plate 22 in Zone 4 (Figure 2) acquire the maximum initial velocity v_{04x} due to the larger angle of its inclination α_4. In this regard, their average local velocity in this zone will be greater than in the side zones 1, where the plates have a zero inclination angle. If the speed of particles is maximum here, then the time of their movement is minimal, and the local productivity is proportional to the speed and is maximum in comparison with other zones. In Zone 4 the electric heaters are hottest.

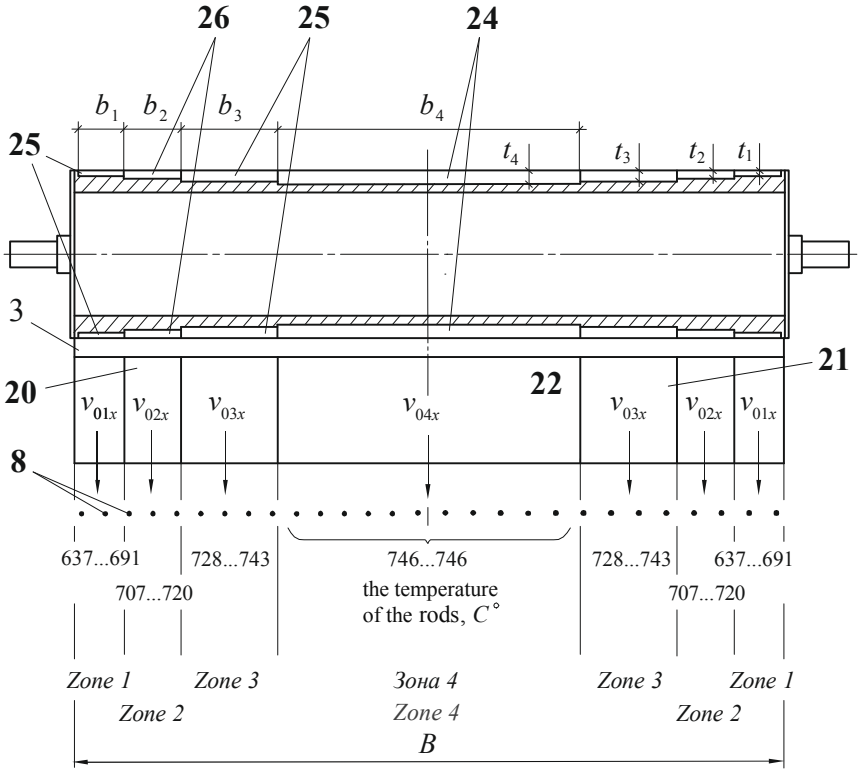

Figure 2. Dispenser drum, accelerating tray and electric heater rods with indication of temperature zones

In Zone 3, the temperature of the electric heaters is lower, therefore, the concentrate particles falling on plates 21 (Figure 2) should receive a lower initial velocity v_{03x}. It is due to their smaller tilt angle α_3. The local productivity in these zones is proportional to the average local speed of the particles, and the particles motion time is slightly longer than in the central zone. The same applies to Zone 2 and 1: the average local particle speeds from the central to the side zones should become less and less, as the temperatures of the heaters decrease from the center to the periphery.

Adjusting screws 23 (Figure 1) allow to change the initial and the average local speeds when one size group of vermiculite concentrate change into another, since larger expanded grains move at higher speeds than small ones (proofed by the tests).

Due to the accelerating trays such distribution of average local speeds over the temperature zones is created, that in each zone vermiculite will consume the necessary amount of thermal energy during the corresponding time and, at the same time, the whole will be fully expanded. If this distribution is carried out correctly, the productivity of the furnace will increase with constant energy consumption.

The initial velocities v_{01x}, v_{02x}, v_{03x}, and v_{04x} determine the average particles local speeds in the corresponding zones and depend on the inclination of the accelerating plates. However, they also depend on the speed of particles falling onto these plates. Figure 3 demonstrates the change in the vectors of the initial speeds at different angles of inclination. There is a vector v_f denoting the falling speed in each triangle of speeds. If the falling speed for the places of junction of modules 6 and 12 and modules 12 and 14 (Figure 1) is determined by their length l, then it is necessary that the speed v_f at the place of junction of the tray 5 and the upper module 6 is the same.

The joint operation of the dispenser and the upper module of the furnace, which provides the balance of the supplied concentrate and the furnace productivity, will be discussed below. Let us consider the issue of the correct distribution of local speeds over the module zones.

Local speeds distribution

The interaction between the thermal energy absorbed by vermiculite, leading to its structural change, the loss of hydrated water and a multiple decrease in density, and radiant energy falling on the vermiculite grains from the surfaces of the electric heater rods was discussed in the research [13].

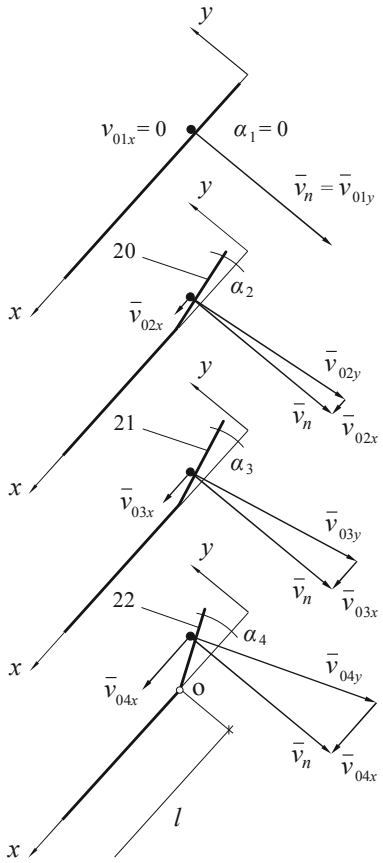

Figure 3. Speeds triangles on the plates of the accelerating tray at different values of the inclination angle of its plates

Let us use the obtained dependence for the heat power flux θ absorbed by the expanded material (W):

$$\theta = 0.667 \cdot \alpha \cdot \sigma \cdot T^4 \cdot s \cdot \varepsilon \cdot (1 + \rho \cdot \varphi_{12})\left(2 \cdot \varphi_{1v} + \varphi_{2v}\right), \quad (1)$$

where α – is the capacity of vermiculite absorbability (0.768); σ – Stefan-Boltzmann constant, 5.67, W/m^2 K; T is the surface temperature of the heater rods, K; s is the area of all surfaces of the heater rods in three furnace modules, m^2; ε – the nichrome blackness degree (0.96); ρ is the nichrome reflectivity (0.04); φ_{12}– is the angular coefficient of heat fluxes from one rod to another, φ_{1v} is the angular coefficient for rods located on both sides symmetrically relative to the vermiculite grain; φ_{2v} – is the angular coefficient for rods located on both sides with relative to the vermiculite grain which is in contact with one of the rods [13].

The above formula (1) does not take into account the effect of reflected radiant fluxes from the refractory base of the module and its cover. The same Ref. [13] states that it was proofed by the tests that the thermal power of the reflected fluxes is 10...12% of the heating power of furnace systems.

The absorbed thermal power θ provides complete expanding of the material and it is unchanged for any thermal zone of the module. Therefore, we can write the equality valid for the i-th number of zones (J):

$$E = \theta_1 \cdot t_1 = \theta_2 \cdot t_2 = \theta_3 \cdot t_3 = \theta_4 \cdot t_4 = \theta_i \cdot t_i, \quad (2)$$

where E is the energy of vermiculite heat absorption, sufficient for full expanding, J; t_1 is the average local time of vermiculite flow movement in Zone 1 (Figure 2), equals to the time of firing in the furnace, adopted

as an analogue [14–16]; t_2, t_3, t_4, and t_i are the average local times of vermiculite flow movement in other thermal zones, *s*.

To find the value of the vermiculite time of movement in the zones, it is not required to determine the energy *E*. We use the ratios, in this case for four zones, based on formula (2):

$$t_2 = \frac{\theta_1 \cdot t_1}{\theta_2 \cdot t_2},\ t_3 = \frac{\theta_1 \cdot t_1}{\theta_3 \cdot t_3},\ t_4 = \frac{\theta_1 \cdot t_1}{\theta_4 \cdot t_4}. \quad (3)$$

The average values of rods of electric heaters heating temperatures by zones (Figure 2):

- in Zone 4 – 1030 °K;
- in Zone 3 – 1019 °K;
- in Zone 2 – 986 °K;
- in Zone 1 – 940 °K.

Since in formula (1) only temperature changes for each zone, then the relations (3) will take the form (s):

$$t_2 = \frac{T_1^4}{T_2^4} t_1,\ t_3 = \frac{T_1^4}{T_3^4} t_1,\ t_4 = \frac{T_1^4}{T_4^4} t_1, \quad (4)$$

where T_1, T_2, T_3 and T_4 are the average temperatures of the heater rods in the corresponding zones.

Taking the time $t_1 = 0.91$ s and the average speed $v_m = 1.05$ m / s with a module length of 0.95 m for the adopted analogue – a prototype furnace [15], from relations (4) we obtain the time of vermiculite movement in thermal zones (Figure 2) (s):

$$t_2 = 0.82 \cdot t_1,\ t_3 = 0.75 \cdot t_1,\ t_4 = 0.72 \cdot t_1.$$

It follows from the found relationships that the time of vermiculite particles movement through Zones 2, 3, and 4 in the furnace modules should decrease by 17.9%, 24.9%, and 27.8%, respectively, in comparison with the first zone.

The average time of vermiculite being in a prototype furnace (furnace time constant) is 2.74 s [16]. The indicated values $t_1 = 0.91$ s and $v_m = 1.05$ m / s correspond to Zone 1 of the considered furnace (Figure 2), and for Zones 2, 3, and 4 the average time of local flows should be:

$$t_2 = 0.747 \text{ s},\ t_3 = 0.683 \text{ s},\ t_4 = 0.657 \text{ s}.$$

The l/t_i ratio determines the corresponding average local flow rates of vermiculite in thermal zones:

$$v_{m2} = 1.27 \text{ m/s},\ v_{m3} = 1.39 \text{ m/s и } v_{m4} = 1.45 \text{ m/s}.$$

It is necessary to find such values of the initial particles' speeds on the plates of the accelerating tray, at which the required average speeds will be achieved. Taking into account that gravity and friction forces act on each particle, and neglecting the air resistance, we write the differential equation:

$$m\frac{d^2x}{dt^2} = m \cdot g \cdot \sin\gamma - m \cdot g \cdot f \cdot \cos\gamma, \quad (5)$$

where γ is the inclination angle of the modules (Figure 1); *f* is reduced coefficient of sliding–rolling friction, determined by the tests, $f = 0.51$ [16]; *m* is the particle mass.

Separating the variables in equation (5), we get (m/s):

$$v_x = g\left(\sin\gamma - f\cos\gamma\right)t + v_{0x}, \quad (6)$$

where v_x is the final particle velocity in the zone (the same as the falling velocity v_f) corresponding to its time (t_1, t_2, t_3 and t_4), v_{0x} is the initial particle velocity on the corresponding plates of the accelerating tray (Figure 3).

Let us determine the final falling velocity for the first zone using the formula (6), taking into account the fact that $v_{01x} = 0$ m/s:

$$v_f = 9.81 \cdot (0.707 - 0.51 \cdot 0.707) \cdot 0.91 + 0 = 3.1.$$

Setting the same falling velocity (3.1 m/s) for all other zones, we determine the initial local velocities using expression (6) (m/s):

$$v_{0x} = v_n - g\left(\sin\gamma - f\cos\gamma\right)t. \quad (7)$$

Substituting the movement time in the zones (t_2 = 0.747 s, t_3 = 0.683 s, t_4 = 0.657 s) into formula (7), we determine the initial velocities, (m/s):

- in Zone 2 – v_{02x} = 0.56;
- in Zone 3 – v_{03x} = 0.78;
- in Zone 4 – v_{04x} = 0.87.

In accordance with the vector diagrams (Figure 3), we obtain the relations that determine the angles sines:

$$\sin\alpha_2 = \frac{v_{02x}}{v_f} = \frac{0.56}{3.1} = 0.18,\ \sin\alpha_3 = \frac{v_{03x}}{v_f} = \frac{0.78}{3.1} = 0.26,\ \text{и}\ \sin\alpha_4 = \frac{v_{04x}}{v_f} = \frac{0.87}{3.1} = 0.28.$$

The angles themselves at which the required initial speeds and average local speeds of vermiculite particles in the thermal zones of the furnace modules will be provided equal: α_2 = 10.5 °, α_3 = 15 ° and α_4 = 16.5 °.

As already noted, when processing other size of groups of vermiculite concentrates, it is necessary to change the average local rates. For this purpose, the adjusting screws 21 are provided in the accelerating trays of the modules. By using the adjusting screws, the tilt angles of the plates 18–20 can be changed (Figure 1). When firing smaller concentrates, the time of vermiculite passage should decrease, and therefore, it is necessary to increase the angles α_2, α_3 and α_4 in order to increase the average local speeds in the corresponding thermal zones.

Figure 4 illustrates a nomogram for determining the inclination angles of the plates of the accelerating tray at a given local speed.

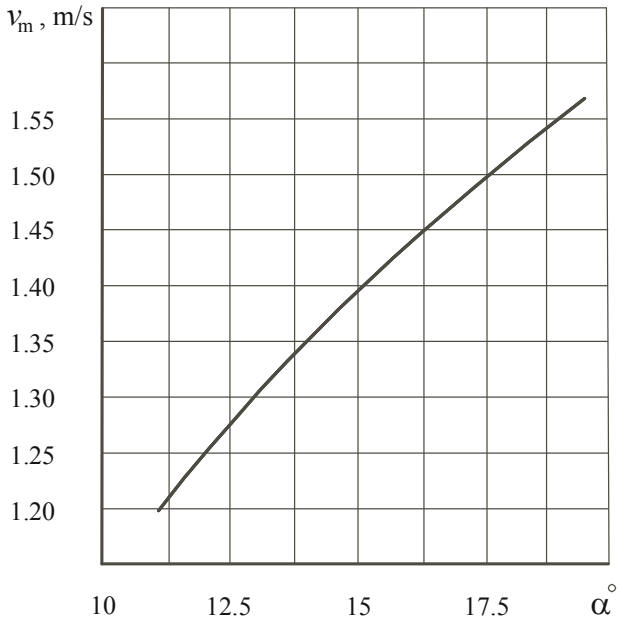

Figure 4. Nomogram for determining the inclination angles of the plates of the accelerating tray at a given average local speed in the thermal zones of the module

Joint operation of the dispenser and furnace modules

To provide a balance between the vermiculite concentrate amount supplied by the dispenser and the amount of expanded material passing through the furnace modules, two conditions must be met:

- the rate of concentrate particles falling out from the inclined tray 4 (Figure 1) should provide the same initial speeds in the thermal zones on the accelerating tray of the upper module, as in the accelerating trays 11 and 13 of the middle and lower furnace modules;

- the capacity of the dispenser for concentrate must correspond to the full capacity of the furnace for expanded material, taking into account the expansion coefficient.

To meet the first condition, it is necessary to find the length value of the inclined tray l_0, at which the rate of the concentrate particles falling out of it will provide the same initial speeds on the accelerating tray of the upper module as on the accelerating trays 11 and 13 of the middle and lower furnace modules. In this case, the friction coefficient f_0 in equation (5) will have a value of 0.68 [15], since flat particles of vermiculite mica slide over steel and there is no rolling, as on refractory surfaces of modules.

From expression (6), which in this case will have the form:

$$v_{\text{f}} = g\left(\sin\gamma - f_0\cos\gamma\right)t + v_{0x},$$

Let us find the time t required for the particles to reach the velocity v_{f} = 3.1 m/s at the moment of contact with the plates of the accelerating tray 5 (Figure 1) at zero initial velocity v_{0x}:

$$t = \frac{v_n}{g\left(\sin\gamma - f_0\cos\gamma\right)} = 1.4 \text{ m/s}. \quad (8)$$

To find the length of the dispenser tray 4 (Figure 1), we fulfill the second integration of equation (5):

$$l_0 = \frac{1}{2}g\left(\sin\gamma - f_0\cos\gamma\right)t^2 + v_{\text{f}}\cdot t, \quad (9)$$

where t is the convergence time of particles along the tray, determined by expression (8); γ is the inclination angle of the tray to the horizon, 45 °.

To supply the concentrate by the dispenser to the furnace in accordance with the capacity of the furnace for expanded material, we will use the formula [17–22]:

$$P_G = \frac{P_V}{k},$$

where k is the expanding coefficient depending on the size group of the —vermiculite concentrate and the natural hydration of the mica (Figure 5).

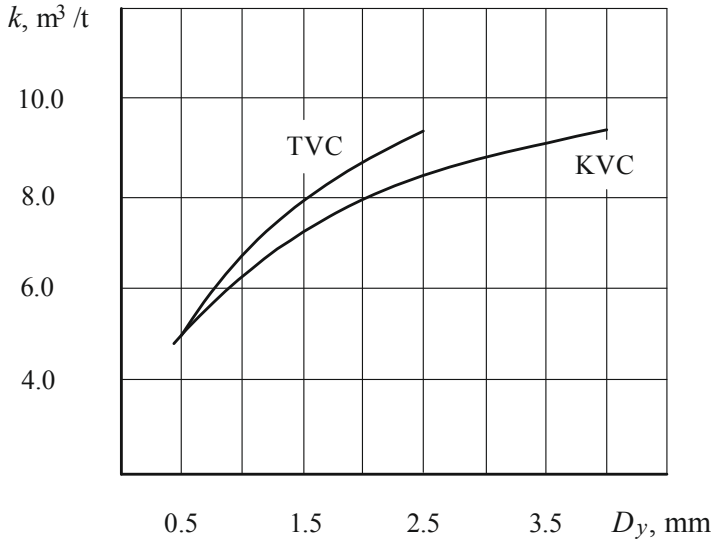

Figure 5. The dependence of the expanding coefficient on the nominal concentrate particle diameter for two fields – Kovdorskoye (KVC) and Tatarskoye (TVC)

Conclusions

Determination of the local capacities and the total furnace productivity.

With the width of the modules B = 95 cm, as in the prototype furnace [15], the productivity of the furnace without accelerating trays 5 (Figure 1) on vermiculite concentrate, for example, grade KBK-4 (4 is the

conventional average particle diameter), is equal to 0.75 m^3/hour. Then the hourly productivity, reduced to the unit of width, will be equal to, (m^3/cm·hour):

$$P_{\text{h}} = \frac{0.75}{95} = 0.0079.$$

Since the local average speeds in zones No. 2, No. 3, and No. 4 the increase relative to the first zone will be:

- at $\frac{1.27}{1.05} = 1.21$ times or by 21 %;
- at $\frac{1.39}{1.05} = 1.32$ times or by 32 %;
- at $\frac{1.45}{1.05} = 1.38$ times or by 38 %;

then the local capacities, taking into account the width of the zones B_4 = 21 cm, B_3= 15 cm, B_2 = 12 cm and B_1 = 10 cm (Figure 2) will be equal to, ($м^3$/h):

- in the fourth zone: $P_4 = 0.0079 \cdot 21 \cdot 1.38 = 0.229$;
- in two third of zones: $P_3 = 2 \cdot 0.0079 \cdot 15 \cdot 1.32 = 0.313$;
- in two second zones: $P_2 = 2 \cdot 0.0079 \cdot 12 \cdot 1.21 = 0.229$;
- in two first zones: $P_1 = 2 \cdot 0.0079 \cdot 10 \cdot 1.0 = 0.16$.

The total furnace productivity will be, (m^3/h):

$$P = 0.229 + 0.313 + 0.229 + 0.16 = 0.931.$$

The increased productivity of the modular–launch furnace due to the distribution of the speeds of the vermiculite flows movement over the thermal zones of the modules is equal to 0.931 m^3/h, which is 24% more than that of the experimental industrial furnace taken as a prototype. Moreover, the energy consumption does not grow and the specific energy consumption of the process increases by the same 24%.

References

1 Kogal J.E. Industrial minerals & rocks: commodities, markets and uses / J.E. Kogal, N.C. Trivedi, J.M. Barker, T.S. Krukowski. — Littleton: Society for Mining, Metallurgy, and Exploration Inc., 2009. — P. 1565.

2 Rashad A.M. Vermiculite as a construction material — A short guide for Civil Engineer / A.M. Rashad // Construction and Building Materials. — 2016. — Vol. 125. — P. 53–62.

3 Fan Ding. Tuning wettability by controlling the layer charge and structure of organo-vermiculites / Manglai Gao, Jie Wang, Tao Shen, Weili Zang // Journal Industrial and Engineering Chemistry. — 2018 — Vol. 57 — P. 304–312.

4 Kariya J. Development of thermal storage material using vermiculite and calcium hydroxide / J. Kariya, J. Ryu, Y. Kato // Applied Thermal Engineering. — 2016. — Vol. 94. — P. 186–192.

5 Figueiredo S. The influence of acid treatments over vermiculite-based material as adsorbent for cationic textile dyestuffs / S. Figueiredo, W. Stawinski, O. Freitas, L. Chmielarz // Chemosphere. — 2016. — Vol. 153. — P. 115–129.

6 Kim Hung Mo. Incorporation of expanded vermiculite lightweight aggregate in cement mortar / Kim Hung Mo, Hong Jie Lee, Michael Yong Jing Liu, Tung-Chai Ling // Construction and Building Materials. — 2018. — Vol. 179. — P. 302–306.

7 Sevim İşçi. Intercalation of vermiculite in presence of surfactants / Sevim İşçi // Applied Clay Science. — 2017. — Vol. 146. — P. 713.

8 Raupach M. Polarized infrared study of anilinium-vermiculite intercalate. I. Spectra and models / M. Raupach, L.J. Janik // Journal of Colloid and Interface Science. — 1988. — Vol. 121. — P. 449–465.

9 Zvezdin A.V. Considering adaptation of electrical ovens with unit-type releasing to peculiarities of thermal energization of mineral raw materials / A.V. Zvezdin, T.B. Bryanskikh // IOP Conf. Series: Materials Science and Engineering. — 2017. — Vol. 168 (1). — 012003.

10 Попов Н.А. Производство и применение вермикулита / Н.А. Попов. — М.: Стройиздат, 1964. — 128 с.

11 Hombostel C. Construction Materials: Types, Uses, and Applications / C. Hombostel. — New York: John Wiley & Sons, Inc., 1991. — 878 p.

12 Nizhegorodov A.I. Theory and practical use of modular-pouring electric furnaces for firing vermiculite / A.I. Nizhegorodov // Refractories and Industrial Ceramics. — 2015. — Vol. 56 (4). — P. 361–365. doi: https://doi.org/10.1007/s11148–015–9848–7.

13 Nizhegorodov A. The development of baking technology for bulk materials based on the use of alternative electric furnace / A. Nizhegorodov, A. Gavrilin, B. Moyzes, K. Kuvshinov // Bulletin of the Karaganda University – Physics — 2020. — Vol. 2 (98). — P. 93–100. doi: 10.31489/2020Ph2/93–100.

14 Chen L. Preparation and characterization of the eco-friendly chitosan/vermiculite biocomposite with excellent removal capacity for cadmium and lead / L. Chen, Wu P. Pingxiao, M. Chen, T. Liu // Applied Clay Science. — 2018. — Vol. 159. — P. 74–82.

15 Нижегородов А.И. Экспериментальное определение эффективности тренировок некоторых потенциально термоактивных минералов / А.И. Нижегородов // Строительные материалы. — 2016. — Т. 11. — С. 63–67.

16 Lozano-Lunar A. Safe use of electric arc furnace dust as secondary raw material in self-compacting mortars production / A. Lozano-Lunar, P.R. da Silva, J. de Brito, J.M.F. Rodriguez // Journal of Cleaner Production. — 2019. — Vol. 211. — P. 1375–1388.

17 Santamaria A. Dimensional stability of electric arc furnace slag in civil engineering applications / A. Santamaria, F. Faleschini, G. Giacomello, K. Brunelli, M. Pasetto // Journal of Cleaner Production. — 2018. — Vol. 205. — P. 599–609.

18 Xu W. Application of multi-model switching predictive functional control on the temperature system of an electric heating furnace / W. Xu, J. Zhang, R. Zhang // ISA Transaction. — 2017. — Vol. 68. — P. 287–292.

19 Balima F. Effect of the temperature on the structural and textural properties of a compressed K-vermiculite / F. Balima, L. Laurence Reinert, N. An-Ngoc, S. Le Floch // Chemical Engineering Science. — 2015. — Vol. 134. — P. 555–562.

20 Jinpeng Feng. Heating temperature effect on the hygroscopicity of expanded vermiculite / Jinpeng Feng, Meng Liu, Wei Mo, Xiujuan Su // Ceramics International. — 2021. — Vol. 47 (18). — P. 25373–25380.

21 Fisher R. Hydration kinetics of K_2CO_3, $MgCl_2$ and vermiculite-based composites in view of low-temperature thermochemical energy storage / R. Fisher, Y. Ding, A. Sciacovelli // Journal of Energy Storage. — 2021. — Vol. 38. — 102561.

22 Naveenkumar K. Experimental investigation flexural behavior of reinforced concrete beam with partial replacement of vermiculite / K. Naveenkumar, P.A. Suriya, R. Divahar, S.P. Sangeetha, M. Jayakumar // Materials Today: Proceedings. — 2021. — Vol. 46 (12). — P. 5885–5888.

А. Нижегородов, А. Гаврилин, Б. Мойзес, К. Кувшинов

Электрлендірілген модульдер аймақтарында өңделетін шикізат ағыны жылдамдығының таралуын реттейтін жылу агрегаты

Ісінген вермикулитті өндіру және пайдалану технологиялары саласындағы зерттеулер өзекті болып табылады. Көмірсутекті отынмен жұмыс істейтін отты пештерге балама ретінде вермикулитті жағуға арналған электр пештерін әзірлеу белсенді жүргізілуде. Бұл пештерде ісінген бөлшектердің ағындары бақыланбайтын және бөлшектердің ауырлық күшінің әсерімен анықталады. Мақалада пайдалану кезінде пайда болған агрегаттардың кемшіліктерін жойғаннан кейін модульдік-іске қосу түріндегі жылу агрегаттарында вермикулит концентраттарын термиялық өңдеу мүмкіндігі қарастырылған. Электр жылытқыштар мен күйдіру модульдерінің отқа төзімді бетінің температурасы көлденеңінен біркелкі бөлінбейтіні байқалды: температура орталықтан периферияға дейін айтарлықтай төмендейді. Бұл ерекшелік техникалық шешімді көрсетті – ісінген вермикулиттің жалпы ағынын пеш модульдерінің жылу аймақтары арасындағы жергілікті және бақыланатын ағындарға олардың температурасын ескере отырып бөлу. Жергілікті вермикулит ағындарының жылу сыйымдылығын салыстыру арқылы әр жылу аймағындағы бөлшектердің қажетті қозғалыс уақыты, сондай-ақ көрсетілген аймақтардағы олардың қозғалысының орташа жергілікті жылдамдығы белгілі. Жергілікті шығындар есебі жүргізілді және жаңғыртылған пештің жалпы өнімділігі анықталды. Жаңартылған пештің өнімділігі тәжірибелі пешке қарағанда 24 % жоғары. Өнімділіктің жоғарылауымен, бірақ электр энергиясын тұтынумен бірдей, күйдіру процестерінің энергия шығыны 24 %-ға төмендегені көрсетілді. Бұл пешті жетілдіреді және бәсекегеқабілетті етеді. Мақалада зерттеу процесін суреттейтін және осы ғылыми жұмыста қойылған мақсатқа қол жеткізуді растайтын диаграммалар келтірілген.

Кілт сөздер: электр модульдік-іске қосу пеші, күйдіру модулі, температураның біркелкі бөлінбеуі, температуралық аймақтар, үдеткіш науа, жылытқыштар, жылу қуаты, орташа жергілікті жылдамдық, жергілікті өнімділік, жалпы өнімділік.

А. Нижегородов, А. Гаврилин, Б. Мойзес, К. Кувшинов

Тепловой агрегат с регулируемым распределением скоростей потока обрабатываемого сырья в зонах электрифицированных модулей

Исследования в области технологий производства и использования вспученного вермикулита являются актуальными. Активно ведутся разработки электрических печей для обжига вермикулита, как альтернатива пламенным печам, работающим на углеводородном топливе. В данных печах потоки расширенных частиц неконтролируемы и определяются действием сил тяжести частиц. В статье рассмотрена возможность термической обработки вермикулитовых концентратов в тепловых агрегатах модульно-пускового типа после устранения недостатков агрегатов, возникших в процессе эксплуатации. Было замечено, что температура электронагревателей и огнеупорной поверхности обжиговых

модулей распределяется неравномерно по горизонтали: температуры значительно снижаются от центра к периферии. Эта особенность показала техническое решение – разделение общего потока вспученного вермикулита на локальные и контролируемые потоки между тепловыми зонами модулей печи с учетом их температур. Путем сравнения теплоемкостей локальных потоков вермикулита определяли требуемое время движения частиц в каждой тепловой зоне, а также средние локальные скорости их движения в указанных зонах. Проведены расчеты локальных расходов, и определена общая производительность модернизированной печи. Производительность модернизированной печи на 24 % выше, чем у опытной печи. Показано, что при увеличении производительности, но равном потреблении электроэнергии, удельное энергопотребление процессов обжига уменьшается на те же 24 %. Это делает печь более совершенной и конкурентоспособной. В статье приведены диаграммы, иллюстрирующие процесс исследования и подтверждающие достижение цели, которая поставлена в данной научной работе.

Ключевые слова: электрическая модульно-пусковая печь, обжиговый модуль, неравномерное распределение температуры, температурные зоны, ускорительный лоток, нагреватели, тепловая мощность, средние локальные скорости, локальная производительность, общая производительность.

References

1 Kogal, J.E., Trivedi, N.C., Barker, J.M., & Krukowski, T.S. (2009). *Industrial minerals & rocks: commodities, markets and uses*. Littleton: Society for Mining, Metallurgy, and Exploration Inc.

2 Rashad, A.M. (2016). Vermiculite as a construction material — A short guide for Civil Engineer, *Construction and Building Materials, 125*, 53–62.

3 Fan Ding, Manglai Gao, Jie Wang, Tao Shen, & Weili Zang (2018). Tuning wettability by controlling the layer charge and structure of organo-vermiculites. *Journal Industrial and Engineering Chemistry, 57*, 304–312.

4 Kariya, J., Ryu, J., & Kato, Y. (2016). Development of thermal storage material using vermiculite and calcium hydroxide. *Applied Thermal Engineering, 94*, 186–192.

5 Figueiredo, S. et al. (2016). The influence of acid treatments over vermiculite-based material as adsorbent for cationic textile dyestuffs. *Chemosphere, 153*, 115–129.

6 Kim Hung Mo, Hong Jie Lee, Michael Yong Jing Liu, & Tung-Chai Ling. (2018). Incorporation of expanded vermiculite lightweight aggregate in cement mortar. *Construction and Building Materials, 179*, 302–306.

7 Sevim İşçi. (2017). Intercalation of vermiculite in presence of surfactants. *Applied Clay Science, 146,* 713.

8 Raupach, M. & Janik, L.J. (1988). Polarized infrared study of anilinium-vermiculite intercalate. I. Spectra and models. *Journal of Colloid and Interface Science, 121*, 449–465.

9 Zvezdin, A.V. & Bryanskikh, T.B. (2017). Considering adaptation of electrical ovens with unit-type releasing to peculiarities of thermal energization of mineral raw materials. *IOP Conf. Series: Materials Science and Engineering, 168(1)*, 012003.

10 Popov, N.A. (1964). *Proizvodstvo i primenenie vermikulita [Production and application of vermiculite]*. Moscow: Stroiizdat [in Russian].

11 Hombostel, C. (1991). *Construction Materials: Types, Uses, and Applications.* New York: John Wiley & Sons Inc.

12 Nizhegorodov, A.I. (2015). Theory and practical use of modular-pouring electric furnaces for firing vermiculite. *Refractories and Industrial Ceramics, 56 (4)*, 361–365. doi: https://doi.org/10.1007/s11148–015–9848–7.

13 Nizhegorodov A., Gavrilin A., Moyzes B., & Kuvshinov K. (2020). The development of baking technology for bulk materials based on the use of alternative electric furnace. *Bulletin of the Karaganda University – Physics*, *2 (98)*, 93–100. doi: 10.31489/2020Ph2/93–100.

14 Chen, L., Pingxiao, Wu P., Chen, M., & Liu, T. (2018). Preparation and characterization of the eco-friendly chitosan/vermiculite biocomposite with excellent removal capacity for cadmium and lead. *Applied Clay Science, 159*, 74–82.

15 Nizhegorodov, A.I. (2016). Eksperimentalnoe opredelenie koeffitsientov treniia nekotorykh potentsialno termoaktivnykh mineralov [Experimental determination of friction coefficients of some potentially thermoactive materials]. *Stroitelnye materialy, 11*, 63–67 [in Russian]. doi: https://doi.org/10.31659/0585–430X-2016–743–11–63–67 [in Russian].

16 Lozano-Lunar, A., da Silva, P.R., de Brito, J., & Rodriguez, J.M.F. (2019). Safe use of electric arc furnace dust as secondary raw material in self-compacting mortars production. *Journal of Cleaner Production, 211*, 1375–1388.

17 Santamaria, A. Faleschini, F., Giacomello, G., Brunelli, K., & Pasetto, M. (2018). Dimensional stability of electric arc furnace slag in civil engineering applications. *Journal. of Cleaner Production, 205*, 599–609.

18 Xu, W., Zhang, J., & Zhang, R. (2017). Application of multi-model switching predictive functional control on the temperature system of an electric heating furnace. *ISA Transaction, 68,* 287–292.

19 Balima, F., Laurence Reinert, L., An-Ngoc, & N. Le Floch, S. (2015). Effect of the temperature on the structural and textural properties of a compressed K-vermiculite. *Chemical Engineering Science, 134,* 555–562.

20 Jinpeng Feng, Meng Liu, Wei Mo, & Xiujuan Su (2021). Heating temperature effect on the hygroscopicity of expanded vermiculite. *Ceramics International, 47(18),* 25373–25380.

21 Fisher, R., Ding, Y., & Sciacovelli, A. (2021). Hydration kinetics of K_2CO_3, $MgCl_2$ and vermiculite-based composites in view of *low-temperature thermochemical e*nergy storage. *Journal of Energy Storage, 38,* 102561.

22 Naveenkumar, K., Suriya, P.A., Divahar, R., Sangeetha, S.P., & Jayakumar, M. (2021). Experimental investigation flexural behavior of *reinforced concrete beam with* partial replacement of vermiculite. *Materials Today: Proceedings, 46 (12)*, 5885–5888.

DOI 10.31489/2021PH4/78-84

UDC621.039

N.A. Suleimenov[1,2*], N.E. Mukhamedov[2], O.M. Zhanbolatov[2]

[1]*D. Serikbayev East Kazakhstan technical University, Ust-Kamenogorsk, Kazakhstan*
[2]*Branch "Institute of Atomic Energy" RSE NNC RK, Kurchatov, Kazakhstan*
([*]E-mail: sna@mail.ru)

Using a user–defined function in Ansys Fluent to implement the energy release profile in model fuel elements taking into account radiation heating

The paper presents a model of an experimental device tested on the complex of impulse graphite reactor of the Branch IAE RSE NNC RK, designed to study the possibility of changing the neutron spectrum of the reactor from thermal to fast. At the stage of preparation for testing, a series of neutron-physical studies were carried out using the MCNP. The purpose of these studies is to determine the specific energy release both in the model fuel elements and in non-fuel structural elements of the experimental device during their radiation heating, taking into account the thermal state of the reactor core. After that, the obtained data are used as initial conditions for development of user-defined functions and conducting thermophysical calculations to determine the distribution of the temperature field in the tested device, the ANSYS Fluent software package. The method for calculating the specific energy release in non-fuel structural elements during their radiation heating in the impulse graphite reactor, considering its thermal state, has been used relatively recently. It requires a special approach to the implementation of the required energy release profile when carrying out thermophysical calculations in the Ansys software. The paper also illustrates the advantages of using a custom function in Ansys Fluent to define the profile of the energy release in model fuel elements and structural elements of an experimental device depending on time and height. In addition, the results of a thermophysical calculation of the experimental device for determining the distribution and maximum values of temperature in fuel and non-fuel structural elements are presented.

Keywords: user–defined function, Ansys Fluent, radiation heating, energy release, fuel elements, experimental device, impulse graphite reactor, thermophysical calculations.

Introduction

The object of research is model fuel rods and structural elements of an in-reactor experimental device [1]. Earlier, in [2], the results of computational studies to substantiate the technology of testing this experimental device were highlighted.

The aim of the work is to demonstrate the methodology for specifying complicated profiles of energy release in model fuel rods and structural elements in the Ansys Fluent software.

The tasks of the work are as follows:

– processing and preparation of the results of neutron-physical calculations;
– preparing a user-defined function for profiling the energy release in model fuel elements and structural elements;
– checking the function and initializing the thermophysical calculation.

Figure 1 shows a model of an experimental device created in the SolidWorks software. The device includes an ampoule, a test section and a trap. The ampoule consists of a body and a lid. The trap protects the ampoule from possible mechanical and thermal effects. The main elements of the test section are the upper and lower fuel rods, which are cooled with nitrogen. The center of the lower fuel rod coincides with the reactor core center (RCC), and the center of the upper fuel rod is at the level of +800 mm from the RCC.

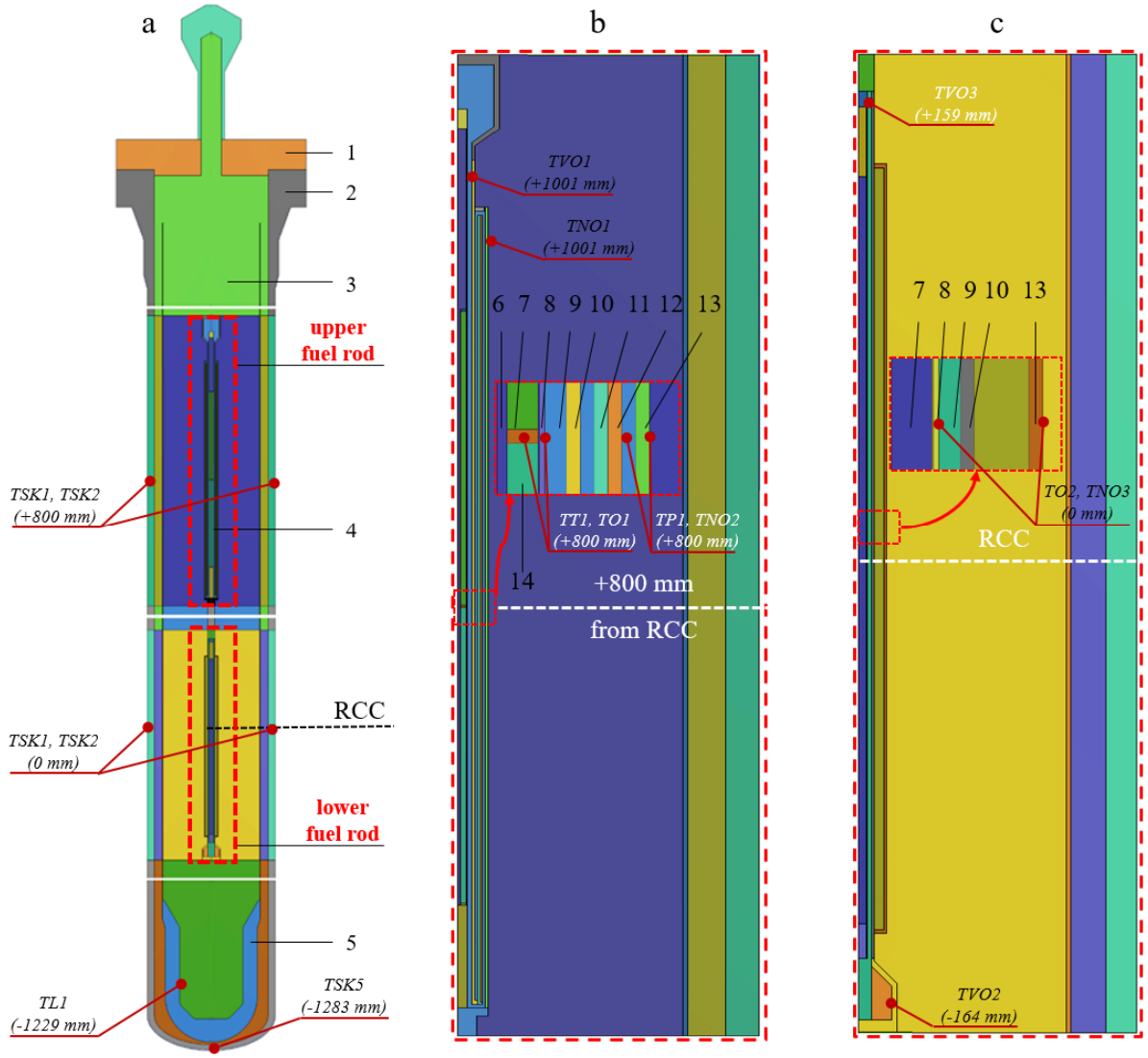

Figure 1. Model of the experimental device: a – general view, b – upper fuel rod, c – lower fuel rod, 1 – ampoule lid, 2 – ampoule body, 3 – ampoule cavity, 4 – test section, 6 – fuel, 7 – nickel indicator, 8 – fuel cladding, 9 – fuel rod cooling tract, 10 – inner shell, 11 – heat shield, 12 – cadmium absorber, 13 – outer shell

Results and Discussion

According to the conditions of the performed neutron–physical calculation, the reactor power is 5.2 MW, the diagram duration is ~ 1000 s, and the integral energy release in the reactor is ~ 5.2 GJ. Taking into account the limiting test mode and the absence of melting of nuclear fuel in the experiment tasks, obtaining accurate estimates of the temperature field is a priority goal of the calculations.

As a result of a neutron-physical calculation carried out in the MCNP program, a reactor power change diagram during the test was obtained, also, the values of the specific power of energy release in the elements — fuel, fuel cladding, inner and outer shells, heat shield and cadmium absorber when they are heated by radiation [3]. The calculations took into account the reactor core heating and the effect of the delayed power on the increase in energy release in the fuel and non-fuel structural elements. The markup, considering this effect, can reach 50 % in structural elements, which can lead to undesirable consequences, such as local overheating, especially in structural elements with a low melting point.

Each element of fuel rods is divided into 10 parts by height (numbered from top to bottom) and has its own specific per-second diagram of the specific power change in accordance with the reactor power diagram change. For example, Figure 2 illustrates a diagram for nuclear fuel.

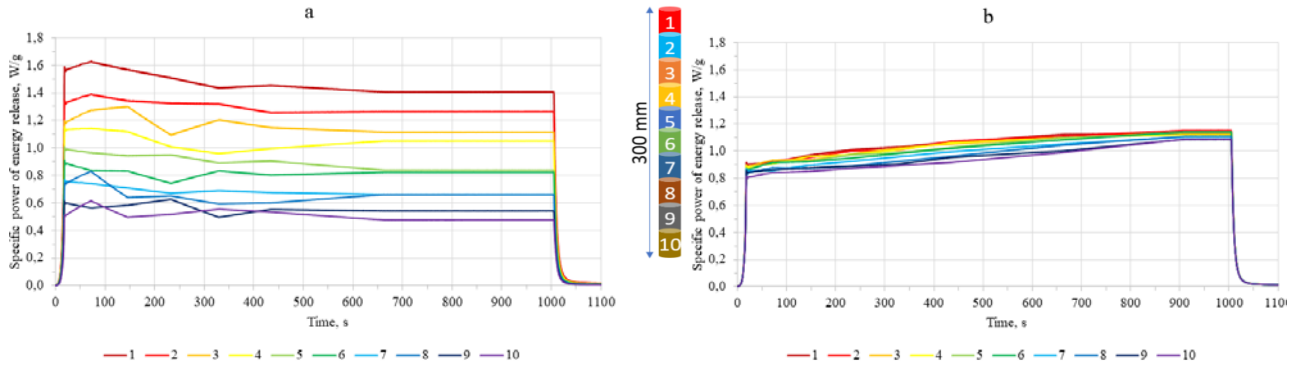

Figure 2. Diagram of the change in the power of energy release in the fuel:
a – upperfuelrod; b – lower fuel rod

The maximum specific power change of energy release in the structural elements of the fuel rods is indicated in Figure 3. The cadmium absorber is strongly exposed to radiation heating, and its specific power diagram change is shown on the auxiliary axis on the right. These values are in the range from 2.5 till 3.2 W/g.

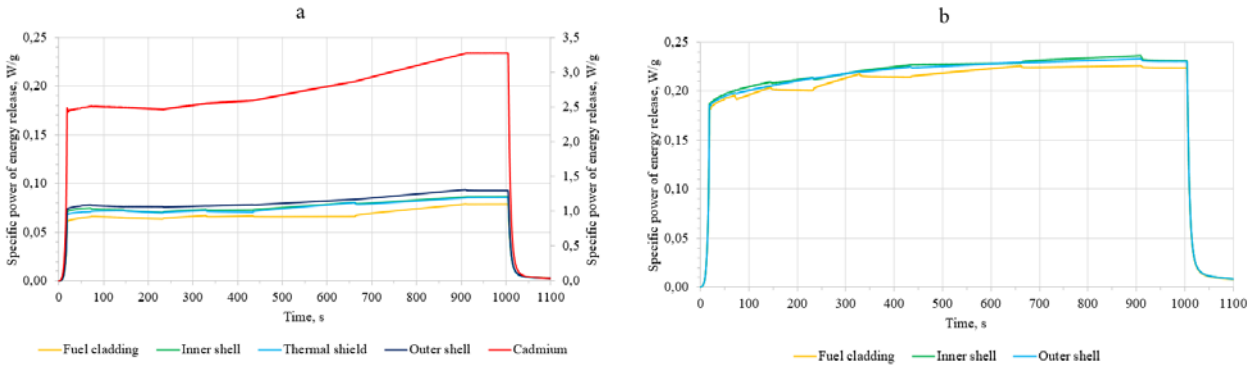

Figure 3. The specific power change of energy release in the structural elements:
a – elements of the upper fuel rod; b – elements of the lower fuel rod

To implement such a profile of energy release without using a custom function, it is necessary to divide the considered elements by height into a predetermined number of parts at the stage of developing a computational thermophysical model, and also, to take into account the distribution of energy release over time when performing calculations. This procedure makes thermophysical calculations a laborious process.

The application of a user-defined function in Ansys Fluent software consists in preparing it, using the C ++ programming language commands and compiling it in Ansys Fluent. Figure 4 shows the general structure of this function.

In the user-defined function, an array of element coordinates by height is set, dividing into the required number of parts, arrays of the energy release values of elements for these coordinates, which are read by the program at certain intervals, set in a separate array according to the reactor power change diagram.

The function also specifies arrays of energy release values in other structural elements of fuel rods — inner and outer shells, heat shield and cadmium absorber.

Next, in the Ansys Fluent software, one needs to import the mesh model, compile the user-defined function and specify the boundary conditions. In the elements where it is necessary to set the energy release, we select the corresponding function from the list (Figure 5). By default, the software allows to set a constant value for the volumetric energy release.

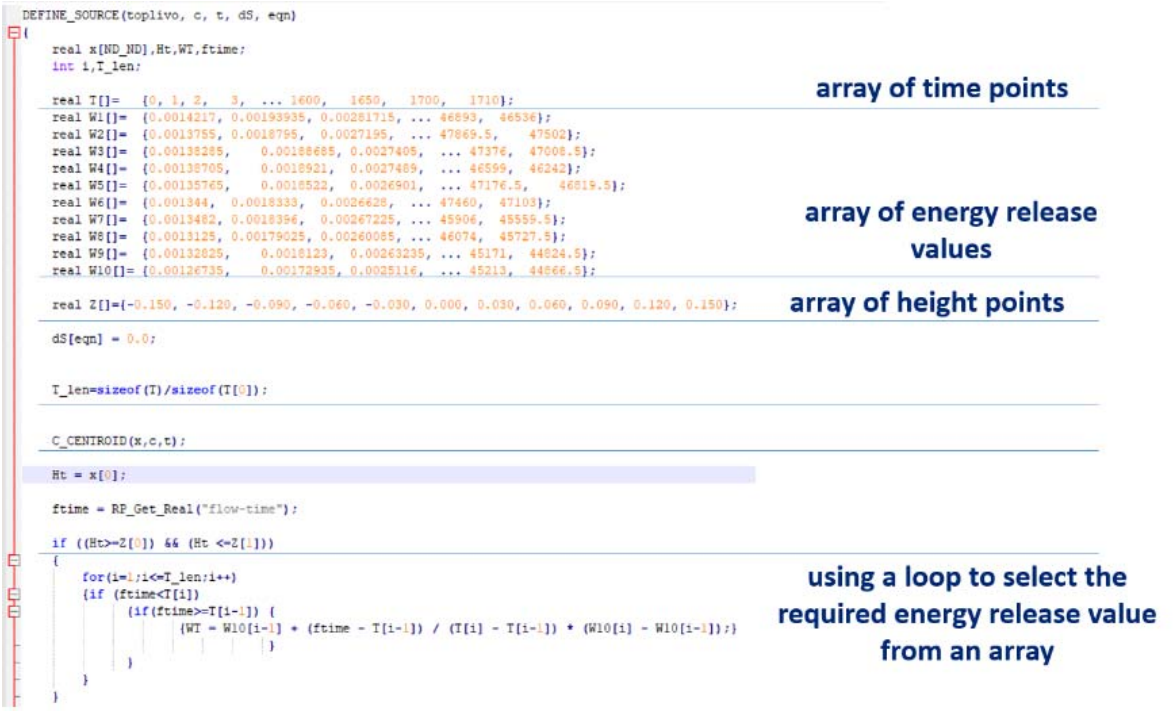

Figure 4. The general structure of function

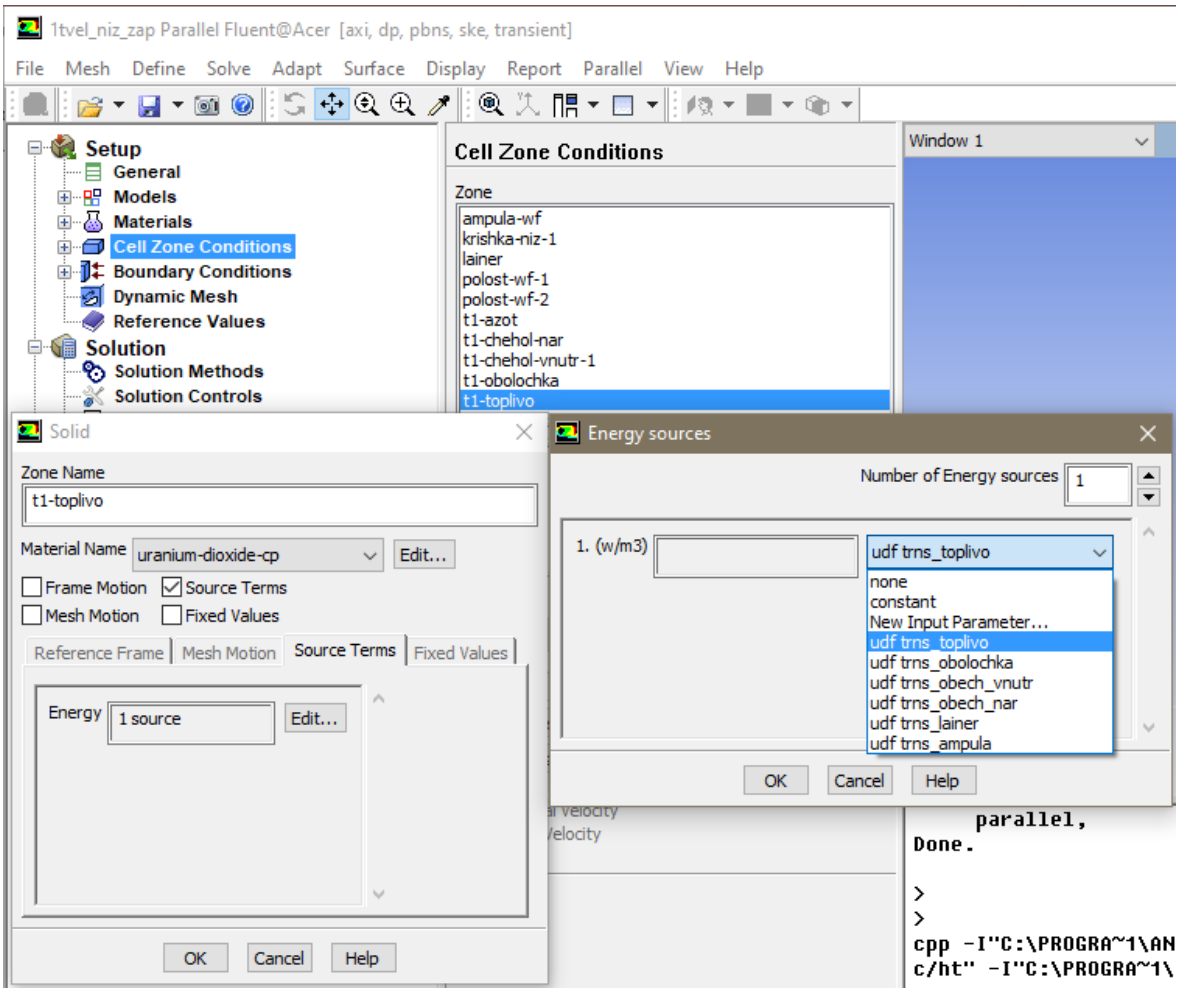

Figure 5. Window for selecting a user-defined function

After that, one needs to initialize the calculation. Considering the obtained calculation results, we can judge the final operability of the function. At the stage of performing a function, its operability can also be checked in a separate external compiler, for example, DevCpp.

As a result of the thermophysical calculation results, the maximum temperature diagram change of the fuel and structural elements during the experiment was obtained (Figure 6). The maximum temperature of the elements is observed at ~ 990 s, which corresponds to the moment of reactor "shutdown" according to the diagram of the experiment. The fuel temperature of the upper fuel element reaches 618 K, the lower one – 475 K. The dynamics of changes in the maximum value of the element temperature (Figure 6a) after 700 s from the beginning of the experiment diagram grows due to the heating of the reactor core, leading to an increase in the energy release in the experimental device elements. This property was taken into account when developing a user-defined function for a more accurate and closer to real conditions calculation, therefore, the energy release profile depending on time is set correctly. The temperature distribution of the elements relative to the reactor core center (RCC) at 990 s from the beginning of the experiment diagram is demonstrated in Figure 7. At this moment, the experimental device elements have different temperatures in height relative to the RCC, which indicates an uneven distribution of energy release along the height and the operability of the user-defined function. In the performed calculation, the mass flow rate of the cooling nitrogen was 2 g / s for each fuel rod.

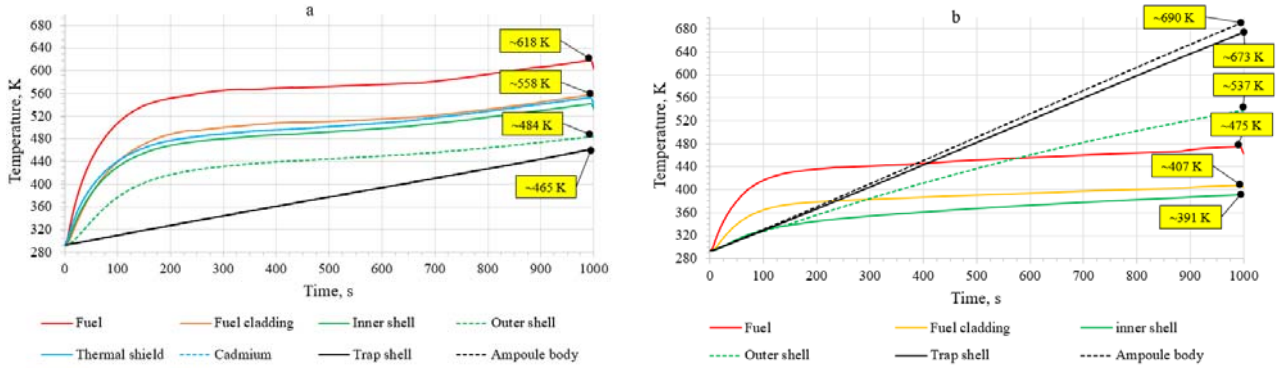

Figure 6. The maximum temperature changing of fuel and structural elements: a – upper fuel rod; b – lower fuel rod

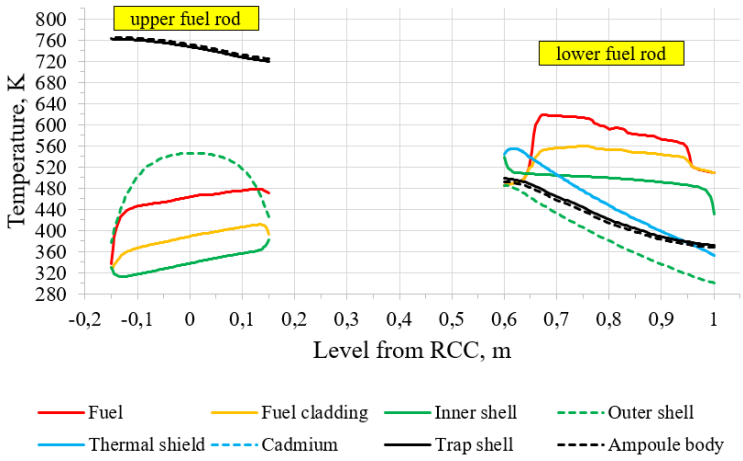

Figure 7. Temperature of fuel and structural elements relative to the RCC at 990 s from the beginning of the experiment diagram

Conclusions

The paper considers a model of an experimental device designed to study the possibility of changing the neutron spectrum of the impulse graphite reactor from thermal to fast. To carry out a thermophysical calculation in the ANSYS Fluent software, closer to real conditions and taking into account the reactor core heating during the test, a user-defined function was developed. Based on the results of the thermophysical calculation, a diagram of the maximum temperature values change in the fuel and structural elements of the device

was obtained. Changes in the maximum temperature of the elements have shown full operability and applicability of user-defined functions for modeling and setting complex profiles of energy release in model fuel elements with a distribution by time and height.

The developed user-defined functions will be used in subsequent computational studies to assess the thermal state of other experimental devices, and can also find their application in other engineering calculations, for example, in aerodynamic and electromagnetic [4–6].

References

1 Сулейменов Н.А. Влияние радиационного разогрева конструкционных материалов экспериментального устройства с конвертером нейтронов на их температурный режим / Н.А.Сулейменов, Н.Е.Мухамедов, В.М.Котов // Вестн. НЯЦ РК. — 2020. — Вып. 4. — № 84. — С. 61–68.

2 Котов В.М. Обоснование технологии экспериментальных исследований твэлов быстрых реакторов в ИГР / В.М. Котов, О.М. Жанболатов, Н.А. Сулейменов // Вестн. НЯЦ РК. — 2020. — Вып. 1. — № 81. — С. 62–67.

3 Жанболатов О.М. Расчет диаграммы мощности экспериментального устройства с конвертором нейтронов / О.М. Жанболатов, Р.А. Иркимбеков, Н.Е. Мухамедов // Вестн. НЯЦ РК. — 2020. — Вып. 4. — № 84. — С. 82–87.

4 Tanasheva N.K. Simulation of flow of the blade wind turbine / N.K. Tanasheva, E.R. Shrager, A.N. Dyusembaeva, A.K. Kussaiynova, D.A. Ospanova, A.R. Bakhtybekova // Bulletin of the university of Karaganda-Physics. — 2016. — No. 4 (84). — P. 20–23.

5 Tanasheva N.K. The study of the aerodynamic coefficients of rotating cylinders/ N.K. Tanasheva, A.N. Dyusembaeva, B.R. Nussupbekov, L.L. Minkov, Zh.G. Nurgalieva, K.K. Sadenova // Bulletin of the university of Karaganda-Physics. — 2019. — № 2 (94). — P. 108–113.

6 Айкеева А.А. ANSYS Maxwell бағдарламалық ортада скип қозғалысының имитациялық моделін жасау / А.А. Айкеева, К.С. Роговая, А.Р. Танскожанова, А.Е. Аюбекова, П.А. Мухтарова, А.Е. Оспанов // Қарағанд. унив. хаб. Физика сер. — 2017. — № 1(85). — Б. 82–88.

Н.А. Сулейменов, Н.Е. Мухамедов, О.М. Жанболатов

Модельдік жылушығарғыш элементтеріндегі энергия шығарылу кескінін іске асыру үшін радиациялық қызуын есепке ала отырып, AnsysFluent бағдарламасындағы пайдаланушы функциясын қолдану

Мақала импульстік графитреактордың нейтрондық спектрін жылулықтан шапшаңға өзгерту мүмкіндігін зерттеуге арналған және ҚР ҰЯО РМК «Атом энергиясы институты» филиалының импульстік графитреактор кешенінде сыналған эксперименттік құрылғының моделі көрсетілген. Сынауға дайындау барысында MCNP бағдарламалық кодын қолданып, көптеген нейтрон-физикалық зерттеулер мен есептер өткізілді. Зерттеулердің мақсаты жылушығарғыш элементтердің ядролық отындағы және отынсыз конструктивтік элементтердің радиациялық қызу кезінде импульстік графитреактордың жылулық күйін есепке алумен меншікті энергия шығарылуын анықтау болып табылады. Алынған мәліметтердің бастапқы шарттары пайдаланушы функциясын әзірлеу және сыналып жатқан эксперименттік құрылғының температура өрісін анықтау мақсатымен AnsysFluent бағдарламалық жасақтамасында өткізілетін жылуфизикалық есептерде қолданылады. Отынсыз конструктивтік элементтердің импульстік графитреакторында радиациялық қызу кезінде және де реактордың жылулық күйін есепке алатын, меншікті энергия шығарылуын санау әдістемесі кейінгі уақытта қолданыла басталған. Оған AnsysFluent бағдарламалық жасақтамасында өткізілетін жылуфизикалық есептерде керекті энергия шығарылу кескінін іске асыру үшін жеке тәсілдеме қажет. Сонымен қатар, мақалада эксперименттік құрылғының модельдік жылушығарғыш және конструктивтік элементтерінде уақытқа және биіктікке тәуелді меншікті энергия шығарылу кескінін Ansys Fluent бағдарламасында қою үшін пайдаланушы функциялардың артықшылықтары көрсетілген. Мұнан басқа эксперименттік құрылғының отынды және отынсыз конструктивтік элементтерінің температура үлестірімі және оның максимум мәнін анықтау үшін өткізілген жылуфизикалық есептеудің нәтижелері келтірілген.

Кілт сөздер: пайдаланушы функциясы, Ansys Fluent, радиациялық қызу, энергия шығарылуы, жылушығарғыш элемент, эксперименттік құрылғы, импульстік графит реакторы, жылуфизикалық есептеу.

Н.А. Сулейменов, Н.Е. Мухамедов, О.М. Жанболатов

Применение пользовательской функции в Ansys Fluent для реализации профиля энерговыделения в модельных твэлах с учетом радиационного разогрева

В статье представлена модель экспериментального устройства, испытанного на комплексе импульсного графитового реактора Филиала ИАЭ РГП НЯЦ РК и предназначенного для изучения возможности изменения спектра нейтронов реактора из теплового в быстрый. На этапе подготовки к испытаниям проведен ряд нейтронно-физических исследований и расчетов с использованием программного кода MCNP. Целью исследований — определение удельного энерговыделения как в топливе модельных твэлов, так и в нетопливных конструктивных элементах экспериментального устройства в процессе их радиационного разогрева с учетом теплового состояния активной зоны реактора. После чего полученные данные были использованы в качестве начальных условий для разработки пользовательской функции и проведения теплофизических расчетов по определению распределения температурного поля в испытываемом устройстве в программном пакете Ansys Fluent. Методика расчета удельного энерговыделения в нетопливных конструктивных элементах в процессе их радиационного разогрева в реакторе, с учетом его теплового состояния, применяется относительно недавно. Это требует особого подхода к реализации необходимого профиля энерговыделения при проведении теплофизических расчетов в Ansys Fluent. В работе показаны преимущества пользовательской функции в Ansys Fluent для задания профиля удельного энерговыделения в модельных твэлах и конструктивных элементах испытанного экспериментального устройства в зависимости от времени и высоты. Кроме этого, приведены результаты проведенного теплофизического расчета экспериментального устройства по определению распределения и максимальных значений температуры в топливе и нетопливных конструктивных элементах.

Ключевые слова: пользовательская функция, Ansys Fluent, радиационный разогрев, энерговыделение, твэл, экспериментальное устройство, импульсный графитовый реактор, теплофизические расчеты.

References

1 Suleimenov, N.A., Mukhamedov, N.E., & Kotov, V.M. (2020). Vliianie radiatsionnogo razogreva konstruktsionnykh materialov eksperimentalnogo ustroistva s konverterom neitronov na ikh temperaturnyi rezhim [Effect of radiation heating of construction materials of an experimental device with a neutron converter on their temperature regime]. *Vestnik NIaTs RK— NNC RK Bulletin, 4 (84)*, 61–68 [in Russian].

2 Kotov, V.M., Zhanbolatov, O.M., & Suleimenov, N.A. (2020). Obosnovanie tekhnologii eksperimentalnykh issledovanii tvelov bystrykh reaktorov v IGR [Substantiation of an experimental study technologyof fuel rods of fast reactors in the IGR]. *Vestnik NIaTs RK — NNC RK Bulletin, 1 (81)*, 62–67 [in Russian].

3 Zhanbolatov, O.M., Irkimbekov, R.A., & Mukhamedov, N.E. (2020). Raschet diagrammy moshchnosti eksperimentalnogo ustroistva s konvertorom neitronov [Calculation of the power diagram of an experimental device with a neutron converter]. *Vestnik NIaTs RK — NNC RK Bulletin, 4 (84)*, 82–87 [in Russian].

4 Tanasheva, N.K., Shrager, E.R., Dyusembaeva, A.N., Kussaiynova, A.K., Ospanova, D.A., & Bakhtybekova A.R. (2016). Simulation of flow of the blade wind turbine. *Bulletin of the Karaganda University-Physics, 4(84),* 20–23.

5 Tanasheva, N.K., Dyusembaeva, A.N., Nussupbekov, B.R, Minkov, L.L., Nurgalieva, Zh.G., & Sadenova,K.K. (2019). The study of the aerodynamic coefficients of rotating cylinders. *Vestnik Karagandinskogo universiteta. Seriia Fizika — Bulletin of the Karaganda University – Physics, 2(94),*108–113.

6 Aikeeva, A.A., Rogovaia, K.S., Tanskozhanova, A.R. Aiubekova, A.E., Mukhtarova, P.A., & Ospanov, A.E. (2017). ANSYS Maxwell bagdarlamalyq ortada skip qozgalysynyn imitatsiialyq modelin zhasau [Development of imitating model of skip motion in the programenvironment ANSYS Maxwell]. *Karagandy universitetinin khabarshysy. Fizika seriiasy — Bulletin of the Karaganda University – Physics, 1(85),*82–88 [in Kazakh].

DOI 10.31489/2021PH4/85-93

UDC 638.21.4

Z.K. Sattinova[1*], T.N. Bekenov[1], B.K. Assilbekov[2], G.I. Ramazanova[2], K.M. Dyusenov[1]

[1]*L.N. Gumilyev Eurasian National University, Nur-Sultan, Kazakhstan;*
[2]*Satbayev University, Almaty, Kazakhstan*
(E-mail: [*]Sattinova_zamira@mail.ru)

Development of the algorithm for calculating the optimal molding modes of the BeO slurry using various rheological models

This paper presents the results of calculating a mathematical model of the flow and heat transfer of thermoplastic beryllium oxide in a round channel of a molding installation. An algorithm for calculating the system of equations based on the Herschel-Bulkley rheological model has been developed. The finite-difference analogue of the equations system of motion, continuity, and energy is solved numerically using the Crank-Nicholson difference scheme. The three-parameter equation is used to test the consistency of experimental, data, and how adequately the physical features of the non-isothermal flow of the slurry convey comparing to the Shvedov-Bingham model. The calculation results illustrate that the proposed model reflects the most important features of the thixotropic flow character of the slurry and is in better agreement with the experimental data of viscoplastic fluids. It provides the calculations of speed of viscous-plastic flow of the slurry based on Shvedov-Bingham and Herschel Bulkley's two rheological models considering the peculiarities of coagulation structure formation and flow mechanism with boundary conditions. As a result of calculations, the fields of velocity, temperature, and density were obtained, which describe the regularities of the flow and heat transfer of a thermoplastic slurry. The change in the Nusselt criterion along the length of the shaping cavity is shown, which coincides with the analytical solution of Nusselt under first kind boundary conditions. The optimal conditions for the process of ceramics molding by hot casting method have been found, allowing to obtain a hardened product with a homogeneous structure of beryllium ceramics at the outlet.

Keywords: thermoplastic slurry, beryllium oxide, ceramics, rheological model, Herschel Bulkley, thixotropic, viscous-plastic, non-isothermal.

Introduction

High-density beryllium oxide ceramics are widely used in various fields of new technology due to a number of valuable properties and above all, unique thermal conductivity. The manufacture of high-tech beryllium ceramics by the slurry (extrusion) molding, similar to MIM (Metal Injection Molding) technology, includes the same physical processes and methods that reduce the cost of rejected products and significantly improve the quality of products.

During industrial tests, thermoplastic slurry has been used to obtain ceramic products — a highly viscous suspension with different organic binder contents: 9.5; 10.7 and 11.7% prepared from beryllium oxide powder (grade H1 specific surface area 1,57 m2/g). The organic binder includes three components: paraffin, beeswax, oleic acid in a ratio (82; 15 and 3%) [1].

The molding unit tank is filled with thermoplastic molten slurry and the mold is filled under pressure. In the molding process, there is a difficulty in the deformation behavior of the molding because of the high thermal conductivity of the dispersion medium. In the temperature range of 40–59 ° C, the volume-phase characteristics of the slurry mass changes and the volume of the liquid phase increases. An increase in the volume of the liquid phase and the presence of an additional amount of binder lead to structural defects. Effective control of the molding process to reduce the content of the liquid phase while maintaining the high fluidity of the slurry was carried out under the influence of a pressure gradient resulting from ultrasonic (US) effects.

The present paper examines the viscous-plastic course of the beryllium ceramic molding process based on experimental data obtained from actual injection molding plants [2]. The reasonable choice and calculation of the optimal mode of the beryllium ceramic molding process are, from an energy point of view, a paramount technological task for the production of ceramic products.

Numerical calculations of the mathematical model of the process take into account the thixotropic-dilatant and complex rheological behavior of the slurry on rheological models, the dependence of thermophysical characteristics on temperature, non-isothermal flow, and heat exchange when the aggregate state

changes. A detailed discussion of the conditions of heat exchange and phase conversion is not our task however, it was necessary to note the solidification temperature of the slurry.

Calculation of non-isothermal flow based on the rheological model of a power-law fluid

Non-isothermal movement of thermoplastic slurry in molding cavity of molding unit is considered (Fig. 1). The structure of the molding cavity is made in the form of coaxial pipes. Inner pipe with radius of $r_1 = 0{,}045\,m$ forms cavity and circular layer with radii of $r_2 = 0{,}005$ and $r_3 = 0{,}015$ — casing for circulation of cooling liquid. Liquid slurry with initial temperature of $T_0 = 75$℃ flows in and moves into forming cavity. According to experimental data, the maximum value of the molding speed does not exceed 2 mm/min.

As it moves, the slurry cools and solidifies acquiring a structural shape at the outlet of the pipe [3].

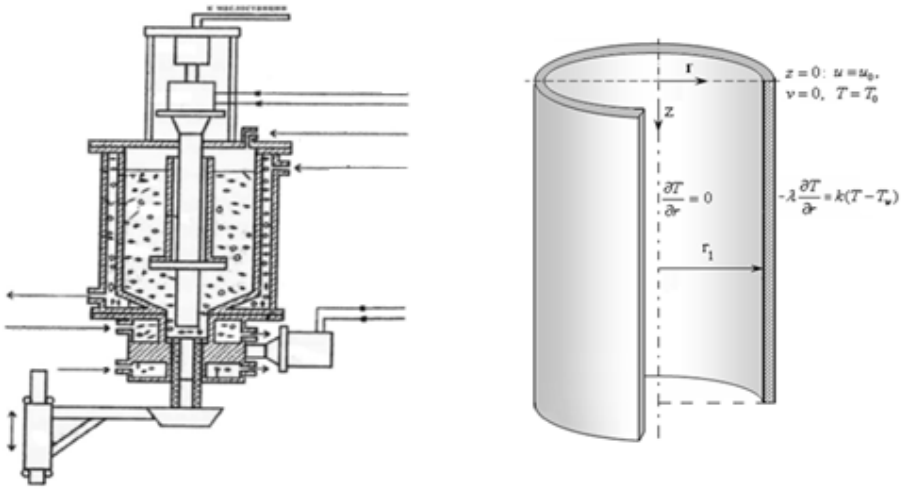

Figure 1. Diagram of industrial ultrasonic (UZ) molding plant

The wall of the molding cavity is cooled by water circulating in the annular casing. The cooling zone is divided into three parts, in the first compartment the water temperature $T_{w1} = 73$℃, in the second $T_{w2} = 59$℃, in the third $T_{w3} = 45$℃. The total length of the cavity $L = 0{,}108$ м: the length of the hot, warm, and cold part of the pipe is equal to $L_1 = 0{,}022\,m,\ L_2 = 0{,}045\,m,\ L_3 = 0{,}041$ m, respectively.

For numerical calculations of non-isothermal flow and heat exchange of thermoplastic slurry, a mathematical model is presented by the following system of equations of motion, continuity and heat exchange [4].

$$\rho u\frac{\partial u}{\partial z} + \rho v\frac{\partial u}{\partial r} = -\frac{dP}{dz} + \frac{\partial \tau_0}{\partial r} + \frac{\partial}{\partial r}\left(B\frac{\partial u}{\partial r}\right) + \rho g; \tag{1}$$

$$\frac{\partial(\rho u)}{\partial z} + \frac{1}{r}\frac{\partial(\rho v r)}{\partial r} = 0; \tag{2}$$

$$\rho u c_p\frac{\partial T}{\partial z} + \rho v c_p\frac{\partial T}{\partial r} = \frac{1}{r}\frac{\partial}{\partial r}\left(\lambda r\frac{\partial T}{\partial r}\right) + L_k\frac{d\rho}{dt} + B\left(\frac{\partial u}{\partial r}\right)^2. \tag{3}$$

The system of equations (1) – (3) is closed by the Herschel-Bulkley rheological equation, in which the quasi-Newtonian viscosity is determined by the relation [5; 6]:

$$B = k(T)\left|\frac{\partial u}{\partial r}\right|^{n-1} \tag{4}$$

In (1) – (3), z, r – cylindrical coordinates; u, v – speed components; $p, \rho, T, \tau_0, B, \lambda, c_p, L_k$ – pressure, density, temperature, yield strength, quasi-Newtonian viscosity coefficient, thermal conductivity, the slurry heat capacity and crystallization heat, respectively. Density, coefficients of heat capacity, viscosity and thermal conductivity of the slurry depend on temperature and their dependencies are determined by empirical formulas obtained on the basis of experimental data [7].

The effect of mechanical energy dissipation is not significant, however, taken into account in the calculations. The condition of maintaining the mass flow rate of the current medium in the mass-forming cavity makes it possible to find the pressure drop necessary to control the molding speed:

$$2\pi \int_0^{r_1} \rho u r dr = \pi r_1^2 \rho_0 u_0 \quad (5)$$

The speed and temperature distribution at the inlet is assumed to be constant along the channel section, accordingly, all thermo-physical characteristics of the slurry are constant. Boundary conditions are recorded at channel input:

$$\text{at } z = 0: \ u = u_0, \ v = 0, \ T = T_0; \quad (6)$$

on the walls of the channel in the area of the liquid state of the slurry for speed, adhesion conditions are set:

$$\text{at } z > 0, r = 0: \ \frac{\partial u}{\partial r} = \frac{\partial T}{\partial r} = 0, \ v = 0; \quad (7)$$

and in the field of solid plastic state — conditions of non-flowing and sliding:

$$\text{at } z > 0, \ r = r_i, \ v = 0, \ -\frac{dP}{dz} = \frac{2}{r_1}\left(\tau_{0i} + \left(k\frac{\partial u}{\partial r}\right)^n\right), i = 1,2. \quad (8)$$

Heat exchange on the outer wall is determined in accordance with the temperature value in the cooling contour of the cavity. We denote the temperature of water in hot, warm, cold contours T_1, T_2, T_3, respectively, and then we have boundary conditions for the temperature on the outer wall:

$$\begin{gathered} \text{at } \ 0 \le z < l_1, \ r = r_1, \ -\lambda\frac{\partial T}{\partial r} = k(T - T_1); \\ \text{at } \ l_1 \le z < l_2, \ r = r_1, \ -\lambda\frac{\partial T}{\partial r} = k(T - T_2); \\ \text{at } \ l_2 \le z < l_3, \ r = r_1, \ -\lambda\frac{\partial T}{\partial r} = k(T - T_3). \end{gathered} \quad (9)$$

The heat transfer coefficient *k* is in the standard manner [8].

The system of equations (1) – (3) is given to dimensionless variables. As a result of transition to dimensionless variables of the Reynolds equation, Bingham, Nusselt, Prandtl and Bio:

$$\tilde{z} = \frac{z}{r_1}, \tilde{r} = \frac{r}{r_1}, \ \tilde{u} = \frac{u}{u_0}, \tilde{v} = \frac{v}{u_0}, \tilde{\rho} = \frac{\rho}{\rho_0}, \tilde{\tau} = \frac{\tau}{\tau_0}, \ \tilde{T} = \frac{T}{T_0}, \tilde{P} = \frac{P}{\rho_0 u_0^2},$$
$$\tilde{L}_k = \frac{L_k}{c_{p0}T_0}, Re = \frac{\rho \cdot U^{2-n} {r_1}^n}{\mu}, \ Bin = \frac{\tau_0 \cdot {r_1}^{n-1}}{\mu \cdot U^n}, \ Nu = \frac{\alpha_1 r_1}{\lambda}, \ Pr = \frac{c_p \mu}{\lambda}, \ Bi = \frac{K \cdot r_1}{\lambda}.$$

grid points in each coordinate direction Oz and Or designates $\Delta z, \Delta r$ and are calculated by the formulas:

$$\Delta z = z_{n+1} - z_n, \qquad \Delta r = r_{j+1} - r_{j-1}, \qquad \Delta r_+ = r_{j+1} - r_j, \qquad \Delta r_- = r_j - r_{j-1}, \qquad r_{j+1/2} - r_{j-1/2} = \Delta \dot{r}$$

where $\Delta z, \Delta r$ vary in the range $0 \le \Delta \le 1$.

The difference analogues of the equations of motion (1) and energy (3) are obtained according to the Crank-Nicolson scheme. Then the equations of motion can be represented as:

$$\frac{\left[\theta\left(\rho_j^{n+1}u_j^{n+1}\right) + (1-\theta)\rho_j^n u_j^n\right]\left(u_j^{n+1} - u_j^n\right)}{\Delta z} +$$
$$\frac{\theta\left(\rho_j^{n+1}v_j^{n+1}\right)\left(u_{j+1}^{n+1} - u_{j-1}^{n+1}\right) + (1-\theta)\left(\rho_j^n v_j^n\right)\left(u_{j+1}^n - u_{j-1}^n\right)}{r_{j+1} - r_{j-1}} +$$
$$= -\left(\frac{dp}{dz}\right)^{n+1} + \frac{\theta}{r_{j+1/2} - r_{j-1/2}}\left[B_{j+1/2}^{n+1}\frac{u_{j+1}^{n+1} - u_j^{n+1}}{r_{j+1} - r_j} - B_{j-1/2}^{n+1}\frac{u_j^{n+1} - u_{j-1}^{n+1}}{r_j - r_{j-1}}\right]$$
$$+ \frac{1-\theta}{r_{j+1/2} - r_{j-1/2}}\left[B_{j+1/2}^{n}\frac{u_{j+1}^{n} - u_j^{n}}{r_{j+1} - r_j} - B_{j-1/2}^{n}\frac{u_j^{n} - u_{j-1}^{n}}{r_j - r_{j-1}}\right] + \frac{\tau_{0,j+1}^{n+1} - \tau_{0,j-1}^{n+1}}{r_{j+1} - r_{j-1}}.$$

The resulting difference equation is nonlinear with respect to the desired quantities, therefore, to find them, it is necessary to iterate along the nonlinearity or apply the Newton linearization method [9].

$$\frac{\theta\rho_j^{n+1}u_j^{n+1}u_j^n + (1-\theta)\rho_j^n u_j^n u_j^{n+1} - \theta\rho_j^{n+1}u_j^{n+1}u_i^n}{\Delta z} + \frac{\theta\rho_j^{n+1}v_j^{n+1}\left(u_{j+1}^{n+1} - u_{j-1}^{n+1}\right)}{r_{j+1} - r_{j-1}} -$$

$$-\frac{\theta}{r_{j+1/2}-r_{j-1/2}}\left[\frac{B_{j+1/2}^{n+1}}{r_{j+1}-r_j}\left(u_{j+1}^{n+1}-u_j^{n+1}\right)-\frac{B_{j-1/2}^{n+1}}{r_j-r_{j-1}}\left(u_j^{n+1}-u_{j-1}^{n+1}\right)\right]-$$

$$-\theta\frac{\tau_{0,i+1}^{n+1}-\tau_{0,i-1}^{n+1}}{r_{j+1}-r_{j-1}}=-\left(\frac{dp}{dz}\right)^{n+1}+\frac{(1-\theta)\rho_i^n u_i^n u_i^n}{\Delta z}-\frac{(1-\theta)\rho_i^n v_i^n(u_{i+1}^n-u_{i-1}^n)}{r_{j+1}-r_{j-1}}+$$

$$+\frac{1-\theta}{r_{j+1/2}-r_{j-1/2}}\left[\frac{B_{j+1/2}^{n}}{r_{j+1}-r_j}\left(u_{j+1}^{n}-u_j^{n}\right)-\frac{B_{j-1/2}^{n}}{r_j-r_{j-1}}\left(u_j^{n}-u_{j+1}^{n}\right)\right]\equiv-\left(\frac{dp}{dz}\right)^{n+1}+$$

$$+RHS_j^n+(1-\theta)\frac{\tau_{0,j+1}^n-\tau_{0,j-1}^n}{r_{j+1}-r_{j-1}}.$$

Accuracy of calculating the flow strongly depends on the way of calculation B_j^{n+1}, then it can be written as:

$$B_{j+1/2}^{n+1}=\frac{1}{2}\left(B_{j+1}^{n+1}-B_j^{n+1}\right),$$

$$B_{j-1/2}^{n+1}=\frac{1}{2}\left(B_{j-1}^{n+1}-B_j^{n+1}\right).$$

$$\frac{\theta}{r_{j+1/2}-r_{j-1/2}}\left[\frac{B_{j+1/2}^{n+1}}{r_{j+1}-r_j}\left(u_{j+1}^{n+1}-u_j^{n+1}\right)-\frac{B_{j-1/2}^{n+1}}{r_j-r_{j-1}}\left(u_j^{n+1}-u_{j-1}^{n+1}\right)\right]=\frac{\theta}{2\Delta\dot{r}_j}*$$

$$*\left[\frac{\left(B_{j+1}^{n+1}+B_j^{n+1}\right)\left(u_{j+1}^{n+1}-u_j^{n+1}\right)}{\Delta r_j^+}-\frac{\left(B_j^{n+1}+B_{j-1}^{n+1}\right)\left(u_j^{n+1}-u_{j-1}^{n+1}\right)}{\Delta r_j^-}\right].$$

After linearizing nonlinear elements in the equation of motion to find u_j^{n+1}, the difference analogue of the equation is reduced to the three–point form:

$$-a_j^n u_{j+1}^{n+1}+b_j^n u_j^{n+1}-c_j^n u_{j-1}^{n+1}=\delta_j^n-\left(\frac{dp}{dz}\right)^{n+1}.$$

When calculating internal flows, the pressure gradient, which is an unknown quantity, in the process of solving it, will be determined by splitting method from condition of preservation of mass flow rate:

$$\int_0^1\rho_j^{n+1}u_j^{n+1}\,rdr=\frac{1}{2} \tag{10}$$

For determining $\left(\frac{dp}{dz}\right)^{n+1}$ the splitting method is used [9]:

$$u_j^{n+1}=\varphi_j^{n+1}+\left(-\frac{dp}{dz}\right)^{n+1}\cdot S_j^{n+1} \tag{11}$$

Thus, the solution algorithm u_j^{n+1} has the form: 1) from difference analogs $\varphi_j^{n+1}, S_j^{n+1}$ the desired variables are calculated by the sweep method; 2) by found values $\varphi_j^{n+1}, S_j^{n+1}$ definite integrals are found by the Simpson method and the pressure gradient $\left(\frac{dp}{dz}\right)^{n+1}$; 3) calculated u_j^{n+1}.

Similarly, the heat transfer equation is represented in finite-difference form by the Crank-Nicolson scheme.

Results and Discussion

Calculation of non-isothermal flow and heat transfer of thermoplastic slurry which based on the Bulckley-Herschel model gives the following results. The calculations provided for two identical operating parameters similar to the Bingham model [10]. Figure 2 (b) shows that the velocity profiles have a more filled form, and decreasing of the velocity on the axis is associated with a high consistency of the slurry mass. The developed profile of the shear rate increases the cooling effect from the side of the wall and this, in turn, leads to intensive heat transfer between the slurry and the cooling liquid, hence, to an increase in viscosity. As can be seen from Figure 2 (a), in hot and warm contours with the slurry which located in the central region of the pipe occurs heat transfer due to convection. When transition to warm contour $z=23\,mm$, large changes of temperature along the channel radius are demonstrated which are related to the temperature gradient. Further, the temperature distribution in the core of the flow over the cross sections is reduced and remains almost uniform in the cold contour (Fig. 2, a). Beginning with $z=63\,mm$, the speed distribution

becomes more uniform because of the balance between the cooling effect and the internal phenomenon of convection. The filled profile of the shear rate of the considering model does not always ensure the uniformity of the structure of the slurry mass, however, with the correct choice of thermal parameters, positive results can be obtained.

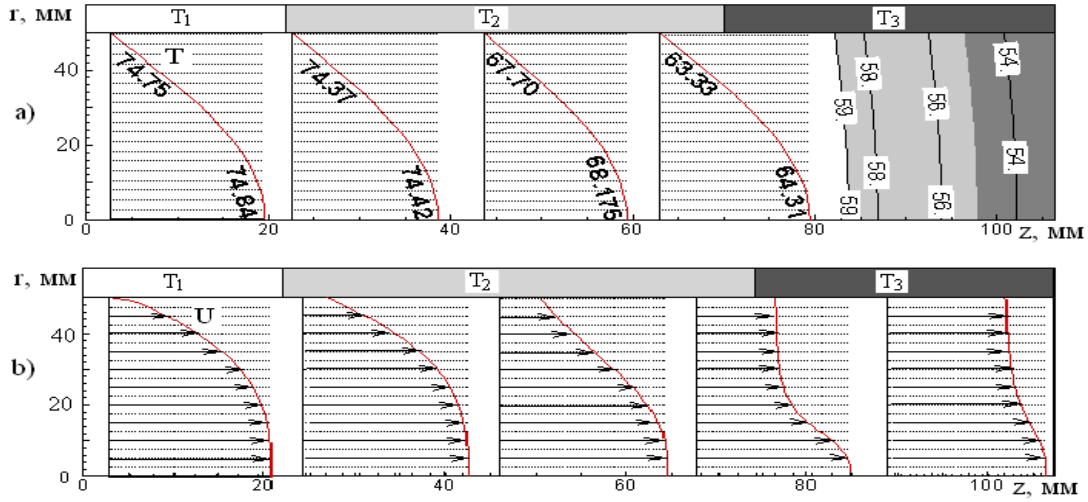

Figure 2. Temperature (a) and speed distribution (b) along the pipe length:

$$u = 1\ mm/min, \qquad r_1 = 45\ mm, \qquad Re = 3{,}52 \cdot 10^{-4}$$

As the thickness of the round pipe decreases, the temperature of crystallization is reached near the wall at a distance of z = 59 mm, and the crystallization front at a sharp rate covers the entire crosscut layer of the round channel (Fig. 3). The developed speed profile facilitates rapid heat removal from the inside of the slurry to the wall. At transition to cold contour the slurry is in solid-plastic state and the temperature of the slurry at all points shall be equal to temperature of cooling liquid of this contour [11]. The solidification begins with a cold contour, followed by a sharp increase in the density of the thermoplastic slurry. The calculated data of the speed profile, obtained using the Bulkley-Herschel model, have a more filled form with a constant core in the central part of the flow (Fig. 3), which is in qualitative agreement with the data of the analytical solution of the motion of a non-Newtonian fluid in a round channel.

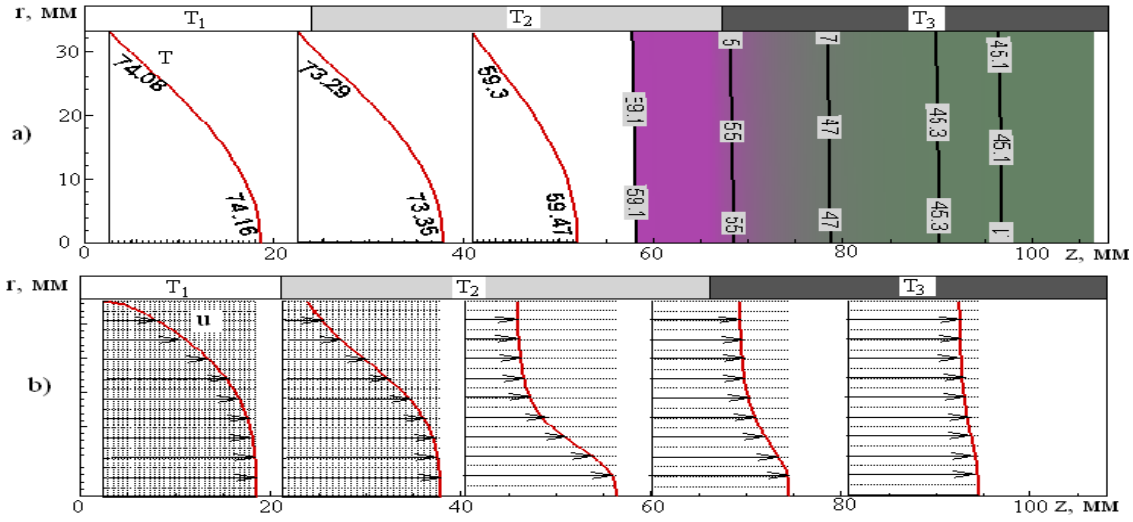

Figure 3. Temperature (a) and speed distribution (b) along the pipe length:

$$u = 1\ mm/min, \qquad r_1 = 33\ mm, \qquad Re = 1{,}95 \cdot 10^{-4}$$

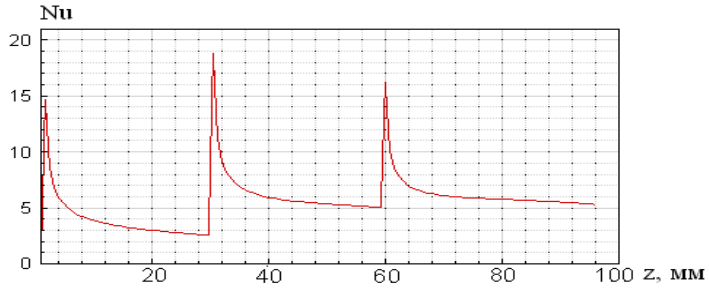

Figure 4. Nusselt criterion change along the pipe length

The regularities of the change of temperature and longitudinal speed profiles cause the change in the Nusselt number (Fig. 4). The presented dependence of the Nu number on Z testifies that in the warm and cold contours, the change in slurry viscosity with temperature has a stronger effect on heat transfer than in the hot contour, where the temperature gradient is insignificant. When falling temperature is different, Nusselt number decreases much faster (warm contour) than in a cold contour, where the rising temperature head slows down the fall Nu. The problem of heat transfer for a laminar flow of a non-Newtonian fluid, in a round pipe at a constant wall temperature, was solved to verify the numerical method. The change in the Nusselt criterion (dimensionless heat transfer coefficient) along the pipe length decreases monotonically in each contour and tends to a constant value that coincides with the analytical Nusselt solution under *first-kind boundary condition [12]*.

As can be seen from Figure 5, the calculation data, obtained using the Herschel-Bulkley model, indicate good agreement with the results of experiments and industrial tests. In the calculated temperature range, the change in density in the liquid state is (2.355–2.38) g/cm^3, in solid plastic — (2.38–2.43) g/sm^3.

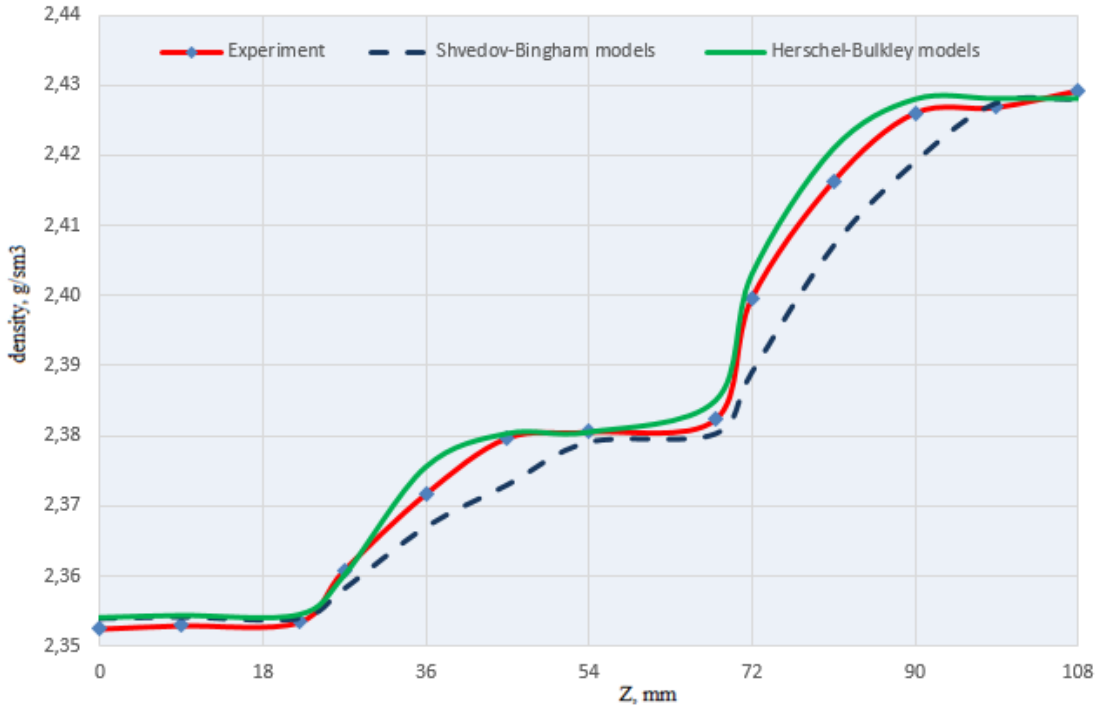

Figure 5. Density change of the slurry along the pipe length

The obtained results of calculations of the process of thermoplastic slurry solidification under the specific conditions of the round pipe of the molding installation make it possible to clearly represent the kinetics of solidification depending on the molding modes, the structure of the molding mass and the peculiarities of the configuration of the articles.

Conclusions

Numerical calculations of non-isothermal flow and heat exchange of thermoplastic slurry based on Shvedov-Bingham and Herschel-Bulkley two rheological models are compared with experimental data. The application of the Herschel-Bulkley rheological model describing the non-thermal flow and the gradual transition from the flowing state after the destruction of the slurry mass structure to the solid state is justified by the thixotropic-dilatant properties of the slurry. The rheological behavior of the viscoplastic slurry is complex when different flow modes exist at different shear rate intervals depending on the duration of treatment of the slurry with exposure. Rheological parameters of viscoplastic slurry are determined experimentally in the studied area, where with existing measurement methods reliable results.

The given results of mathematical model calculations help to find optimal parameters of thermal regime of the slurry molding in forming cavity to reduce production costs of molding system. The calculated data show the applicability of the Herschel-Bulkley rheological model in a wider range of molding systems compared to the Shvedov-Bingham model. The optimum conditions of the process of molding of BeO thermoplastic slurry were found, which make it possible to obtain a solidified product with a unified structure of beryllium ceramics at the outlet.

The results of the study, obtained using the Herschel-Bulkley rheological model, lead to the following conclusion:

– speed profiles have a more filled appearance with a constant core in the central portion of the flow;
– unified speed distribution contributes to unified fields of temperature, density and improvement of other thermo-physical properties of the slurry;
– speed epures with a constant core in the central part of the stream satisfy the theoretical data.

References

1 Шахов С.А. Применение ультразвука при производстве высокотеплопроводных керамических изделий / С.А. Шахов, Г.Д. Бицоев. — Усть-Каменогорск, 1999. — 145 с.

2 Rudert A. Experimental and numerical investigation of a viscoplastic Carbopol gel injected into a prototype 3D mold cavity / A. Rudert, R. Schwarze // Non-Newtonian Fluid Mech. – 2009. Vol. 161, № 1–3. P. 60–68.

3 Zhapbasbayev U. Experimental and calculated data of the beryllium oxide slurry solidification / U. Zhapbasbayev, G.Ramazanova, Z. Sattinova, B. Kenzhaliev, S. Shakhov // Applied Thermal Engineering. — 2016. — Vol. 96, P. 593–599. https://www.sciencedirect.com/journal/applied-thermal-engineering/vol/96

4 Фройштетер Г.Б. Течение и теплообмен неньютоновских жидкостей в трубах / Г.Б. Фройштетер, Э.Л. Смородинский, Н.В. Радионова. — Киев: Наук. думка, 1990. — 216 с.

5 Borzenko E.I. Free-surface flow of a viscous-plastic fluid during the filling of a planar channel / E.I. Borzenko, K.E. Ryltseva, G.R. Shrager // Journal of Non-Newtonian Fluid Mechanics. — 2018. — Vol. 254. — P. 12–22.

6 Шульман З.П. Конвективный тепломассоперенос реологически сложных жидкостей / З.П. Шульман. — М.: Энергия, 1975. — 352 с.

7 Sattinova Z. Investigation of thermal conditions of the molding process of slurry beryllium oxide / Z. Sattinova, G. Ramazanova, B. Assilbekov, E. Mussenova // Eurasian Physical Technical Journal. — 2018. — № 15(30). — С. 110–116.

8 Себиси Т. Конвективный теплообмен. Физические основы и вычислительные методы / Т. Себиси, П. Брэдшоу; пер. с англ. — М., 1987. — 592 с.

9 Андерсон Д. Вычислительная гидромеханика и теплообмен: [В 2-х т.] / Д. Андерсон, Дж. Таннехилл, Р. Плетчер; пер. с англ. — М.: Мир, 1990. — Т. 1. — 384 с.

10 Sattinova Z. Numerical research of the beryllia ceramics formation process / Z. Sattinova, U. Zhapbasbayev, G. Ramazanova //Advanced Materials Research. — 2014. — Vol. 936. — P. 187–194. [Electronic resource]. — Access mode: https://doi.org/10.4028/www.scientific.net/AMR.936.187

11 Кусаиынов К. Моделирование процесса распыления водоугольного топлива, полученного из шламов шубаркульского угля / К. Кусаиынов, Н.К. Танашева, А.Ж. Тлеубергенова, А.В. Рожкова, С.Е. Сулейменова // Вестн. Караганд. ун-та. Сер. Физика. — 2015. — № 1(77). — С. 71–74.

12 Есьман Б.И. Термогидравлические процессы при бурении скважин / Б.И. Есьман, Г.Г. Габузов. — М.: Недра, 1991. — 216 с.

З.К. Саттинова, Т.Н. Бекенов, Б.К. Ассилбеков, Г.И. Рамазанова, К.М. Дюсенов

Әртүрлі реологиялық модельдерді қолдана отырып, BeO термопласт шликерін құюдың оптималды шарттарын есептеу алгоритмін жасау

Мақалада бериллий тотығы термопласт шликерінің құю қондырғысының дөңгелек каналындағы ағысы мен жылуалмасуының математикалық моделі есебінің қорытындысы келтірілген. Ағысты сипаттайтын Гершель–Балкли реологиялық модель негізіндегі теңдеулер жүйесінің сандық шешу алгоритмі құрастырылған. Қозғалыс, үзіліссіздік және энергия теңдеулер жүйесінің соңғы-айырымды аналогы Кранк–Никольсон схемасы арқылы алынған. Үшпараметрлі теңдеуді қолданудағы мақсат изотермиялық емес, ағысты қаншалықты эксперименттік деректерге сәйкес адекватты сипаттай алатындығын тексеру және Шведов–Бингам моделімен алынған есептеу нәтижелерімен салыстыру. Гершель-Балкли моделін қолданудың ерекшелігі жылжу жылдамдығының кең интервалында қисық сызықты шликер ағысын ескерудің күрделілігі болып саналады. Шликердің тиксотроп-дилатантты қасиетіне сәйкес ультрадыбысты өңдеуден кейінгі шликердің құрылымы бұзылып, қисық сызықты аққыштығы жылжу жылдамдығының үлкен интервалын қамтиды. Есептеулер нәтижесі ұсынылған модель шликердің тиксотропты ағысының ең басты ерекшеліктерін көрсететіндігі және эксперимент деректерімен сәйкестігі шликер ағысы жылдамдығы мен тығыздығының өзгеруі арқылы салыстырылды. Шликердің тұтқыр-пластикалы ағысының жылдамдығын, шликердің коагуляциялық құрылым түзу ерекшелігі мен ағыстың шекаралық шарттарын ескеріп, Шведов Бингам және Гершель–Балкли реологиялық модельдері негізінде сандық есептеулермен жүргізілді. Есептеулер нәтижесінде ағыс және жылуалмасу заңдылықтарын сипаттайтын жылдамдық, температура өрістерінің таралуы және тығыздықтың өзгеруі алынды. Бірінші текті шекаралық шартта Нуссельт критерийінің өзгеруі аналитикалық шешімімен сәйкес келетін жылуалмасу критерийінің канал бойымен өзгеруі көрсетілген. Құю процесі соңында біртекті құрылымды керамика өнімін алу үшін шликерді формалау процесінің тиімді шарттары анықталған.

Кілт сөздер: термопласт шликері, бериллий тотығы, керамика, реологиялық модель, Шведов-Бингам, Гершель–Балкли, тиксотропия, тұтқыр-пластикалы, изотермиялы емес.

З.К. Саттинова, Т.Н. Бекенов, Б.К. Ассилбеков, Г.И. Рамазанова, К.М. Дюсенов

Разработка алгоритма расчета оптимальных режимов литья термопластичного шликера BeO с использованием различных реологических моделей

В статье представлены результаты расчета математической модели течения и теплообмена термопластичного оксида бериллия в круглом канале литейной установки. Разработан алгоритм численного расчета системы уравнений на основе реологической модели Гершель-Балкли. Конечно-разностный аналог системы уравнений движения, непрерывности и энергии решается численным методом с использованием разностной схемы Кранка-Никольсона. Приведенные экспериментальные данные позволяют оценить деформационное поведение формовочной массы, а также установить зависимость реологических и теплофизических свойств термопластичного шликера от температуры. Учитывая особенности коагуляционного структурообразования и механизма течения с граничными условиями, в статье проводились расчеты скоростей вязкопластичного течения шликера на основе двух реологических моделей Шведова-Бингама и Балкли-Гершель. Трехпараметрическое уравнение применено с целью проверки согласованности адекватности экспериментальным данным неизотермического течения шликера по сравнению с моделью Шведова-Бингама. Данная модель для описания реологического поведения шликера связана со сложностью учета нелинейности кривой течения в широких пределах изменения скорости сдвига. Тиксотропно-дилатантное свойство шликера такому ограничению не удовлетворяет, и нелинейность кривой течения после разрушения структуры проявляется в широких пределах изменения скорости сдвига. В нашем случае применение модели Балкли-Гершеля позволило адекватно отразить реологическое поведение шликера, включая нелинейность кривой течения и вязкие эффекты среды. В результате расчетов были получены поля скорости, температуры и плотности, описывающие закономерности течения и теплообмена термопластичного шликера. Показано изменение критерия Нуссельта по длине формообразующей полости, совпадающей с аналитическим решением Нуссельта при граничных условиях первого рода. Найдены оптимальные условия процесса формования керамики способом горячего литья, которые позволяют получить на выходе отвердевшее изделие с однородной структурой.

Ключевые слова: термопластичный шликер, оксид бериллия, керамика, реологическая модель, Шведов-Бингам, Гершель-Балкли, тиксотропия, вязко-пластичный, неизотермический.

References

1 Shakhov, S.A. & Bitsoev, G.D. (1999). *Primenenie ultrazvuka pri proizvodstve vysokoteploprovodnykh keramicheskikh izdelii [Application of Ultrasound in the Manufacture of High Thermal Conductivity ceramic products]*. Ust-Kamenogorsk [in Russian].

2 Rudert, A. & Schwarze, R. (2009). Experimental and numerical investigation of a viscoplastic Carbopol gel injected into a prototype 3D mold cavity. *Non-Newtonian Fluid Mech, 161, (1-3),* 60–68.

3 Zhapbasbayev, U., Ramazanova, G., Sattinova, Z., Kenzhaliev, B., & Shakhov, S. (2016). Experimental and calculated data of the beryllium oxide slurry solidification. Applied Thermal Engineering, 96, 593–599. Retrieved from https://www.sciencedirect.com/journal/applied-thermal-engineering/vol/96

4 Froishteter, G.B., Smorodinskii, E.L., & Radionova, N.V. *Techenie i teploobmen neniutonovskikh zhidkostei v trubakh [Flow and heat transfer of non-Newtonian fluids in pipes]*. Kiev: Naukova dumka [in Russian].

5 Borzenko, E.I., Ryltseva, K.E., & Shrager, G.R. (2018). Free-surface flow of a viscous-plastic fluid during the filling of a planar channel. *Journal of Non-Newtonian Fluid Mechanics, 254,* 12–22.

6 Shulman, Z.P. (1975). *Konvektivnyi teplomassoperenos reologicheski slozhnykh zhidkostei [Convective heat and mass transfer of rheologically complex fluids]*. Moscow: Yenergiia [in Russian].

7 Sattinova, Z., Ramazanova, G., Assilbekov, B., & Mussenova, E. (2018). Investigation of thermal conditions of the molding process of slurry beryllium oxide. *Eurasian Physical Technical Journal, 15 (30),* 110–116.

8 Sebisi, T. & Bredshou, P. (1987). *Konvektivnyi teploobmen. Fizicheskie osnovy i vychislitelnye metody [Convective heat transfer. Physical foundations and computational methods]*. Moscow [in Russian].

9 Anderson, D., Tannekhill, Dzh., & Pletcher, R. (1990). *Vychislitelnaia gidromekhanika i teploobmen [Computational Fluid Mechanics and Heat Transfer]*. Moscow: Mir, 1, 384 [in Russian].

10 Sattinova, Z., Zhapbasbayev, U., & Ramazanova, G. (2014). Numerical research of the beryllium ceramics formation process. Advanced Materials Research, 936, 187–194. Retrieved from https://doi.org/10.4028/www.scientific.net/AMR.936.187

11 Kussaiynov, K., Tanasheva, N.K., Tleubergenova, A.Zh., Rozhkova, A.V., & Suleiymenova, S.E. (2015). Modelirovanie protsessa raspyleniia vodougolnogo topliva, poluchennogo iz shlamov shubarkulskogo uglia [Simulation of the process of spraying fuel obtained from coal-water slurry shubarkul coal]. *Vestnik Karagandinskogo universiteta. Seriia Fizika – Bulletin of the university of Karaganda – Physics,* 1(77), 71–74 [in Russian].

12 Esman, B.I. & Gabuzov, G.G. (1991). *Termogidravlicheskie protsessy pri burenii skvazhin [Thermohydraulic processes during well drilling]*. Moscow: Nedra [in Russian].

АВТОРЛАР ТУРАЛЫ МӘЛІМЕТТЕР
СВЕДЕНИЯ ОБ АВТОРАХ
INFORMATION ABOUT AUTHORS

Abuova, A.U. — PhD Doctor, Associate Professor of the Department of Technical Physics, Faculty of Physics and Technology, L.N. Gumilyov Eurasian National University, Nur-Sultan, Kazakhstan; e-mail: aisulu-us1980@yandex.kz

Abuova, F.U. (contact person) — PhD Doctor, Associate Professor of the International Department of Nuclear Physics, New Materials and Technologies, Faculty of Physics and Technology, L.N. Gumilyov Eurasian National University, Nur-Sultan, Kazakhstan; e-mail: Fatika_82@mail.ru

Aldiyarov, A.U. — Candidate of physical and mathematical sciences, Associate Professor, Al-Farabi Kazakh National University, Almaty, Kazakhstan.

Argynova A.Kh. — Senior Researcher, Satpayev University, Institute of Physics and Technology, Almaty, Kazakhstan; e-mail: argali7@mail.ru

Assilbekov, B.K. — PhD, Head of Research Laboratory «Computational modeling and information technology», Satbayev University, Almaty, Kazakhstan.

Baizhan, D.R. — Master's student, Engineer of the Research Center «Surface Engineering and Tribology», S. Amanzholov East Kazakhstan University, Ust-Kamenogorsk, Kazakhstan, e-mail: daryn.baizhan@mail.ru

Barilko, S.V. — Doctor of science (Engineering), Associate Professor of the Department of Information and Measuring Technologies, National Technical University of Ukraine «Igor Sikorsky Kyiv Polytechnic Institute», Ukraine, E-mail: poo4ta@bigmir.net

Beisenov, K.I. (contact person) — 1st year PhD student, Department of thermal physics and technical physics, Al-Farabi Kazakh National University, Almaty, Kazakhstan. E-mail: khasen.007@gmail.com

Bekenov, T.N. — Doctor of technical sciences, Professor of the Department «Organization of transport, traffic and transport operation», L.N. Gumilyov Eurasian National University, Nur-Sultan, Kazakhstan.

Dyusenov, K.M. — Candidate of technical sciences, Associate Professor of Department «Heat and power Engineering», L.N. Gumilyov Eurasian National University, Nur-Sultan, Kazakhstan.

Yerbolatova, G.U. — PhD, Senior Lecturer; D. Serikbayev East Kazakhstan Technical University, Ust-Kamenogorsk, Kazakhstan. E-mail: e.gulnara_77@mail.ru

Gavrilin, A.N. — Associate Professor, Candidate of Sciences (Engineering), Division for Mechanical Engineering, National Research Tomsk Polytechnic University, Russia. E-mail: tom-gawral@list.ru

Goncharenko, V.I. — Doctor of Technical Sciences, Professor, Director of the Military Institute of the Moscow Aviation Institute, Federal State Budgetary Educational Institution of Higher Education «Moscow Aviation Institute (National Research University), Moscow, Russia. E-mail: ovs_mai@mail.ru

Idrisova, T.K. — Junior Researcher, Satpayev University, Institute of Physics and Technology, Almaty, Kazakhstan. E-mail: zh.tynik@mail.ru

Inerbaev, T.M. — Candidate of physical and mathematical sciences, Leading Researcher of South China Normal University, Guangzhou, China. E-mail: talgat.inerbaev@gmail.com

Kaptagay, G.A. — PhD Doctor, Senior Lecturer, Kazakh National Women's Teacher Training University, Almaty, Kazakhstan. E-mail: gulbanu.kaptagai@mail.ru

Kowalewski, P. — PhD, Professor of the Faculty of Mechanical Engineering, Wroclaw University of Science and Technology, Wroclaw, Poland, e-mail: piotrus.kowalewski@gmail.com

Kozhanova, R.S. — PhD student, Shakarim University, Semey, Kazakhstan, e-mail: kozhanovars@yandex.kz (contact person).

Kucheruk, V.Yu. — Professor, Doctor of science (Engineering), Head of the Department of Metrology and Industrial Automation, Vinnytsia National Technical University, Ukraine, E-mail: vladimir.kucheruk@gmail.com

Kuvshinov, K.A. — Senior Lecturer, Candidate of Sciences (Engineering), Division for Mechanical Engineering, National Research Tomsk Polytechnic University, Russia, E -mail: kuvshinov@tpu.ru

Lisovets, S.N. — Associate Professor, Candidate of technical sciences (Engineering), Associate Professor of the Department of automated process control, V.I.Vernadsky Taurida National University, Ukraine, E-mail: ser.lis.290171@gmail.com

Mahajan, O.H. — Associate Professor at M.J. College, affiliated to K.B.C. North Maharashtra University, Jalgaon, India.

Makhanov, K.M. — Candidate of Physical and Mathematical Sciences, Associate Professor of the Department of Radiophysics and Electronics, Karaganda University of the name of academician E.A. Buketova, Karaganda, Kazakhstan. E-mail: makanov@inbox.ru

Moyzes, B.B. — Associate Professor, Candidate of Sciences (Engineering), Division for Testing and Diagnostics, National Research Tomsk Polytechnic University, Russia, E-mail: mbb@tpu.ru

Mukashev, K.M. — Doctor of Physical and Mathematical Sciences, Professor, Al-Farabi Kazakh National University, Almaty, Kazakhstan; E-mail: mukashev.kms@gmail.com

Mukhamedov, N.E. — PhD, Head of the reactor fuel testing laboratory, Institute of Atomic Energy branch RCE NNC RK, Kurchatov, Kazakhstan, E-mail: mukhamedov@nnc.kz

Nizhegorodov, A.I. — Professor, Doctor of science (Engineering), Department of Construction and Road-Making Machines and Hydraulic Systems, Irkutsk National Research Technical University, Russian Federation, E-mail: nastromo_irkutsk@mail.ru

Oleshko, V.S. — Candidate of Technical Sciences, Professor of the Department, Federal State Budgetary Educational Institution of Higher Education «Moscow Aviation Institute (National Research University)», Moscow, Russia. E-mail: oleshkovs@mai.ru

Rakhadilov, B.K. — PhD, Associate Professor, Senior Researcher Research Center «Surface Engineering and Tribology», S. Amanzholov East Kazakhstan University, Ust-Kamenogorsk, Kazakhstan, rakhadilovb@mail.ru

Ramazanova, G.I. — Candidate of Physics and Math sciences, Deputy Head of Petroleum Industrial Laboratory «Energy Modeling» Satbayev University, Almaty, Kazakhstan.

Sagdoldina, Zh.B. — PhD, Associate Professor, Leading Researcher of the research Center «Surface Engineering and Tribology», S. Amanzholov East Kazakhstan University, Ust-Kamenogorsk, Kazakhstan, e-mail: sagdoldina@mail.ru

Sarode, A.P. — Associate Professor and Head of Physics Department at Dr. A.G.D. Bendale Girls College, affiliated to K.B.C. North Maharashtra University, Jalgaon, India, e-mail: abhijitsarode@yahoo.com

Sattinova, Z.K. (contact person) — Candidate of physics and math sciences, Professor of the Department «Heat and power Engineering», L.N. Gumilyov Eurasian National University, Nur-Sultan, Kazakhstan; e-mail: Sattinova_zamira@mail.ru

Stepanov, A.V. — Senior Researcher, Tien Shan High-Altitude Scientific Station, P.N. Lebedev Physical Institute of the Russian Academy of Science; e-mail: tien-shan@mail.ru

Suiinzhanova, U.P. — 1st year PhD student, Department of thermal physics and technical physics, Al-Farabi Kazakh National University, Almaty, Kazakhstan. e-mail: only_kh@mail.ru

Suleimenov, N.A. — Doctoral student of D. Serikbayev East Kazakhstan Technical University, Ust-Kamenogorsk, Kazakhstan. E-mail: sna@mail.ru

Yerezhep, D.E. — PhD, Senior Lecturer, Al-Farabi Kazakh National University, Almaty, Kazakhstan.

Yurov, V.M. — Candidate of Physical-mathematical sciences, Professor, Director of the Scientific Research Center, Karaganda University of the name of academician E.A. Buketova, Karaganda, Kazakhstan. E-mail: exciton@list.ru

Zdorenko, V.G. — Professor, Doctor of science (Engineering), Professor of the Department of Information and Measuring Technologies, National Technical University of Ukraine «Igor Sikorsky Kyiv Polytechnic Institute», Ukraine, E-mail: valzd@meta.ua

Zhanbolatov, O.M. — Engineer of the laboratory for research of thermophysical and neutron-physical characteristics of irradiating devices, Institute of Atomic Energy branch RCE NNC RK, Kurchatov, Kazakhstan, E-mail: zhanbolatov@nnc.kz

Zhukov, V.V. — Candidate of Physical and Mathematical Sciences, Tien Shan High-Altitude Scientific Station, P.N. Lebedev Physical Institute of the Russian Academy of Sciences; E-mail: vzhu@mail.ru

Zhurerova, L.G. — PhD, Senior Researcher of the Research Center «Surface Engineering and Tribology»; S. Amanzholov East Kazakhstan University, Ust-kamenogorsk, Kazakhstan, e-mail: leila_uka@mail.ru

2021 жылғы
«Қарағанды университетінің хабаршысында»
жарияланған мақалалардың көрсеткіші. «Физика» сериясы

Указатель статей, опубликованных в журнале
«Вестник Карагандинского университета. Серия Физика»
в 2021 году

Index of articles published in
«Bulletin of the Karaganda University. Physics Series»
in 2021

КОНДЕНСАЦИЯЛАНҒАН КҮЙДІҢ ФИЗИКАСЫ
ФИЗИКА КОНДЕНСИРОВАННОГО СОСТОЯНИЯ
PHYSICS OF THE CONDENSED MATTER

ЖЫЛУФИЗИКАСЫ ЖӘНЕ ТЕОРИЯЛЫҚ ЖЫЛУТЕХНИКАСЫ
ТЕПЛОФИЗИКА И ТЕОРЕТИЧЕСКАЯ ТЕПЛОТЕХНИКА
THERMOPHYSICS AND THEORETICAL THERMOENGINEERING

ФИЗИКАНЫ ОҚЫТУ ӘДІСТЕМЕСІ
МЕТОДИКА ФИЗИКИ
METHODOLOGY OF PHYSICS